



TECHNISCHE  
UNIVERSITÄT  
WIEN

## DISSERTATION

# Coherent Wave Transport: Time Delay and Beyond

Ausgeführt zum Zwecke der Erlangung des akademischen Grades eines  
Doktors der technischen Wissenschaften

unter der Leitung von  
Univ.-Prof. Dipl.-Ing. Dr. Stefan Rotter  
Institut für Theoretische Physik, E136

eingereicht an der  
Technischen Universität Wien  
Fakultät für Physik

von  
Dipl.-Ing. Philipp Ambichl  
Matr.-Nr. e0625914  
Landstraßer Gürtel 43/6  
1030 Wien

---

Prof. Stefan Rotter

---

Prof. Allard Pieter Mosk

---

Ort, Datum

---

Dipl.-Ing. Philipp Ambichl



*In Loving Memory of Ing. Franz Lehner*

## Abstract in German - Deutsche Kurzfassung

# Phasenkohärenter Wellentransport: Streuzeiten und Wellenmanipulation

In allen Gebieten der Physik, in denen die Ausbreitung von Wellen eine zentrale Rolle spielt, ist man bestrebt, das Amplituden- und Phasenprofil der betrachteten Wellen genau zu verstehen und nach Möglichkeit zu kontrollieren. Moderne Techniken und Konzepte erlauben eine derartige Kontrolle heute bereits für akustische Wellen, Mikrowellen, oder auf dem Gebiet der Optik. Speziell im phasenkohärenten Transport optischer Wellen durch ungeordnete Medien konnten in den letzten Jahren beeindruckende experimentelle Erfolge, wie eine drastische Erhöhung der transmittierten Intensität, Fokussieren, Bildübertragung, sowie bzgl. nicht-invasiver Bildgebung erzielt werden.

Der Schlüssel für diese experimentellen Anwendungen liegt in der Vermessung der sogenannten Streuamplituden. Das Ziel der vorliegenden Arbeit ist es, die in diesen Amplituden gespeicherte Information auf geschickte Art und Weise für spannende Physik und Anwendungen nutzbar zu machen. Für jedes der hier diskutierten theoretischen Konzepte demonstrieren wir auch mögliche Anwendungen im Rahmen numerischer oder experimenteller Studien.

Das wohl bekannteste und am weitesten verbreitete Beispiel eines auf den Streuamplituden basierenden mathematischen Instruments ist der Zeitverzögerungs-Operator. Er misst die Zeitdauer eines Wellenstreuvorganges und ist, benannt nach den Pionieren in diesem Gebiet, heute unter dem Namen Wigner-Smith Time Delay Operator bekannt. Die mittlere Streu-, bzw. Aufenthaltsdauer in einem betrachteten System stellt eine Invariante dar, welche weit über die Physik hinaus eine Rolle spielt, so zum Beispiel auch für die Futtersuche staatenbildender Insekten. Unter einer gezielten Verwendung des Zeitverzögerungs-Operators werden wir zeigen, dass dieses weitreichende Ergebnis auch für den phasenkohärenten Wellentransport Gültigkeit besitzt. Weiters zeigen wir auf, dass die invariante Streuzeit auch eine interessante Verbindung zu einem weiteren fundamentalen Gesetz besitzt, das im Kontext photovoltaischer Solarzellen eine zentrale Bedeutung einnimmt, nämlich die sogenannte Yablonoitch-Grenze.

Das direkte Umfeld der Wigner-Smith Matrix verlassend, präsentieren wir darauffolgend eine Verallgemeinerung dieses Time Delay Operators und stellen entsprechende Konstruktionsalgorithmen vor, welche die praktische Umsetzung v.a. hinsichtlich eines Experiments erheblich vereinfachen. Diese

neu gefundenen Konzepte wenden wir in der Folge auf ungeordnete Systeme an, die einfallende Wellen entlang von verästelten Streumustern aufspalten. Wie wir zeigen werden, können einzelne dieser Intensitäts-Äste durch eine gezielte Wellenmanipulation selektiv angesprochen werden, was wiederum eine Anwendung im Bereich des effizienten Energietransports, oder der abhörsicheren Kommunikation durch ungeordnete Medien finden könnte. Sozusagen als Ableger dieses Projekts, präsentieren wir darüber hinaus auch eine Methode um eine effektive Tarnung eines beliebigen Streusystems zu realisieren, welche die zuvor genannten Konstruktionsalgorithmen beinhaltet.

Wie wir experimentell im Rahmen einer Kooperation mit Kollegen an der Yale University zeigen konnten, können verwandte mathematische Verfahren auch dazu benutzt werden, die Effizienz der Datenübertragung in sogenannten optischen Multimoden-Glasfasern zu erhöhen. Hierbei finden unsere Erkenntnisse hinsichtlich des verallgemeinerten Zeitverzögerungsoperators eine weitere Verwendung in der Berechnung von räumlichen Einschussprofilen, die eine Entkoppelung der zeitlichen und räumlichen Gestalt transmittierter Datenpulse in einem deutlich breiteren spektralen Bereich erlauben, als es bisher möglich war.

Wie wir zeigen werden, lässt sich allerdings nicht nur der Ausdruck für einen physikalisch sinnvollen Time Delay Operator verallgemeinern, auch sein Funktionsprinzip selbst lässt die Formulierung einer gesamten, neuen Operator-Klasse zu. Einen ausgewählten Vertreter dieser Operatoren werden wir benutzen, um im Inneren eines ungeordneten Mediums eine gezielte Fokussierung auf ein bestimmtes, streuendes Element zu erzeugen. Wie wir in Zusammenarbeit mit Kollegen von der Université de Nice in einem Mikrowellen-Experiment beweisen konnten, erlaubt unser Verfahren allerdings auch das Aussparen der Umgebung rund um besagten Streuer, was - im Gegensatz zur Möglichkeit des Fokussierens - einen völlig neuen, innovativen Ansatz darstellt. Ebenso diskutieren wir auch den Zusammenhang dieses von uns gefundenen Operators mit einem kürzlich durchgeführten Experiment, welches ein erfolgreiches Fokussieren auf bewegliche Ziele hinter einem ungeordneten Medium demonstriert hat. Wie sich zeigen wird, können unsere Methoden sogar die Effizienz der experimentellen Prozedur, die diese beachtlichen Resultate hervorgebracht hat, erhöhen. Schließlich stellen wir noch einen weiteren Vertreter unserer allgemeinen Operator-Klasse vor, welcher dazu verwendet werden kann, sogenannte 'teilchenartige' Wellenfronten zu erzeugen. Diese sehr speziellen Wellenprofile breiten sich nicht über den gesamten Querschnitt eines System aus, sondern verbleiben als kollimierte Strahlen im Laufe ihrer gesamten Propagation.

# Contents

Abstract in German - Deutsche Kurzfassung . . . . .	iv
<b>1 Introduction</b>	<b>1</b>
<b>2 Notion of Time Delay and Analytical Results</b>	<b>5</b>
2.1 Scattering Theory . . . . .	7
2.2 The Wigner-Smith Time Delay Operator . . . . .	10
2.3 Average Delay Times and the DOS . . . . .	13
Connection of the DOS and the Resonance Poles . . . . .	13
Connection of the Scattering Phases and the Resonance Poles	16
Connection of the Average Time Delay and the DOS . . . . .	17
Average Reflection and Transmission Delay Times . . . . .	17
2.4 General Time Delay Matrix and Principal Modes . . . . .	19
Time-Dependent Wave Packet . . . . .	21
Construction Scheme for Non-Invertible Scattering Matrices	22
2.5 The Dwell Time . . . . .	24
2.6 General Class of Dependence Shift (DEFT) Operators . . . . .	26
<b>3 Numerical &amp; Experimental Results and Applications</b>	<b>29</b>
3.1 Coherent Control of Branched Flow . . . . .	31
3.2 Camouflage by Wavefront Shaping . . . . .	37
3.3 A Universal Time as an Invariance Property of Wave Scattering	41
The Invariant Average Delay Time and the Yablonovitch Limit	48
3.4 Orthogonal Super Principal Modes . . . . .	52
3.5 DEFT: Focus and Omission in Disordered Media . . . . .	61
Connection to Focussing on a Moving Target . . . . .	67
Occupying Regular Islands in Classical Phase Space . . . . .	71
<b>4 Summary and Outlook</b>	<b>77</b>
<b>A Notion of Time Delay and Analytical Results</b>	<b>81</b>
A.1 Average Delay Times and the DOS . . . . .	82

Connection of the Scattering Phases and the Resonance Poles	82
Connection of the Average Time and the DOS . . . . .	84
A.2 The Dwell Time . . . . .	85
Energy Density and Power Flux for the Helmholtz Equation	85
Connection of $Q_d$ and $Q$ . . . . .	88
<b>B Numerical &amp; Experimental Results and Applications</b>	<b>89</b>
B.1 A Universal Time as an Invariance Property of Wave Scattering	90
Statistical Signature for the Chaotic and the Localized Regime	90
The Invariant Average Delay Time and the Yablonovitch Limit	91
B.2 Orthogonal Super Principal Modes . . . . .	92
Eigenstates of the Recurrence Operator . . . . .	92
Weighting Function & Wavepacket Envelope . . . . .	92
The Gradient-Based Optimization Scheme . . . . .	93
Expectation Value and Variance of the $\rho(\omega, \omega_0)$ -Operators .	94
<b>Bibliography</b>	<b>97</b>
<b>Acknowledgements</b>	<b>107</b>
<b>List of Publications</b>	<b>110</b>
<b>Curriculum Vitae</b>	<b>111</b>

CHAPTER 1 

**Introduction**

During the last decade, wavefront shaping and its intimate connection to the measurement of the so-called *scattering matrix* has become an extraordinarily fruitful, broad, and intensively studied field in many areas of wave scattering. The involved concepts prove very versatile, and realizations range from the domain of microwaves [1] and the propagation of sound [2] or water waves [3, 4] to optomechanics [5]. Since the advent of spatial light modulators, the concepts of wavefront shaping have also reached optics [6], where impressive advances in transmission enhancement and focusing [7, 8], the measurement of the scattering amplitudes [9, 10], image transmission [11], or non-invasive imaging [12] were made. Not only focusing at a single wavelength, but using experimental feedback loops, the focusing of pulses in space and time is already state-of-the-art [13–15].

With the recent advances in wavefront shaping and the phase-coherent measurement of wave amplitudes, also the implementation of concepts derived from the scattering matrix is within experimental reach today. Not only the scattering matrix itself, but rather any operator composed of the scattering amplitudes and phases can be constructed, once the latter are known. In this regard, a very intriguing concept theoretically conceived almost 60 years ago is the so-called *Wigner-Smith time delay operator*, whose construction, in fact, requires no explicit information about the interior of a given scattering setup other than encoded in the complex scattering amplitudes. Originally invented in the context of particle-particle reactions [16–19], this time delay operator is now the most-widely known and accepted mathematical tool used to ascribe specific delay times to wave scattering processes [20, 21]. The operator, its eigenvalues [22–24], and its connection to the density of states [25, 26] were intensively studied. However, also its eigenstates generally feature remarkable scattering properties in terms of their spectral stability bandwidths if the initial frequency of an incident wave is altered a feature especially advantageous for data transmission [27, 28]. The latter property lead to the proposal of *principal modes* - a concept intimately related to the time delay eigenstates. Only very recently in 2015, also the first experimental realization of the principal modes succeeded in the context of multimode optical fibers [29]. Rather ironically, an explicit measurement of the time delay operator has become possible for many different types of waves (like in optics or with acoustic or microwaves) with the notable exception of matter waves, which this concept was originally devised for. Among the principal modes, one can identify a special class of so-called *particlelike states*, as we could show in an earlier work [30]. These wave states feature intensity patterns of highly collimated beams during their entire propagation, as opposed to a more generic, continuous spreading of the wavefront. As we could reason, the particlelike

states obtain their favorable properties for energy-efficient and/or secure communication directly from the time delay operator.

This thesis is dedicated both to a broadening of the understanding and of the applicability of the time delay operator, as well as to a further development of its construction principles. As we will show, the concept of time delay and similar ideas, together with the techniques of wavefront shaping, open up a wide range of novel experiment designs and possible applications. Since the scattering of electromagnetic waves is currently the most fertile ground on which phenomena of coherent wave transport are studied, we will discuss all concepts and results in the framework of the scalar Helmholtz equation describing the transverse component of the electric field. Most of the results in the context of time delay have been derived for the Schrödinger equation, for which reason, we will not only review the fundamental concept of time delay, but also derive the occurring quantities for the Helmholtz equation.

Having done so, we proceed to the presentation of a very generally applicable time delay operator, of which the Wigner-Smith matrix is only one specific implementation. In most practical applications, the construction of this operator requires less information than the time delay operator originally proposed by Smith. Along with a solid theoretical embedding, we will also explain a corresponding construction algorithm for the case of imperfect experimental conditions, thus further facilitating our operator's feasibility. Ultimately, we will utilize our knowledge for the purpose of even generalizing not only its construction scheme, but also the functional principle of the Wigner-Smith time delay operator, and introduce a whole novel class of *dependence shift* (DEFT) operators, as we termed these matrices.

Along those lines, we apply our findings to several different systems, also discussing possible applications. Either we present numerical studies backing up our analytical claims, or show experimental measurements which directly resulted from our theoretical concepts. Our time-delay-related ideas specifically lead to an algorithm enabling the selection of single branches in systems allowing for a phenomenon called “branched flow”. The name stems from the wave-propagation patterns evolving in setups featuring a weak and correlated disorder potential, which show the emergence of individual branches rather than a fan-like spreading [31]. Related to the construction algorithms derived in the context of our generalized expression for the time delay operator, we will further demonstrate the possibility of hiding a specific scattering region by mimicking a different one. Directly from the Wigner-Smith expression for the time delay operator and its deep connection between to the density of states, however, we will derive, that the “mean-chord-length” theorem [32] does not only apply to situations

ranging from the food harvesting patterns of social insects to the scattering of particles, but also to wave dynamics even in the regime of localized transport. Further, we will also discuss the implications and links of our results to the so-called “Yablonovitch limit” [33], a fundamental limit for the efficiency of solar cells.

Introducing a new optimization procedure that relies on the information of the scattering amplitudes in a whole frequency interval rather than only at a single wavelength, we will also push the limits of output-stability bandwidth formerly prescribed by the principal modes. A static output pattern resulting from a given input over a preferably large spectral region is particularly advantageous for data transmission, and as one can show, the principal modes feature a very broad bandwidth in comparison to a random input configuration by construction. Yet we could successfully demonstrate the generation of a new set of *orthogonal super principal modes* (OSPMs), that even outplay the time delay eigenstates in this respect. In cooperation with Hui Cao’s group at Yale University, we could successfully demonstrate the experimental feasibility of our findings in an optical multi-mode fiber setup.

A different collaboration with Ulrich Kuhl’s group from Nice University, who are experts in phase-coherent transport through microwave resonators, permitted the experimental implementation of one representative of our newly introduced DEFT-class of operators. We use this tool to illustrate the possibilities of not only focussing on a chosen scatterer inside a disordered medium, but quite on the contrary, also sparing the region around it from radiation. As we further evince, an interesting connection to a recent experiment [34] can be drawn, where our findings might drastically widen the scope of the setup used there. Finally, we will show, that the time delay operator is not the only DEFT-member inheriting information about the phase space of trajectories. The operator we introduce in this regard is capable of generating particlelike states conveniently exploiting the “mixed” phase space structure of a D-shaped fiber system.

CHAPTER 2

**Notion of Time Delay and  
Analytical Results**

However simple it may be to associate a run time to a classical (pointlike) particle traversing a certain region of space, it is definitely non-trivial to do the same for a wave injected into a scattering system. On the one hand, parts of a time-dependent pulse launched into a certain setup might leave the system again via different scattering channels at different times; furthermore, those channels might even be spatially separated from each other, in general. On the other hand, a realistic wave packet possesses a non-zero temporal width, so it may not even be clear in terms of a well-defined point in time when the pulse enters the region of interest in the first place. Despite these difficulties, a commonly-accepted and well-studied operator measuring a physically reasonable delay time for waves exists.

The now-called *Wigner-Smith time delay operator* was first derived by Smith already in 1960 [19] following preceding works of Eisenbud [16], Bohm [17] and Wigner [18]. Originally devised in the context of particle-particle scattering, the time delay operator  $Q$  turned out to be a universal key for the understanding of time delay, i.e. the duration of a wave scattering process, in the whole field of linear wave scattering. In fact, the  $Q$ -operator quite counterintuitively assigns reasonable delay times even to time-independent monochromatic waves. It takes the appealingly simple form,

$$Q = -iS^\dagger \frac{dS}{d\omega}, \quad (2.1)$$

that is based solely on the knowledge of the scattering matrix  $S = S(\omega)$ , with  $\omega$  being the frequency of the incident wave ( $\dagger$  means Hermitian conjugation). The scattering matrix in turn relates incoming to outgoing flux amplitudes, and is the most widely-used tool in order to describe wave scattering processes. In what follows, we will motivate the concrete mathematical shape of the time delay operator  $Q$  and discuss the properties of its eigenstates and the meaning of its eigenvalues, the so-called *proper delay times*. Before doing so, however, we will review the very basics of linear wave dynamics in the framework of scattering theory in the next section. Subsequently, we will demonstrate the connection between the average delay time and the density of states using the resonance poles of the respective system under study. Afterwards, we will define time delay operators that can be constructed relying on only a fraction of the information stored in the total  $S$ -matrix and/or in cases where the amplitudes stored in  $S$  do not describe all channels the initial flux can scatter into. We will also present and briefly discuss another formalism describing a scattered wave's delay time, the dwell time, that is generally different from the quantity measured by the Wigner-Smith time delay operator. In the last section of this chap-

ter, we will ultimately introduce a whole class of novel operators, of which the time delay operator is just one of many possible realizations.

## 2.1 Scattering Theory

The geometric composition of a wave scattering problem can usually be subdivided into two domains: an asymptotic region and the scattering region (see Fig. 2.1(a)). The flux carried by the incident wavefront coming from the asymptotic region is injected into the system via discrete input channels, and scattered within the scattering region, where the flux is redistributed to the output channels by the actual scattering process. Ultimately the wave leaves again for the asymptotic region (see also [35, 36]). The scattering region is considered the only redistributive element, no mixing of the wave's intensity in the individual input and output channels occurs in the asymptotic region. The exact way in which the flux propagates from the input channels into the output channels can conveniently be described mathematically by the so-called scattering matrix  $S$ . Systems where an actual measurement of (parts of) the scattering matrix is already feasible with currently existing technology, are fibers [37] or disordered media [9] illuminated by optical waves, microwave resonators [1], ultrasonic waves in water [38], or slabs allowing for the propagation of elastic waves [5], just to mention a few examples. In case of optical systems, the in- and output channels can, e.g., be chosen as specific angles from which the sample is irradiated (as we did in order to obtain the experimental results in section 3.4); for microwave resonators (as discussed in section 3.5) and elastic slabs, often a basis of waveguide modes is suitable.

The general concepts of wavefront shaping presented throughout this thesis are valid for many types of waves and applicable to many kinds of scattering setups, however, we will discuss all of them in the framework of the scalar Helmholtz equation,

$$(\Delta + n(\vec{x})^2 k^2) \psi(\vec{x}) = 0, \quad (2.2)$$

where  $\Delta = \sum_j \partial^2 / \partial x_j^2$  denotes the Laplacian,  $n(\vec{x})$  the generally non-uniform refractive index, and  $k = \omega/c$  is the vacuum wavenumber of the wavefunction  $\psi(\vec{x})$ . For the numerical studies presented in the next chapter, we solved the Helmholtz Eq. on a finite-difference grid, using the advanced modular recursive Green's function method [39, 40].

On an abstract operator level, the  $S$ -matrix corresponding to Eq. (2.2) takes the form (see, e.g., [41], subsection 6.1.3),

$$S = -\mathbf{1} + 2i V^\dagger G V, \quad (2.3)$$

which conveniently illuminates the mathematical structure of wave scattering as explained at the beginning of this section:  $G$  is the Green's function of the Helmholtz equation,  $G = (\Delta + n^2 k^2)^{-1}$ , which is closely related to the corresponding propagator (see also [42]).  $V$  is a so-called coupling matrix, connecting scattering channels and scattering region. For reasons of simplicity, we implicitly assumed the output channels to be the time-reversed partners of the input channels. As can easily be seen from Eq. (2.3) now, the action of  $S$  is coupling an incident wave into the system, propagating it within, and out-couple it again into the scattering channels. The unity matrix  $\mathbb{1}$  in Eq. (2.3) is necessary to account for the correct phase of the back-scattered wave.

For 2-port systems, as discussed in the next chapter, it is often advantageous to further group the scattering amplitudes stored in  $S$  according to

$$S = \begin{pmatrix} r & t' \\ t & r' \end{pmatrix}. \quad (2.4)$$

The amplitudes corresponding to a reflection from port 1 back into port 1 are stored in the reflection matrix  $r$ , the respective amplitudes for a transmission from port 1 into port 2 are grouped in the transmission matrix  $t$ .  $t'$  and  $r'$  are the analogous matrices for injection through port 2.

A specific example of such a system is depicted in Fig. 2.1(b), where a (two-dimensional) resonator is coupled to two distinct rectangular waveguides. In this case a suitable basis of scattering channels are the waveguide modes. If we assume clean and rectangular waveguides featuring a refractive index of  $n(\vec{x}) \equiv 1$ , as well as perfectly reflecting boundaries, the modes have the simple, analytical form,

$$\phi_m(x, y) = \frac{1}{\sqrt{k_{x,m}}} \sqrt{\frac{2}{w}} \chi(y) e^{ik_{x,m} x}, \quad (2.5)$$

with  $\chi(y) = \sin(k_{y,m} y)$  here. The transverse width of the waveguide is referred to as  $w$ , the prefactors  $1/\sqrt{k_{x,m}}$  and  $\sqrt{2/w}$  assure a flux normalization and a transverse normalization, respectively, which are often beneficial. The wavenumbers  $k_{x,m}$  and  $k_{y,m} = m\pi/w$  with  $m = 1, 2, 3, \dots$  are connected by the total wavenumber  $k$  in Eq. (2.2) like

$$k^2 = k_{x,m}^2 + k_{y,m}^2. \quad (2.6)$$

From Eq. (2.6) we see, that  $k_{x,m}$  is only a real number and, therefore, corresponds to a propagating mode, if  $m < kw/\pi$ . In case of  $m > kw/\pi$ , the longitudinal wavenumber  $k_{x,m}$  is purely imaginary, so the corresponding mode is evanescently damped in propagation direction and carries no flux.

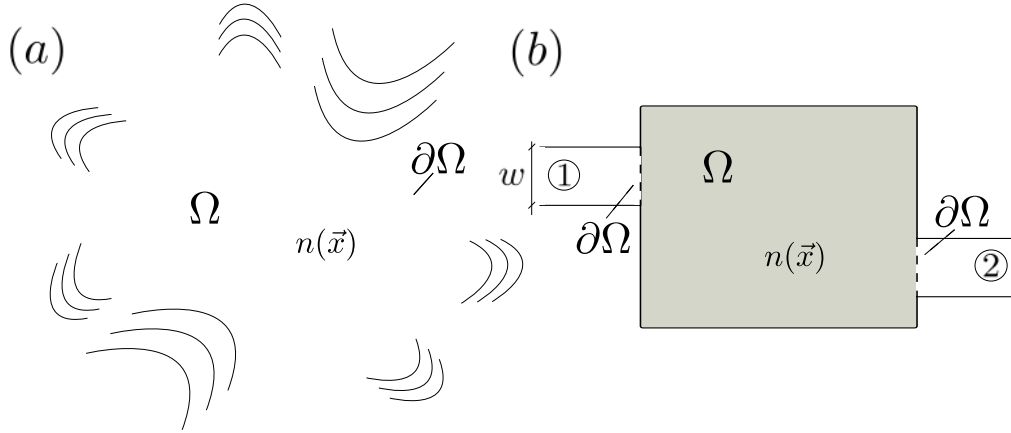


**Figure 2.1:** (a) An impinging wavefront incident from the asymptotic region (white) is scattered within the scattering region  $\Omega$  (grey) by a generally non-uniform refractive index distribution  $n(\vec{x})$  (in case of optical waves) and ultimately leaves again for the asymptotic region. The scattering matrix  $S$  is evaluated along the boundary of the scattering region,  $\partial\Omega$  (dashed line). (b) A resonator (grey), that constitutes the scattering region  $\Omega$ , is attached to two waveguides (white), port 1 (left) and port 2 (right), that represent the asymptotic area. The scattering matrix for this system can be written in the block structure shown in Eq. (2.4).

The  $S$ -matrix usually contains the scattering amplitudes for flux-carrying (open) channels, only. If for the corresponding incoming and outgoing flux coefficients with respect to the chosen basis of scattering channels,  $\vec{u}$  and  $\vec{v} = S\vec{u}$ , respectively,  $|\vec{v}|^2 = |\vec{u}|^2$  is valid, it follows that the scattering matrix must be unitary,

$$S^\dagger S = \mathbb{1}. \quad (2.7)$$

In the following section, we will show that the unitarity stated by Eq. (2.7) can be used in order to show that the time delay operator  $Q$  in flux-conserving systems is Hermitian.

## 2.2 The Wigner-Smith Time Delay Operator

Before we derive an expression for the quantity measured by the Wigner-Smith time delay operator  $Q$ , we qualitatively recall the seminal ideas that ultimately led to its derivation. For the latter purpose, we consider the (relatively simple) case of a wave packet transmitting through an arbitrary one-dimensional scattering region characterized by its scalar frequency-dependent transmission 'matrix'  $t(\omega)$  (see also [18] as well as [20] and references therein). Note that the transmission amplitude  $t(\omega)$  in this section must not be confused with the time  $t$ . For the transmitted part of a scattered wave packet one finds,

$$\psi(x, t) = \frac{1}{\sqrt{2\pi}} \int d\omega |t(\omega)| |\epsilon(\omega)| e^{i(kx - \omega t + \varphi_\epsilon(\omega) + \varphi(\omega))}, \quad (2.8)$$

where we assumed a free-space propagation outside the scattering region, and splitted the complex transmission amplitude into its absolute value and phase according to  $t(\omega) = |t(\omega)| \exp(i\varphi(\omega))$ . The complex-valued function  $\epsilon(\omega) = |\epsilon(\omega)| \exp(i\varphi_\epsilon(\omega))$  denotes the assumed spectral input envelope of the pulse. At large times  $t$ , or equivalently, far away from the scattering region, i.e., at large values of  $x$ , we see from Eq. (2.8), that most integrands at different frequencies  $\omega$  cancel each other due to the rapid fluctuation of the phase factor. Only in the vicinity of a stationary point in the latter exponent, the terms interfere constructively. Applying the so-called stationary phase approximation (see for example [43] for a discussion of its applicability, limitations, and corrections in the context of delay times in wave transmission) to Eq. (2.8) gives

$$\frac{d}{d\omega} (kx - \omega t + \varphi_\epsilon(\omega) + \varphi(\omega)) = 0. \quad (2.9)$$

Following any significant instance of the wavepacket  $\psi(x, t)$ , e.g., its peak or 'center of mass', we can solve Eq. (2.9) for this distinguished, time-dependent spatial position  $x_p(t)$ , resulting in

$$x_p(t) = \frac{d\omega}{dk} \left( t - \frac{d\varphi_\epsilon(\omega)}{d\omega} - \frac{d\varphi(\omega)}{d\omega} \right) = \frac{d\omega}{dk} (t - \tau_\epsilon - \tau). \quad (2.10)$$

Recognizing the first term on the right-hand side of Eq. (2.10) as the group velocity  $v_g = d\omega/dk$ , we see that the scattered wave packet suffers a total temporal delay of  $\tau_\epsilon + \tau$ . Since  $\tau_\epsilon$  is just the expected delay simply resulting

from the spectral shape of the envelope  $\epsilon(\omega)$ , we can identify

$$\tau = \frac{d\varphi(\omega)}{d\omega} \quad (2.11)$$

as the additional time delay the pulse experiences when compared to a wave packet which would not have been affected by the scattering process at all, i.e.,  $t(\omega) \equiv 1$ . The so-called *phase time* described by Eq. (2.11) can be generalized to multichannel scattering and higher-dimensional systems, as we will show in the following.

As briefly mentioned at the end of the previous section, an incoming wave can be characterized by its (flux-)coefficients  $\vec{u}$  with respect to the chosen basis of scattering channels. Applying the scattering matrix  $S$  then yields the corresponding output coefficients  $\vec{v} = S\vec{u}$ . The proper generalization of Eq. (2.11) then reads like [44],

$$\tau = \sum_n |[\vec{v}]_n|^2 \frac{d\varphi_n}{d\omega} = \sum_n |[S\vec{u}]_n|^2 \frac{d \arg([S\vec{u}]_n)}{d\omega}, \quad (2.12)$$

where  $[\vec{v}]_n$  means the  $n$ -th complex element of the vector  $\vec{v}$ , and  $\varphi_n$  denotes the phase of the former. As indicated in the previous section, a scattering system featuring neither any losses due to power outcoupling, absorption, etc., nor any amplifications by possible gain mechanisms, is perfectly flux-conserving, resulting in a unitary scattering matrix,  $S^\dagger = S^{-1}$ . Using again  $\vec{v} = S\vec{u}$ , we thus have,  $\sum_n |[\vec{v}]_n|^2 = \vec{v}^\dagger \vec{v} = \vec{u}^\dagger \vec{u} = 1$  if the input vector  $\vec{u}$  is normalized to one. Eq. (2.12) can, therefore, be considered a meaningful average over the phase times of the individual scattering channels weighted with their respective (normalized) intensities.

In what follows, we will show that the average phase delay time given by Eq. (2.12) equals exactly the expectation value of the Wigner-Smith time delay operator evaluated for the input state  $\vec{u}$  and a unitary  $S$ -matrix. We start from the expression for  $Q$  given by Eq. (2.1) at the beginning of this chapter,

$$\tau' = \vec{u}^\dagger Q \vec{u} = \vec{u}^\dagger \left( -iS^\dagger \frac{dS}{d\omega} \right) \vec{u}, \quad (2.13)$$

and consider the vector  $\vec{u}$  as frequency independent,  $d\vec{u}/d\omega = 0$ . It thus follows from Eq. (2.13) for the output vector  $\vec{v}$ ,

$$\tau' = -i\vec{v}^\dagger \frac{d\vec{v}}{d\omega} = -i \sum_n [\vec{v}]_n^* \frac{d[\vec{v}]_n}{d\omega}, \quad (2.14)$$

where the symbol  $*$  means complex conjugation. Again fractionizing the vector element  $[\vec{v}]_n$  in its amplitude and phase,  $[\vec{v}]_n = |[\vec{v}]_n| \exp(i\varphi_n)$ , and

inserting into Eq. (2.14), we find

$$\tau' = \sum_n |[\vec{v}]_n|^2 \frac{d\varphi_n}{d\omega} = \tau, \quad (2.15)$$

where we used  $\sum_n |[\vec{v}]_n| d|[\vec{v}]_n|/d\omega = 0$  due to  $d(\vec{v}^\dagger \vec{v})/d\omega = d(1)/d\omega = 0$  because of the assumed flux conservation. The delay time given by Eqs. (2.12) or equally (2.15) is a purely real quantity independent of the input coefficients in  $\vec{u}$ . Indeed, one can easily see that  $Q$  is a Hermitian matrix based on the unitarity of  $S$ , which thus features purely real eigen- and expectation values. We start by taking the derivative with respect to frequency of both sides of the equation

$$S^\dagger(\omega) S(\omega) = \mathbb{1} \rightarrow \frac{d}{d\omega} (S^\dagger(\omega) S(\omega)) = 0. \quad (2.16)$$

Evaluating and transforming the latter equation results in

$$-iS^\dagger \frac{dS}{d\omega} = i \frac{dS^\dagger}{d\omega} S \rightarrow Q = Q^\dagger, \quad (2.17)$$

which directly states the Hermiticity of the  $Q$ -operator (see also [19]). The fact that the time delay operator is self-adjoint for unitary  $S$ -matrices implies desirable features such as a complete and orthonormal eigenbasis in the vector space of input configurations on the one hand, and real eigenvalues that are conveniently interpreted as physically reasonable delay times, on the other hand.

In section 2.4, we will present a time delay matrix that is generally non-Hermitian, but still provides meaningful delay times in the real parts of its eigenvalues. Before doing so, we will discuss in the next section the connection of the average time delay and the density of states (DOS), as well as a concept to separate average reflection and transmission times drawn from  $Q$ .

## 2.3 Average Delay Times and the DOS

The connection of the density of states (DOS), i.e., the number of states or levels per unit frequency interval for the scattering region, with the Green's function, the scattering matrix and scattering phases, as well as the average delay time has been studied intensively during the last decades from the theoretical side as well as experimentally [25,26,45–50]. Despite, or perhaps due to such an extensive activity in this field, the literature lacks a clear and complete derivation of this enlightening connection especially in the context of the Helmholtz equation, which differs with respect to certain subtleties from the corresponding calculations for the Schrödinger equation. For those reasons, we will present a largely self-consistent derivation of this connection. Much of the derivations with respect to the specific connection of the Green's function and the average delay time in this section and the respective appendices works analogously to the calculations made in [36]. We will connect all quantities involved in each step to the complex poles of the Green's function, ultimately linking the DOS to the average delay time. At the end of this section, we will demonstrate a physically reasonable way to define a transmission and a reflection time separately, before we move on to a completely general definition for a time delay matrix in the next section.

### Connection of the DOS and the Resonance Poles

The DOS for a bounded and *closed* system is given by the expression

$$\rho(k^2) = \sum_n \delta(k^2 - \lambda_n), \quad (2.18)$$

where the real and discrete eigenvalues  $\lambda_n$  are defined by the Helmholtz equation,

$$(\Delta + n^2(\vec{x}) \lambda_n) \psi_n(\vec{x}) = 0, \quad (2.19)$$

subject to Hermitian boundary conditions. The symbol  $\delta$  on the right-hand side of Eq. (2.18) stands for the Dirac delta function. In case of a bounded but *open* system, however, like a finite scattering region connected to the asymptotic region, injected flux will gradually leak out of the scattering area. This uncertainty in the duration of time the flux is confined inside the system translates into a corresponding uncertainty in the frequency of such a 'quasi-bound' or 'meta-stable' state. As was postulated by Breit and Wigner in the context of neutron scattering already in 1936 [51], the DOS then turns from discrete, sharp  $\delta$ -peaks as in Eq. (2.18) to an approximate

form of

$$\rho(k^2) \approx -\frac{1}{\pi} \text{Im} \left[ \sum_n \frac{1}{k^2 - \lambda_n} \right] = \frac{1}{\pi} \sum_n \frac{\Gamma_n/2}{(k^2 - k_n^2)^2 + \Gamma_n^2/4}, \quad (2.20)$$

where  $\text{Im}$  stands for the imaginary part. The opening of the system results in a non-Hermitian equation governing the mode-structure inside the scattering region. This in turn causes the eigenvalues  $\lambda_n$  to become complex, which translates into temporally decaying internal modes, as expected for an open system. In Eq. (2.20), we split the complex eigenvalues in their real and imaginary parts like  $\lambda_n = k_n^2 - \Gamma_n/2$ , and we consequently see that the DOS is described as a sum of Lorentzians at positions  $k_n$  and widths of  $\Gamma_n$ . As already mentioned, this expression for the DOS is only an approximation and theorists have tried to generalize it and to test its applicability (see [52] and references therein) ever since its postulation. We would like to mention a very appealing ansatz of describing the actual DOS using Delta functions allowing for a complex argument [53–55], at this point. Unfortunately, we could not find a precise and clear statement in the literature about the extent of applicability of the Breit-Wigner approximation to the scattering systems we study in this thesis. The results we will present in section 3.3 of the next chapter, however, indirectly prove its applicability, and further justify the usage of Eq. (2.20). We can also qualitatively motivate this shape of the DOS though, as we will briefly discuss in what follows.

On the one hand, please note that the sum of Lorentzians in Eq. (2.20) turns over to the right expression for the DOS in Eq. (2.18) in the limit of vanishing linewidths  $\Gamma_n$ , which corresponds to a closed system, because of the identity

$$\delta(x - x') = \lim_{\epsilon \rightarrow 0} \frac{1}{\pi} \frac{\epsilon^2}{(x - x')^2 + \epsilon^2}. \quad (2.21)$$

On the other hand, in case of a closed (Hermitian) system, one finds the relation between the DOS and the Green's function to evaluate to (see, e.g., Eq. (1.20) and pp. 392-393 in [56]),

$$\rho(k^2) = -\frac{1}{\pi} \text{Im} \left[ \text{Tr} \left( \tilde{G}(k^2) \right) \right], \quad (2.22)$$

where  $\text{Tr}$  denotes the trace. If we just apply Eq. (2.22) derived for Hermitian systems to the non-Hermitian system of our open scattering region  $\Omega$ , we end up exactly with the Breit-Wigner formula for the DOS given in Eq. (2.20), as we will show in the remainder of this subsection.

The Green's function  $G$  appearing in Eq. (2.3) is defined by the equation,

$$(\Delta + n(\vec{x})^2 k^2) G(\vec{x}, \vec{x}'; k^2) = \delta(\vec{x} - \vec{x}'), \quad (2.23)$$

with  $\vec{x}, \vec{x}' \in \Omega$ , or in an abstract and simplified way,

$$G(k^2) = \frac{1}{(\Delta + n^2 k^2)}. \quad (2.24)$$

The proper function corresponding to the DOS is slightly different from the Green's function in Eq. (2.24) though [57, 58],

$$\tilde{G}(k^2) = \frac{1}{(n^{-2}\Delta + k^2)} = G(k^2) n^2. \quad (2.25)$$

Please note that purely outgoing, so-called 'constant-flux' boundary conditions [59] must be imposed on the Eqs. (2.23 - 2.25). The former can also be included into the Helmholtz equation in matrix form by adding the anti-Hermitian matrix  $iVV^\dagger$  to the operator on the left-hand side of Eq. (2.23), with  $V$  being equal to the coupling matrix in Eq. (2.3) [36, 41, 44]. For reasons of simplicity, we include the Hermitian part of the constant-flux boundary conditions only implicitly here. We can also express  $\tilde{G}(k^2)$  in its spectral representation,

$$\tilde{G}(\vec{x}, \vec{x}'; k^2) = \sum_n \frac{\psi_n^R(\vec{x}) \psi_n^L(\vec{x}')}{k^2 - \lambda_n}, \quad (2.26)$$

where the left/right eigenstates  $\psi_n^{L/R}(\vec{x})$  satisfy the generalized eigenvalue equations

$$\psi_n^L(\vec{x}) \left( \overleftarrow{\Delta} + n^2(\vec{x}) \lambda_n + iVV^\dagger \right) = 0, \quad (2.27)$$

and

$$\left( \overrightarrow{\Delta} + n^2(\vec{x}) \lambda_n + iVV^\dagger \right) \psi_n^R(\vec{x}) = 0, \quad (2.28)$$

respectively. The arrows  $\leftarrow/\rightarrow$  in the subscripts formally mean that the operator acts to the left/right, and further we assume a normalization of eigenstates like  $\int_\Omega dV \psi_n^L(\vec{x}) \psi_n^R(\vec{x}) = 1$ . As mentioned before, due to the anti-Hermitian coupling, the eigenvalues  $\lambda_n$  are generally complex numbers, which accounts for poles of the Green's function (2.26), and thus of the scattering matrix, in the complex plane at positions  $\lambda_n$ . The latter are thus the positions of the resonances of the scattering system. Please note that generally  $\lambda_n = \lambda_n(\omega)$  due to the coupling  $V = V(\omega)$ , but since this frequency-dependence can often be neglected, we just refer to the  $\lambda_n$  as the 'resonance poles', for reasons of simplicity. For the trace  $\text{Tr}(\tilde{G}(k^2)) = \int dx \tilde{G}(\vec{x}, \vec{x}; k^2)$ , we find from Eq. (2.26) and using the normalization of the eigenstates,

$$\text{Tr}(\tilde{G}(k^2)) = \sum_n \frac{1}{k^2 - \lambda_n}. \quad (2.29)$$

Inserting  $\lambda_n = k_n^2 - \Gamma_n/2$  for the eigenvalues, we immediately see the validity of Eq. (2.22) by comparison of Eq. (2.29) to Eq. (2.20). For the actual DOS in terms of the frequency we thus get,

$$\rho(\omega) = \rho(k^2) \frac{dk^2}{d\omega} = \frac{2\omega}{\pi} \sum_n \frac{\gamma_n/2}{(\omega^2 - \omega_n^2)^2 + \gamma_n^2/4} = -\frac{2\omega}{\pi c^2} \text{Im} \left[ \text{Tr} \left( \tilde{G}(\omega) \right) \right], \quad (2.30)$$

where we used  $k = \omega/c$  for the vacuum wavenumber and defined  $\omega_n := k_n c$  and  $\gamma_n := \Gamma_n c^2$ .

## Connection of the Scattering Phases and the Resonance Poles

In this subsection, we will present the connection of the DOS based on the expression (2.30) in the previous subsection and the scattering matrix. For that purpose, we note that the  $S$ -matrix given by Eq. (2.3) can also be written in terms of its Cayley transform (see Appendix A.1 and [60]),

$$S = -\mathbb{1} + 2iV^\dagger G V = -\frac{\mathbb{1} - iV^\dagger G_0 V}{\mathbb{1} + iV^\dagger G_0 V}, \quad (2.31)$$

with  $G_0$  being defined by the relation  $G = [G_0^{-1} + iVV^\dagger]^{-1}$ . As it will turn out, the proper connection between the scattering matrix and the DOS involves the determinant

$$\text{Det}[S] = \text{Det} \left[ -\frac{\mathbb{1} - iV^\dagger G_0 V}{\mathbb{1} + iV^\dagger G_0 V} \right] = \frac{\text{Det}[\mathbb{1} - iV^\dagger G_0 V]}{\text{Det}[\mathbb{1} + iV^\dagger G_0 V]}, \quad (2.32)$$

which evaluates to (see Appendix A.1 and [36])

$$\text{Det}[S] = e^{i\sum_n \theta_n} = \prod_n \frac{\omega^2 - \omega_n^2 - i\gamma_n/2}{\omega^2 - \omega_n^2 + i\gamma_n/2}. \quad (2.33)$$

We expressed the determinant of  $S$  as the product of its eigenvalues, where the  $\theta_n$  are the scattering (eigen-)phases. The complex numbers  $\lambda_n = (\omega_n^2 - i\gamma_n/2)/c^2$  are exactly the eigenvalues of the Helmholtz Equations defined in Eqs. (2.27) and (2.28). In a next step, we will demonstrate the connection of the resonance poles and the average time delay ultimately leading to the link between the DOS and the time delay.

## Connection of the Average Time Delay and the DOS

The average delay time of waves scattering through a given system can easily be quantified using the time delay operator by just taking the average of its eigenvalues,

$$\langle \tau \rangle = \frac{1}{N} \sum_n^N \tau_n = \frac{1}{N} \text{Tr}(Q), \quad (2.34)$$

which can be written as the trace of the  $Q$ -matrix divided by the number of flux-carrying input channels  $N$ . Inserting the expression of  $Q$  in terms of the scattering matrix,  $Q = -iS^\dagger dS/d\omega$ , we will express  $\langle \tau \rangle$  in terms of the resonance poles. For that purpose we state (see Appendix A.1 and [36])

$$\langle \tau \rangle = \frac{1}{N} \text{Tr}(Q) = -\frac{i}{N} \frac{d}{d\omega} \ln(\text{Det}[S]). \quad (2.35)$$

Using the expression we found for the determinant of the scattering matrix in terms of the resonance poles (Eq. (2.33)), we have

$$\ln(\text{Det}[S]) = \sum_n \ln \left( \frac{\omega^2 - \omega_n^2 - i\gamma_n/2}{\omega^2 - \omega_n^2 + i\gamma_n/2} \right), \quad (2.36)$$

and we are subsequently able to formulate the average delay time  $\langle \tau \rangle$  as (see Appendix A.1),

$$\langle \tau \rangle = \frac{4\omega}{N} \sum_n \frac{\gamma_n/2}{(\omega^2 - \omega_n^2) + \gamma_n^2/4}. \quad (2.37)$$

A comparison of Eqs. (2.37) and (2.30) finally yields the connection between the average delay time and the density of states [25, 26],

$$\langle \tau(\omega) \rangle = \frac{2\pi}{N} \rho(\omega). \quad (2.38)$$

## Average Reflection and Transmission Delay Times

In case one is interested in the average delay time  $\langle \tau \rangle$  for a 2-port system, or equally the DOS, it might also be of interest to separate the average delay into an average reflection and an average transmission time, as we will make use of in section 3.3. The derivations in this subsection were published in [61].

In order to do this separation of scattering times, we return to the expression for the expectation value of the  $Q$ -operator for an arbitrary input

$\vec{u}$  in Eq. (2.15) and deduce

$$\langle \tau \rangle = \frac{1}{N} \text{Tr}(Q) = \sum_{mn}^N |S_{mn}|^2 \frac{d\varphi_{mn}}{d\omega}, \quad (2.39)$$

with the complex element  $S_{mn} = |S_{mn}| \exp(i\varphi_{mn})$  of the scattering matrix. Using the division of  $S$  into reflected and transmitted parts (Eq. (2.4)), we can define the total transmission  $T_{\text{tot}}$  and reflection  $R_{\text{tot}}$  according to

$$\begin{aligned} T_{\text{tot}} &= \frac{1}{N} \left( \sum_{mn}^{N/2} |t_{mn}|^2 + |t'_{mn}|^2 \right) \\ &= 1 - \frac{1}{N} \left( \sum_{mn}^{N/2} |r_{mn}|^2 + |r'_{mn}|^2 \right) = 1 - R_{\text{tot}}. \end{aligned} \quad (2.40)$$

For reasons of simplicity, we assumed the reflection and transmission matrices to be square blocks of dimension  $N/2 \times N/2$ . An effective number of transmitting channels then evaluates to  $N_T = T_{\text{tot}}N$ , and analogously the effective number of reflected channels is  $N_R = R_{\text{tot}}N$ , with  $N = N_T + N_R$ . The second equal sign in Eq. (2.40) follows from the unitarity of  $S$ . Quite similar to (2.40), we can also define

$$\langle \tau_T \rangle = \frac{1}{N_T} \left( \sum_{m,n}^{N/2} |t_{mn}|^2 \frac{d\varphi_{mn}^t}{d\omega} + |t'_{mn}|^2 \frac{d\varphi_{mn}^{t'}}{d\omega} \right), \quad (2.41)$$

and

$$\langle \tau_R \rangle = \frac{1}{N_R} \left( \sum_{m,n}^{N/2} |r_{mn}|^2 \frac{d\varphi_{mn}^r}{d\omega} + |r'_{mn}|^2 \frac{d\varphi_{mn}^{r'}}{d\omega} \right), \quad (2.42)$$

where, e.g.,  $r_{mn} = |r_{mn}| \exp(i\varphi_{mn}^r)$  denotes a complex reflection amplitude from left to left. The connection between the average transmission and reflection delay times and the total mean delay is then very intuitive and reads like

$$\langle \tau \rangle = T_{\text{tot}} \langle \tau_T \rangle + R_{\text{tot}} \langle \tau_R \rangle. \quad (2.43)$$

## 2.4 General Time Delay Matrix and Principal Modes

Throughout the last section, we assumed a perfectly flux-conserving system, accounting for a unitary scattering matrix and thus a Hermitian time delay operator. In many cases, especially in experimental applications, however, only subparts of  $S$  might be measurable. Additionally, there are always sources of loss present in a realistic setup that often cannot be completely neglected. For those reasons, the detected scattering amplitudes will constitute a non-unitary matrix, which impedes simple expressions for the delay time of a wave such as Eq. (2.12), or a straightforward definition of partial delay times like we did in section 2.3. Therefore, a general definition for a time delay operator, including the Hermitian Wigner-Smith operator  $Q$  as a special case, would be very desirable. We will introduce such an operator and will provide physical arguments for its construction in the following. Without loss of generality, the presented derivations will be done in terms of a sub-unitary transmission matrix  $t$ , that we firstly assume to be invertible. Later in this section we will also present a construction algorithm in case of a non-invertible matrix.

Due to the previously-assumed unitarity of  $S$ , the defining equation of  $Q$  can also be written like

$$Q = -iS^\dagger \frac{dS}{d\omega} = -iS^{-1} \frac{dS}{d\omega}. \quad (2.44)$$

The right-hand side of Eq. (2.44) will serve us as a general construction scheme for a universally applicable, generically non-Hermitian time delay operator

$$q = -it^{-1} \frac{dt}{d\omega}. \quad (2.45)$$

In order to breathe physical life into this mathematical expression, consider an arbitrary (static) input configuration specified by its coefficient vector  $\vec{u}$ . The corresponding frequency-dependent output vector reads like

$$\vec{v}(\omega) = t(\omega) \vec{u}. \quad (2.46)$$

Accordingly, a Taylor series up to first order then reads

$$\vec{v}(\omega) \approx \vec{v}(\omega_0) + \left. \frac{d\vec{v}}{d\omega} \right|_{\omega_0} (\omega - \omega_0) = t(\omega_0) \vec{u} + \left. \frac{dt}{d\omega} \right|_{\omega_0} (\omega - \omega_0) \vec{u}. \quad (2.47)$$

We now demand  $\vec{v}$  not to change with frequency to first order except only with respect to a *global* phase and amplitude. This translates into demanding that the first order term in the Taylor series should be parallel to the

zero-th order term,

$$\left. \frac{d\vec{v}}{d\omega} \right|_{\omega_0} = iz\vec{v}(\omega_0), \quad (2.48)$$

with some complex proportionality constant  $z$ . A multiplication with  $-it^{-1}(\omega_0)$  from the left along with trivial reordering and  $\vec{v} = t\vec{u}$  yields

$$-it^{-1}(\omega_0) \left. \frac{dt}{d\omega} \right|_{\omega_0} \vec{u} = z\vec{u} \equiv \tau\vec{u}. \quad (2.49)$$

The constant  $z$  plays the role of an eigenvalue  $\tau$ , and from the eigenvalue equation (2.49), we also directly see that in the spectral vicinity of the frequency  $\omega_0$  at which the time delay matrix  $q$  in Eq. (2.45) was calculated, its eigenvectors feature the unique property of a vanishing change in the directions of their respective output vectors. Please note, that this feature of the time delay eigenstates was specifically derived already in [27] and later generalized in [28]. The authors Fan and Kahn also established the term *principal modes* (PMs) as a general appellation for the time delay eigenstates. For didactic reasons, we chose the slightly different, yet more instructive approach of the derivation above, rather than following the calculations in these papers.

The observation of the spectral output stability of the PMs together with the meaning of the generally complex eigenvalue  $\tau$ , will enable us to justify the expression (2.45) in the following. We can decompose  $\vec{v} = t\vec{u}$  for a  $q$ -eigenstate according to  $\vec{v} = |\vec{v}|\hat{v}\exp(i\varphi)$ , where we omitted the explicit dependence of its constituents on  $\omega$ . The unit vector  $\hat{v}$  determines the direction of the output vector,  $|\vec{v}|$  is of course its magnitude. As we will see, the absolute value of the phase  $\varphi$  is irrelevant, only its derivative with respect to  $\omega$  is of physical significance. We can, e.g., choose  $\varphi$  such, that at the reference frequency  $\omega_0$  its value is equal to the phase of one of the complex elements (say the  $n$ -th) of  $\vec{v}$ ,  $\text{Arg}([\vec{v}(\omega_0)]_n) = \varphi(\omega_0)$ , thus setting the  $n$ -th element of  $\hat{v}$  to a real number. Keeping the latter element purely real as frequency changes,  $\omega \neq \omega_0$ , then defines the  $\omega$ -dependence of  $\varphi$ .

Since we assumed  $\vec{u}$  to be a time delay eigenstate, we have  $d\hat{v}/d\omega = 0$  according to Eq. (2.48), leading to

$$\frac{d\vec{v}}{d\omega} = \left( \frac{1}{|\vec{v}|} \frac{d|\vec{v}|}{d\omega} + i \frac{d\varphi}{d\omega} \right) |\vec{v}| \hat{v} e^{i\varphi} = \left( \frac{d \ln(|\vec{v}|)}{d\omega} + i \frac{d\varphi}{d\omega} \right) \vec{v}. \quad (2.50)$$

A comparison to Eqs. (2.49) and (2.48) thus yields for the eigenvalue  $\tau$ ,

$$\tau = \left( \frac{d\varphi}{d\omega} - i \frac{d \ln(|\vec{v}|)}{d\omega} \right), \quad (2.51)$$

where we again used  $\vec{v} = t\vec{u}$  as well as  $d\vec{u}/d\omega = 0$ . The  $\omega$ -derivative of the global scattering phase  $\varphi$ , i.e. the real part of  $\tau$ , can be interpreted again as the delay time of the corresponding wave. The imaginary part of  $\tau$  is a measure for the change of the state's transmittivity with changing frequency. By means of a simple calculation we can further illustrate the physical significance of  $\text{Re}[\tau]$  by again investigating a time-dependent wavepacket in the upcoming subsection.

## Time-Dependent Wave Packet

We start from the expression for a temporal output pulse as the Fourier transform

$$\vec{v}(t) = \frac{1}{2\pi} \int d\omega \vec{v}(\omega) \epsilon(\omega) e^{-i\omega t}, \quad (2.52)$$

involving the spectral envelope of the input pulse  $\epsilon(\omega)$ . The parameter  $t$  in this subsection denotes the time and is not to be confused with the transmission matrix. We now assume the width of  $\epsilon(\omega)$  to be sufficiently narrow, such that the assumptions  $|\vec{v}(\omega)| \approx |\vec{v}(\omega_0)|$  for the transmittivity, and  $\varphi(\omega) \approx \varphi(\omega_0) + d\varphi/d\omega|_{\omega_0}$  for the phase in the previously introduced decomposition of the spectral output signal  $\vec{v}(\omega)$  hold. If we further assume  $\vec{v}$  to be the output vector of a  $q$ -eigenstate, we also have  $\hat{v}(\omega) \approx \hat{v}(\omega_0)$ , due to  $d\hat{v}/d\omega = 0|_{\omega_0}$ , hence

$$\vec{v}(\omega) \approx |\vec{v}(\omega_0)| \hat{v}(\omega_0) e^{i\varphi(\omega_0) + i \frac{d\varphi}{d\omega}|_{\omega_0} \omega}. \quad (2.53)$$

Please note that typically the phase rotates much faster with frequency than a change in the transmittivity occurs, therefore, we considered the expansions to first order for the phase, and only to zero-th order for the magnitude, respectively. Inserting Eq. (2.53) into Eq. (2.52) we get for the total output intensity

$$\begin{aligned} |\vec{v}(t)|^2 &= \frac{|\vec{v}(\omega_0)|^2}{(2\pi)^2} \int d\omega' \int d\omega \epsilon^*(\omega') \epsilon(\omega) e^{-i(\omega-\omega') \left( t - \frac{d\varphi}{d\omega}|_{\omega_0} \right)} \\ &= \frac{|\vec{v}(\omega_0)|^2}{(2\pi)^2} \left| \int d\omega \epsilon(\omega) e^{-i\omega \left( t - \frac{d\varphi}{d\omega}|_{\omega_0} \right)} \right|^2 \\ &= |\vec{v}(\omega_0)|^2 \left| \epsilon \left( t - \frac{d\varphi}{d\omega}|_{\omega_0} \right) \right|^2, \end{aligned} \quad (2.54)$$

where we have used  $\hat{v}^\dagger \hat{v} = 1$ . Eq. (2.54) states that for a time delay eigenstate in combination with an adequately narrow envelope  $\epsilon(\omega)$  of the input

packet, the temporal output pulse is just a rescaled and delayed version of the input pulse. The temporal shift in turn is exactly the real part of the corresponding eigenvalue  $\tau$  in (2.49), and is given by the frequency derivative of the global output scattering phase.

Please note that all considerations discussed in this section equally apply not only to  $q$ , but also to the Wigner-Smith time delay operator  $Q$ , for the latter being just a special case of the general expression for  $q$  in Eq. (2.45).

## Construction Scheme for Non-Invertible Scattering Matrices

For the construction of the time delay operator  $q = -i t^{-1}(\omega_0) dt/d\omega|_{\omega_0}$  in Eq. (2.45), the inverse of the transmission matrix  $t$  at  $\omega_0$  is needed. A straight-forward inversion is generally not possible, because  $t(\omega_0)$  might be a singular matrix and/or may not even be quadratic. In this subsection, we present an algorithm that produces an effective inverse, irrespective of the shape or singularity of  $t(\omega_0)$ , that preserves the desired features of the principal modes, i.e., the  $q$ -eigenstates. Since we have used this inversion scheme to achieve many of the results presented in the next chapter, we will discuss all necessary steps of the procedure in detail in what follows.

In a first step we perform a singular value decomposition (SVD) of  $t(\omega_0)$ ,

$$t(\omega_0) = U \Sigma V^\dagger, \quad (2.55)$$

where the matrices  $U$  and  $V$  contain column-wise the left and right singular vectors, respectively. The diagonal matrix  $\Sigma = \text{diag}(\{\sigma_n\})$  contains the (real and positive) singular values of  $t(\omega_0)$ . In order to eliminate possible singularities, or more general, (dark) channels that contribute only weakly to the total output, we only keep those  $N_{\text{bright}}$  singular values and the corresponding left and right singular vectors, where  $\{\sigma_n > \sigma_{\text{thr}}\}$ , with  $\sigma_{\text{thr}}$  being a reasonably chosen threshold value. Accordingly, this leads to the matrices of reduced dimensions,  $\tilde{U}$ ,  $\tilde{V}$ , and  $\tilde{\Sigma} = \text{diag}(\{\sigma_n > \sigma_{\text{thr}}\})$ .

The next step is projecting the transmission matrix onto the reduced subspace spanned by these remaining (bright) channels,

$$\tilde{t}(\omega_0) = \tilde{U}^\dagger t(\omega_0) \tilde{V}, \quad (2.56)$$

resulting in the non-singular, quadratic and, therefore, invertible  $N_{\text{bright}} \times N_{\text{bright}}$  matrix  $\tilde{t}(\omega_0)$ . The effective inverse is finally obtained by inversion

and subsequent reprojection onto the original vectorspace,

$$\begin{aligned} t_b^{-1}(\omega_0) &:= \tilde{V} \tilde{t}^{-1}(\omega_0) \tilde{U}^\dagger \\ &= \tilde{V} \left( \tilde{U}^\dagger t(\omega_0) \tilde{V} \right)^{-1} \tilde{U}^\dagger, \end{aligned} \quad (2.57)$$

where the subscript  $b$  stands for 'bright'. We found that a projection onto the subspace of bright channels, thus 'cutting' away the dark channels, is favorable in many cases, not only in order to compute an effective inverse of  $t$  (see, e.g., section 3.4). For that reason, we also introduce the projected transmission matrix,

$$t_b(\omega) := \tilde{U} \tilde{U}^\dagger t(\omega) \tilde{V} \tilde{V}^\dagger. \quad (2.58)$$

Please note that, since  $\tilde{U}^\dagger \tilde{U} = \mathbb{1}$  and  $\tilde{V}^\dagger \tilde{V} = \mathbb{1}$ , the effective inverse we defined in Eq. (2.57) and the projected matrix in Eq. (2.58) satisfy the calculation rules  $t_b^{-1}(\omega_0) t_b(\omega_0) t_b^{-1}(\omega_0) = t_b(\omega_0)$ , and  $t_b(\omega_0) t_b^{-1}(\omega_0) t_b(\omega_0) = t_b^{-1}(\omega_0)$  for pseudo-inverse matrices. The products of the two matrices give  $t_b(\omega_0) t_b^{-1}(\omega_0) = \tilde{U} \tilde{U}^\dagger$  and  $t_b^{-1}(\omega_0) t_b(\omega_0) = \tilde{V} \tilde{V}^\dagger$ , respectively, where the projectors  $\tilde{U} \tilde{U}^\dagger$  and  $\tilde{V} \tilde{V}^\dagger$  can be viewed as the representations of the unit matrices in the bright left and right subspaces the transmission matrix is projected onto.

Concludingly, we can generalize the construction of the time delay matrix  $q$ ,

$$q = -i t_b^{-1} \frac{dt_b}{d\omega}, \quad (2.59)$$

which is equal to our previous expression in Eq. (2.45) in case of  $N_{\text{bright}} = N$ , since then  $t_b = t$ . The matrices  $t_b$  and  $t_b^{-1}$ , respectively, directly inherit the physical information about the scattering process corresponding to the bright channels from  $t$ , the dark channels span the common nullspace of both matrices. We can thus assert, that all statements about the favorable properties concerning the eigenvalues and eigenstates of the time delay matrix in Eq. (2.45) also apply to the operator (2.59), when it comes to the relevant subspace of bright transmission channels.

## 2.5 The Dwell Time

In this section we briefly discuss another, widely known and used concept of time delay in wave transport, the so-called *dwell time*. The definition of the dwell time is generally different from the quantity based on the derivative of the scattering phases, which is also often referred to as *group delay* and measured by the operators  $Q$  and  $q$  we discussed in the preceding sections. In case of flux-conserving scattering processes, however, a direct and close connection between the operators corresponding to the group delay and the dwell time exists, as we will show below.

First suggested by Smith already in 1960 [19] and later picked up by Büttiker [62], the dwell time for a temporal wave packet has a conveniently simple definition (see also [21]),

$$\tau_d = \int dt \frac{U_\Omega(t)}{U_{\text{tot}}} \quad (2.60)$$

where  $U_\Omega(t)$  is the amount of the packet's energy stored inside the finite scattering system  $\Omega$  as a function of time. For reasons of simplicity, we assumed the total energy  $U_{\text{tot}}$  to be conserved in time, and the pulse is located entirely outside of  $\Omega$  for  $t \rightarrow \pm\infty$ . The dwell time  $\tau_d$  is thus just the average time a certain fraction of energy injected into the system dwells inside this system, irrespective of the specific channels it was injected in and is ultimately scattered into. For a stationary scattering state  $\psi(\vec{x})$ , and  $\vec{\xi} = \vec{x} \in \partial\Omega$ , Eq. (2.60) translates into

$$\tau_d = \frac{U_\Omega}{S_{\partial\Omega}^{(\text{in})}} = \frac{2k}{ic} \frac{\int_\Omega dV \psi^*(\vec{x}) n^2(\vec{x}) \psi(\vec{x})}{\int_{\partial\Omega} d\vec{A} \cdot (\psi(\vec{\xi}) \vec{\nabla} \psi^*(\vec{\xi}) + \text{c.c.})} \quad (2.61)$$

where we used the expressions for the now time-averaged stored energy,

$$U_\Omega = \frac{1}{2} \epsilon_0 \int_\Omega dV \psi^*(\vec{x}) n^2(\vec{x}) \psi(\vec{x}), \quad (2.62)$$

and for the incoming power,

$$S_{\partial\Omega}^{(\text{in})} = \frac{1}{2} \epsilon_0 \frac{ic}{2k} \int_{\partial\Omega} d\vec{A} \cdot (\psi(\vec{\xi}) \vec{\nabla} \psi^*(\vec{\xi}) + \text{c.c.}), \quad (2.63)$$

respectively (see appendix A.2). The symbol  $\epsilon_0$  in the above equations denotes the vacuum permittivity, and  $c$  is the speed of light. We can use the normalization of the field  $\psi(\vec{x})$  according to,

$$\frac{i}{2} \int_{\partial\Omega} d\vec{A} \cdot (\psi(\vec{\xi}) \vec{\nabla} \psi^*(\vec{\xi}) + \text{c.c.}) = 1, \quad \rightarrow \quad S_{\partial\Omega}^{(\text{in})} = \frac{\epsilon_0 c}{2k}, \quad (2.64)$$

in order to express the dwell time like

$$\tau_d = \frac{2k}{\epsilon_0 c} U_\Omega = \frac{k}{c} \int_\Omega dV \psi^*(\vec{x}) n^2(\vec{x}) \psi(\vec{x}). \quad (2.65)$$

Much literature on the relation of group delay and dwell time for different types of waves and systems exists, see for example [63–65], however, few works on a mathematical operator measuring the dwell time can be found, e.g., [24, 66]. Abusing the normalization stated in Eq. (2.64) as well as a simplified matrix notation, we can write for the wave function  $\psi(\vec{x})$  in Eq. (2.65) inside the scattering region,  $\vec{x} \in \Omega$  (see [42, 44, 67]),

$$\vec{\psi} = 2i G V \vec{u}, \quad (2.66)$$

where we used the Green's function  $G$  and the coupling matrix  $V$  from Eq. (2.3), respectively. The vector object  $\vec{u}$  again contains the complex input coefficients. Hence, we can write for the dwell time of a particular input state characterized by  $\vec{u}$ ,

$$\tau_d = \frac{k}{c} \vec{u}^\dagger [4 V^\dagger G^\dagger n^2 G V] \vec{u}, \quad (2.67)$$

and identify the object  $Q_d := 4k V^\dagger G^\dagger n^2 G V/c$  as the dwell time operator. It was demonstrated for the Schrödinger equation that a direct link between  $Q_d$  and the Wigner-Smith operator  $Q$  can be drawn [66]. As we have already shown elsewhere putting these results on a solid physical ground [44], one can even analytically derive the discrepancy  $Q_d - Q$  in terms of the scattering amplitudes. Nevertheless following the mathematically correct derivation in [66], the desired connection can be found by neglecting the frequency dependence of the coupling matrix  $V$ , when calculating the derivative  $dS/d\omega$  in the construction of  $Q$ . Redoing the respective derivations for the Helmholtz equation analogously yields (appendix A.2),

$$Q_d \approx Q, \quad (2.68)$$

a correspondence that we will make use of at some later points in section 3.3 of this thesis. Concludingly, we would like to point out to the reader, that also an interesting connection between  $\tau_d$  and the DOS can be found [68],

$$\langle \tau_d(\omega) \rangle = \frac{2\pi}{N} \rho(\omega), \quad (2.69)$$

where we translated the corresponding expression in [68] to the Helmholtz equation using the dispersion relation of a free Schrödinger particle  $E = k^2/2$  (in reduced units). Together with Eq. (2.68), Eq. (2.69) thus further justifies the assumptions for the DOS made in the derivation of Eq. (2.38).

## 2.6 General Class of Dependence Shift (DEFT) Operators

Referring back to the calculations in subsection 2.4, we realize, at first on a purely mathematical level, that the construction of a Hermitian operator resulting from a unitary scattering matrix does not necessarily have to involve a derivative with respect to the frequency  $\omega$  (as in the Wigner-Smith time delay operator). Correspondingly, we can thus directly generalize Eqs.(2.49) and (2.51) expressing the eigenvalue equation and the meaning of the corresponding eigenvalues for the time delay matrix  $q$ , respectively, to arbitrary scalar quantities  $a$ , that the scattering matrix parametrically depends on,  $S = S(a)$ . In analogy to the properties of the principal modes, the eigenstates of the operator

$$D_a := -iS^\dagger \frac{dS}{da}, \quad (2.70)$$

or more generally,

$$d_a := -it^{-1} \frac{dt}{da}, \quad (2.71)$$

feature a static output intensity pattern to first order, when varying the parameter  $a$ . These generalizations of the Wigner-Smith time delay operator  $Q$  and the general time delay matrix  $q$  to a whole new class of operators constitute one of the major analytical results in this thesis. We emphasize again, that  $a$  stands for literally *any* parametrical dependence of the scattering amplitudes. Just a few physically relevant examples of  $a$  might be an external magnetic field  $B$  in the scattering of charged particles, or geometrical parameters of the scattering region, e.g. its position or the position of one specific scattering element, as we will demonstrate in section 3.5. In analogy to the eigenvalues of the time delay operators, i.e., the proper delay times, the eigenvalues of  $D_a$  and  $d_a$  describe the *proper shifts* in the canonically conjugate quantity of  $a$ , as we will show in the remainder of this section. Decomposing the output for a  $d_a$ -eigenstate  $\vec{u}$  again as  $\vec{v}(a) = |\vec{v}(a)|\hat{v}(a) \exp(i\varphi(a))$ , analogously to the derivation of Eq. (2.51) we find for the eigenvalue  $\kappa_a$

$$d_a \vec{u} = -it^{-1} \frac{dt}{da} \vec{u} = \kappa_a \vec{u} \quad \rightarrow \quad \kappa_a = \left( \frac{d\varphi}{da} - i \frac{d \ln(|\vec{v}|)}{da} \right), \quad (2.72)$$

and

$$\frac{d\hat{v}}{da} = 0 \quad (2.73)$$

for the output pattern, respectively. For a unitary scattering matrix, we can derive an even simpler form than Eq. (2.70) for the operator  $D_a$  that

elegantly generalizes the Wigner-Smith operator, displaying the aforementioned shift in the conjugate variable of  $a$ , which is represented by the operator  $\hat{k}_a := -i\partial/\partial a$ .

In case the parameter  $a$  affects the entire scattering region, and/or also the coupling or the scattering channels depend(s) on  $a$ ,  $V = V(a)$ ,  $\chi_n = \chi_n(a)$ , the elements of the matrix representation  $k_a$  can be calculated using the (normalized) transverse profiles of the scattering channels  $\chi_n$  according to

$$[k_a]_{mn} = -i \int_{\partial\Omega} d\xi \chi_m^*(\xi) \frac{\partial \chi_n}{\partial a}(\xi), \quad (2.74)$$

with  $\{\xi: \vec{x} \in \partial\Omega\}$  indicating a position along the boundary of the scattering region. The scattering matrix  $S(a + \Delta a)$  at  $a' = a + \Delta a$  can then be calculated in terms of  $S(a)$  using the 'evolution' operator  $\exp(ik_a \Delta a)$ , where  $k_a$ , acts as the accurate generator,

$$S(a + \Delta a) = e^{-ik_a \Delta a} S(a) e^{ik_a \Delta a}. \quad (2.75)$$

For small deviations  $\Delta a$ , we can approximate Eq. (2.75)

$$\begin{aligned} S(a + \Delta a) &\approx (\mathbb{1} - ik_a \Delta a) S(a) (\mathbb{1} + ik_a \Delta a) \\ &\approx S(a) - ik_a S(a) \Delta a + iS(a) k_a \Delta a, \end{aligned} \quad (2.76)$$

where we neglected terms of the order  $(\Delta a)^n$  with  $n \geq 2$ . Using Eq. (2.76), we can write the derivative of  $S$  with respect to  $a$  as the limit

$$\frac{dS}{da} = \lim_{\Delta a \rightarrow 0} \frac{S(a + \Delta a) - S(a)}{\Delta a} = -ik_a S(a) + iS(a) k_a. \quad (2.77)$$

With  $S^\dagger S = \mathbb{1}$ , it then follows for the  $D_a$ -operator

$$D_a = -iS^\dagger \frac{dS}{da} = k_a - S^\dagger k_a S. \quad (2.78)$$

From Eq. (2.78) one can easily see, that the expectation value of  $D_a$  for an arbitrary input state evaluates to the difference of the expectation values for  $k_a$  before and after the scattering process. In this way, we found a general expression for an operator measuring the shift in  $k_a$  experienced by the wave, which is induced by the scattering process. The quantity  $k_a$  (now as a variable, not an operator) is the canonical-conjugate parameter of the variate  $a$  the scattering setup depends on. Mathematically speaking,  $S(a)$  and  $D_a$  are basis-independent, abstract operators, e.g., the Fourier transform  $\tilde{S}(k_a)$  is equivalent to  $S(a)$ , in this respect. Hence, we can also view the scattering amplitudes as being parametrically dependent on  $k_a$ , rather than on  $a$ . Briefly summarizing these considerations, we termed our newly found and very general class of operators dependence shift (DEFT) operators.



CHAPTER 3 

**Numerical & Experimental  
Results and Applications**

This chapter is dedicated to the application of the notions and results presented in the last chapter. For all discussed projects, we will elaborate a solid theoretical framework based on these concepts, along with either a numerical backup of our claims, or a presentation of measurement results, directly.

In the upcoming section, we will treat systems allowing for so-called *branched flow*. We will show that the branches in the spreading pattern of an injected wave evolving in such a system can conveniently be separated from each other by properly shaping the input wavefront. Our corresponding algorithm involves the construction of a time delay operator along the lines of the derivations in the preceding chapter.

The section thereafter discusses the possibility of effectively camouflaging even strongly scattering disorder potentials by means of recording the impinging wavefront and tailoring the signal ultimately ejected into the disordered region.

Subsequently, we present the proper generalization and applicability of the *mean chord length theorem* to wave propagation. This will allow us to show that an invariant average scattering delay time exists, which is independent of the scattering regime, ranging from ballistic to localized transport. Briefly, we will also discuss a connection to a fundamental result in the context of solar cells, i.e., the *Yablonovitch limit*.

Thereafter, we will present a novel optimization algorithm that may increase the data transfer capacities of multimode optical fibers. This project has been carried out in collaboration with Hui Cao's group at Yale University, enabling us to present a direct verification by means of a successful experimental realization.

The last section eventually introduces a specific example for the general (DEFT) operator class defined at the end of the previous chapter. The involved derivative of the scattering matrix will be taken with respect to the spatial position of a single scatterer, or to the position of the entire scattering region, respectively. The former variation leads to an algorithm which can be used to either focus on a specific scattering element or, quite on the contrary, to avoid a certain region, as we could demonstrate in a microwave setup operated by Ulrich Kuhl's group at the University of Nice. After discussing the connection of the concepts applied there to a recent experiment in the optical domain, we will evince, in a numerical study, that shifting the whole scattering region allows for a separation of wave states 'living' on regular islands from states corresponding to the chaotic sea in systems possessing a mixed (regular-chaotic) phase space of classical (trajectory) dynamics.

### 3.1 Coherent Control of Branched Flow

Branched flow is a fundamental, universal phenomenon occurring in the propagation of both, waves and particles. In wave transport, it arises over a huge range of wavelengths and for many different types of waves, where it specifically denotes the propagation of an initially constricted wavefront along distinct branches rather than a smooth, fan-like spreading. This peculiar ramification is where the term 'branched' flow stems from. First described only quite recently in 2001 for electronic transport through semiconductor nanostructures [31], the discovery of branched flow sparked a remarkable scientific activity revealing its occurrence from the nanoscale to microwaves [69] and even up to ocean waves [70,71]. It thus spans about 12 orders of magnitude in wavelength. The key prerequisite is the presence of a weak and smooth background potential accounting for the formation of branches in the scattering pattern of the respective waves in such systems. As could be shown, the latter effect can largely be understood in terms of caustics viewing the disorder landscape as an effective array of imperfect lenses [72,73]. Not only its origin but also the statistics of branched flow were subject to scientific investigation [74,75], however, to our best knowledge, no work on deliberately controlling specific transport properties of systems allowing for branched flow has so far been put forward. An experimental control of the phenomenon would constitute an important step forward in the context of imaging through disordered tissues, or might be beneficial for an energy-efficient transmission in random media. In this section, we will show that one can actually select individual branches by means of shaping the incident wavefront, hence conveniently exploiting the system-specific branch structure leading to highly collimated beams. The presented results were achieved in collaboration with Adrian Girschik and Andre Brandstötter.

Since a spatially dependent tailoring of the optical refractive index was experimentally achieved very recently [76], we will also demonstrate our findings in this section in the context of the Helmholtz equation (2.2). For our numerical studies, we investigated a specific, two-dimensional realization of a branched flow system which is shown in Fig. 3.1(a). The scattering region of length  $l$  containing the non-uniform refractive index distribution  $n(\vec{x})$  is attached to two semi-infinite waveguides of the same width  $w$  featuring  $n(\vec{x}) \equiv 1$ . The (left) incoming lead and the disorder potential are separated by an aperture of width  $w_a = 0.25 \times w$ . The boundaries of the entire system in transverse direction as well as the aperture are assumed to be perfectly reflecting (hard) walls, accordingly, the waveguide modes inside the leads take the simple form given by Eq. (2.5) in the last chap-

ter. We choose a vacuum wavenumber of  $k = 2\pi/\lambda = 200.1\pi/w$ , thus 200 and 50 propagating modes are open in the waveguide and in the aperture, respectively.

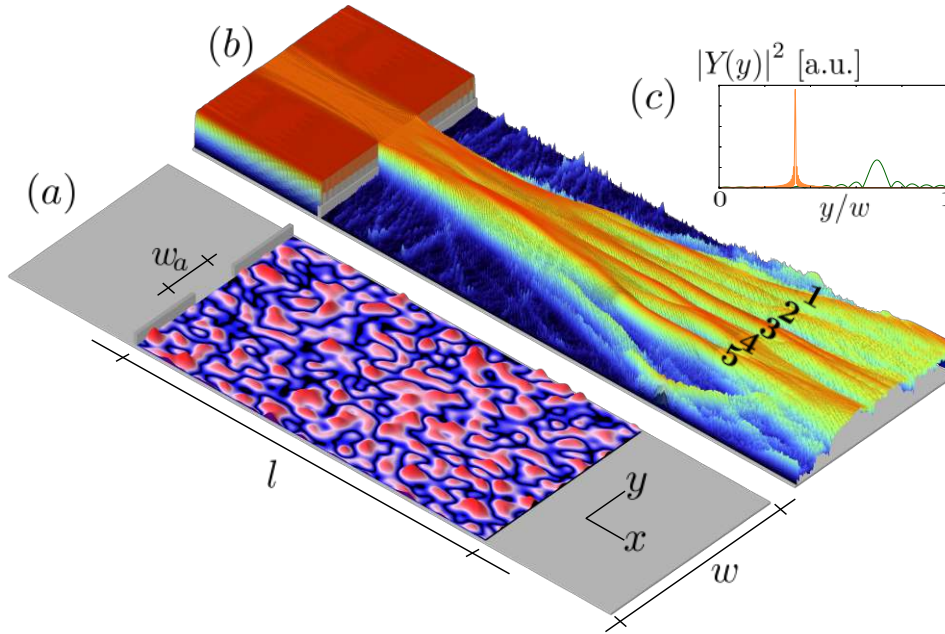


**Figure 3.1:** (a) Sketch of the system allowing for branched flow. The scattering region (length  $l$ ) is attached to two semi-infinite leads of width  $w$  and an index of refraction of  $n(\vec{x}) \equiv 1$ . Flux is injected through the left lead. An aperture with an opening of  $w_a = 0.25 \times w$  separates the incoming waveguide from the disorder landscape (colored region). The color code of the disorder potential is chosen such that red means a high refractive index  $n(\vec{x})$ . (b) Intensity plot of the incoherent superposition of the first 25 waveguide modes injected from the left. The color code is logarithmic, where high intensity regions are shown in red. 5 main branches can be identified and are numbered accordingly. The underlying effective potential causing the branching matches exactly the one shown in (a). (c) Eigenfunctions  $Y(y)$  in real space of the  $\hat{y}$ -operator in the subspace of flux-carrying modes for 15 (green) and our chosen number of 200 open modes (orange), respectively.

The long-ranged effective potential is characterized by its Gaussian auto-correlation function

$$C(|\vec{x} - \vec{x}'|) = \langle (n^2(\vec{x}) - 1) (n^2(\vec{x}') - 1) \rangle_x \propto e^{-\frac{|\vec{x} - \vec{x}'|}{2l_{\text{corr}}}}, \quad (3.1)$$

where we chose the correlation length to be of the order of the wavelength,  $l_{\text{corr}} = 3\lambda$ . In order to ensure the necessary weakness of the disorder, we set the occurring maximum index to  $n_{\text{max}} = 1.1$ . The system-inherent branch structure is made visible by an incoherent superposition,

$$\Psi(\vec{x}) = \sum_n |\psi_n(\vec{x})|^2, \quad (3.2)$$

of the wavefunctions  $\psi_n(\vec{x})$  corresponding to the lowest 25 lead modes in Fig. 3.1(b). We can clearly identify 5 main branches, to which we will refer to as branches 1-5 in the following.

The full scattering matrix of this 2-port system can be subdivided into reflection and transmission matrices according to Eq. (2.4). As we will see, it might also be beneficial to further decompose the transmission matrix  $t$  describing transport from left to right in our notation. Especially in a possible experiment in the optical domain, usually a vast number of modes is open, such that it is not possible to even measure the full transmission matrix using current state-of-the-art devices. One would rather record only subparts of  $t$  corresponding to a transmission into only a (spatial) fraction of the total output facet. Numerically, we can follow a very similar approach by transforming the transmission matrix into a real-space basis,

$$t_\xi = \Xi^\dagger t \Xi, \quad (3.3)$$

making use of the unitary matrix  $\Xi$  containing the eigenvectors of the operator  $\hat{\xi}$ . The latter operator measures the transverse spatial coordinate along the boundary of the scattering region (for a three-dimensional rather than a two-dimensional system,  $\xi$  then stands for one of the two coordinates on the surface of the scattering volume). In case of a transformation from the scattering basis into the real-space basis, the matrix elements of the  $\hat{\xi}$  are calculated like

$$\begin{aligned} \xi_{mn} &= \int_{\partial\Omega} d\xi \chi_m^*(\xi) \xi \chi_n(\xi) \\ &= \frac{2}{w} \int_0^w dy \sin(k_{y,m}y) y \sin(k_{y,n}y) = y_{mn}, \end{aligned} \quad (3.4)$$

where we used  $\xi = y$  and  $\partial\Omega = [0, w]$  for our specific geometry, as well as Eq. (2.5) for the normalized transverse profiles of the lead modes. The eigenfunctions of the operator  $\hat{y}$  can be viewed the projections of Dirac  $\delta$ -functions onto the subspace of flux-carrying channels. The more modes are open, the closer is their resemblance to actual  $\delta$ -functions, as can be seen in Fig. 3.1(c). The respective eigenvalues coincide with the spatial positions

of the maxima of the eigenfunctions in real space. Following Eq. (3.4) and grouping the eigenvectors of the  $y$ -matrix as the columns of the (unitary) matrix  $Y$ , we thus get the transformed transmission matrix  $t_y = Y^\dagger t Y$ .

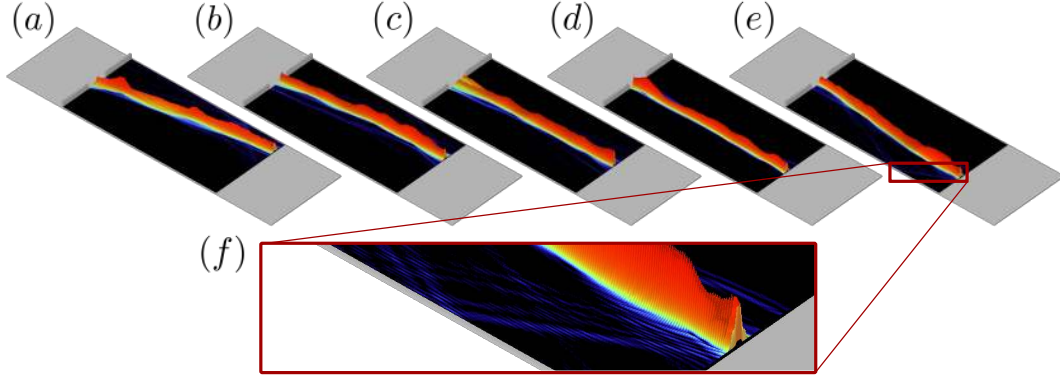


**Figure 3.2:** (a)-(e) Intensities of the eigenstates of the respective operators  $s_y^\dagger s_y$  for the main branches 1-5 marked in Fig. 3.1(b). The shown states are those with the highest transmissions into the chosen spatial fraction of the output facet. (f) A zoom on branch 5 shown in (e). Also paths reflected off the lower wall which are not along the desired branch contribute.

The experimental procedure we suggest now works as follows: In a first step, not further specified wavefronts are injected, the intensity profile at the output facet is coarsely scanned, and the positions where branches hit the output plane are recorded. The next step is a phase-coherent measurement of those parts of the transmission matrix connecting the input aperture and the output position of a chosen branch. Numerically this step translates into 'cutting' the proper scattering amplitudes from the matrix  $t_y$ , and we will denote the resulting sub-matrix as  $s_y$ . To give an example, for branch 5 we used the region  $y \in [0.23, 0.37] w$ , and took only those parts of  $t_y$  that correspond to  $\hat{y}$ -eigenfunctions at the output with eigenvalues within this interval. In a final step, the matrix  $s_y^\dagger s_y$  and its eigenvectors are computed. What  $s_y^\dagger s_y$  measures is the transmittivity from the input into the chosen output region, so the eigenfunctions belonging to those eigenvectors that correspond to the highest eigenvalues should, therefore, also correspond to the chosen branch. As can be seen from Fig. (3.2)(a)-(e), a pretty good separation of the 5 individual branches in our system can already be achieved by this conceptually rather simple procedure. For the state corresponding to branch 5, however, we see that not only paths along the desired branch contribute to the total output intensity but also paths reflected off the lower wall (see Fig. (3.2)(f)). Although the latter contribution is relatively small

here, we expect a much more complicated branch structure to evolve in a real experiment generically featuring a much large number of open modes. In this case, a separation of individual branches might not be possible just according to their transmittivity into a particular spatial region, since then two or even more major branches may end in the same region.

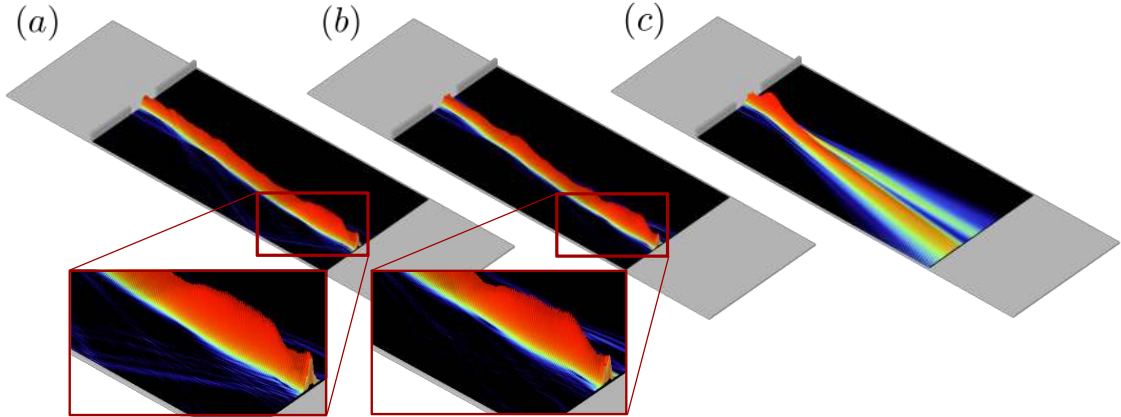


**Figure 3.3:** (a)  $s_y^\dagger s_y$ -eigenstate addressing branch 5, (b) the corresponding  $q_s$ -eigenstate. From the insets, one can clearly see, that the unwanted contributions in (a) are strongly suppressed in (b). (c) Same input pattern as in (b), but injected into a system lacking the non-homogeneous distribution of the index of refraction.

As we have already shown in an earlier work [30], the time delay operator is a suitable and convenient tool when it comes to separate different bundles of classical paths. The underlying functional principle is that different bundles might end up in the same region of space, but they do not share the same delay time unless they also possess the exact same length. With the mathematical instruments provided in section 2.4 of the last chapter, we can now construct a time delay operator using the proper  $s_y$ -matrix for branch 5 as follows

$$q_s = -i s_{y(b)}^{-1} \frac{d s_{y(b)}}{d\omega}. \quad (3.5)$$

In analogy to the derivation of Eq. (2.59), we projected  $s_y$  onto the bright transmission channels in order to get  $s_{y(b)}$  and the effective inverse  $s_{y(b)}^{-1}$ . In this case here, however, we chose a rather high threshold for the singular values that defines the dimension of the bright subspace of  $\sigma_n > 0.8$ , since we are only interested in states strongly transmitting into the chosen region. Please note, that the squared singular values of  $s_y$ ,  $\{\sigma_n^2\}$ , are exactly the eigenvalues of  $s_y^\dagger s_y$ . Diagonalizing  $q_s$  yields the desired unmixing of branch 5

and the unwanted contributions. In Fig. 3.3(a),(b), we show a comparison of the associated eigenstates of the  $s_y^\dagger s_y$  and  $q_s$  matrices, where we can clearly see, that in the latter state, the undesirable paths are suppressed.

Concludingly, after having demonstrated the possibility of selecting individual branches in a branched flow system utilizing the scattering matrix formalism and our concepts of time delay, we will now show, that the respective intensity distributions along single branches result from a very delicate interplay of the inhomogenous refractive index distribution in the system and a proper shaping of the incident wavefront. In order to do so, we show in Fig. 3.3(c) the intensity plot for the wavefunction of the  $q_s$ -eigenstate shown in (b) injected into the same geometry but assuming a homogeneous refractive index distribution of  $n(\vec{x}) \equiv 1$  inside. As is clearly visible in Fig. 3.3(c), the typical fan-like spreading of the wavefront sets in, thus proving that the states presented in this section are non-trivial superpositions of input channels, rather than just input patterns corresponding to some specific, but trivial injection angles.

## 3.2 Camouflage by Wavefront Shaping

Recording a system's transmission matrix, together with the ability to shape the input wavefront, in principle enables one to effectively cloak an arbitrary system by mimicking the presence of a different reference system, as we will discuss in this section. In contrast to a cloaking by means of tailoring the refractive index distribution using so-called metamaterials [77–79], the camouflage algorithm we will present in the following tackles this problem by modulating the impinging wave rather than the scattering system itself. Our approach thus allows for a 'non-invasive' camouflage, since only the transmission amplitudes need to be measured, as we will show. Moreover our concept is largely independent of the actual shape or internal structure of the region that is to be hidden. Preliminary results preceding those presented here were achieved in collaboration with Stephan Steinhauer who wrote his bachelor thesis on this topic that I co-advised [80].

Let the transmission matrices of the bogus reference system we want to suggest, and the existent actual system be denoted by  $t_{\text{ref}}$  and  $t_{\text{act}}$ , respectively. For a given input configuration described by the vector  $\vec{u}$ , the output in the reference system would read

$$\vec{v} = t_{\text{ref}} \vec{u}. \quad (3.6)$$

The same wavefront injected into the actual system, generally produces, of course, a completely different output pattern. In most cases, however, there exists a proper input vector  $\vec{u}'$  leading to the same output vector,

$$\vec{v} = t_{\text{act}} \vec{u}'. \quad (3.7)$$

Since we are searching for the proper input configuration for the bogus system that leads to a specific output vector  $\vec{v}$ , we combine Eqs. (3.6) and (3.7). Doing so, we see that we already arrive at the general construction procedure for the desired configuration  $\vec{u}'$ ,

$$\vec{u}' = t_{\text{act}}^{-1} t_{\text{ref}} \vec{u}. \quad (3.8)$$

We now envision a cloaking device that records the incoming wavefront encoded by  $\vec{u}$ , calculates, and subsequently injects the new input  $\vec{u}'$  under usage of Eq. (3.8), where we assume both of the involved transmission matrices to be known from previous measurements. In this way, the device would manage to dupe a possible spectator with the output image corresponding to the reference system, thus hiding the actual one.

We numerically tested our analytical findings on the system displayed in Fig. 3.4(a): A quadratic hard-wall resonator of length  $L$  is connected to

two diagonally opposite waveguides of width  $w = 0.25 L$ . The refractive index is that of an empty cavity,  $n(\vec{x}) \equiv 1$ . As a challenging example for an input state  $\vec{u}$  that we want to use for demonstration purposes, we chose a particlelike state existing in such a system (see [30] and also the previous section as well as section 3.5) that connects the two leads as a highly collimated beam from left to right. The corresponding intensity pattern is shown in Fig. 3.4(b). The actual system we will try to camouflage shares the geometry of our reference, but features a rather strong and short-ranged correlated disorder inside the quadratic cavity, that is characterized by a refractive index  $n(\vec{x}) \geq 1$  and the correlation function given in Eq. (3.1). The correlation length is  $l_{\text{corr}} = 0.5 \lambda$ , where the wavelength  $\lambda = 2\pi/k$  is that of the impinging wave. We chose  $k = 50.5 \pi/w$ , so 50 propagating modes are open in the leads. The maximum of occurring values of the index of refraction is  $n_{\text{max}} = 2.0$ .

The next step of our procedure would be applying Eq. (3.8) in order to get the desired vector  $\vec{u}'$ . From Eq. (3.8), we immediately see though, that  $\vec{u}'$  can only be computed strictly in case of an invertible transmission matrix  $t_{\text{act}}$ . Furthermore, even in cases where  $t_{\text{act}}$  is quadratic and non-singular, a direct experimental implementation would still not be feasible. If one or several of the singular values of  $t_{\text{act}}$  are close to zero,  $\sigma_n \approx 0$ , which is the generic case in a strongly scattering optical medium featuring a typical number of around 10 million transversal modes open per  $\text{mm}^2$  [6], an initially normalized signal  $\vec{u}$  would produce a vector  $\vec{u}'$  of very high magnitude. This means an unnecessarily high amount of energy would be sent into the system of which only a fraction contributes to the actual output pattern. A certain inevitable level of noise under experimental conditions additionally causes a direct inversion of the transmission matrix to grow unstable [10,11,81]. Fig. 3.4(c) shows the intensity scattering pattern for the initial wavefront computed according to (3.8). As can clearly be seen, the vast majority of energy is stored inside the cavity and ultimately reflected back into the incoming lead. Since the direct inversion of  $t_{\text{act}}$  is numerically possible, the output image is a perfect reconstruction for the particlelike output shown in (b), though. The situation worsens drastically when adding a random noise matrix to  $t_{\text{act}}$ ,

$$t_{\text{act},ij}^{\eta} = t_{\text{act},ij} + \eta e^{i\varphi_{\eta}}. \quad (3.9)$$

To each of the scattering amplitudes, we add a different random complex number, with a phase  $\varphi_{\eta} \in [0, 2\pi]$ , and a maximum noise amplitude of 1% of the largest singular value  $\sigma_{\text{max}}$ ,  $\eta \in 0.01[0, \sigma_{\text{max}}]$ , drawn from uniform distributions. From Fig. 3.4(e), we see that not only much of the injected intensity is again lost unspent, but also the reconstruction of the expected

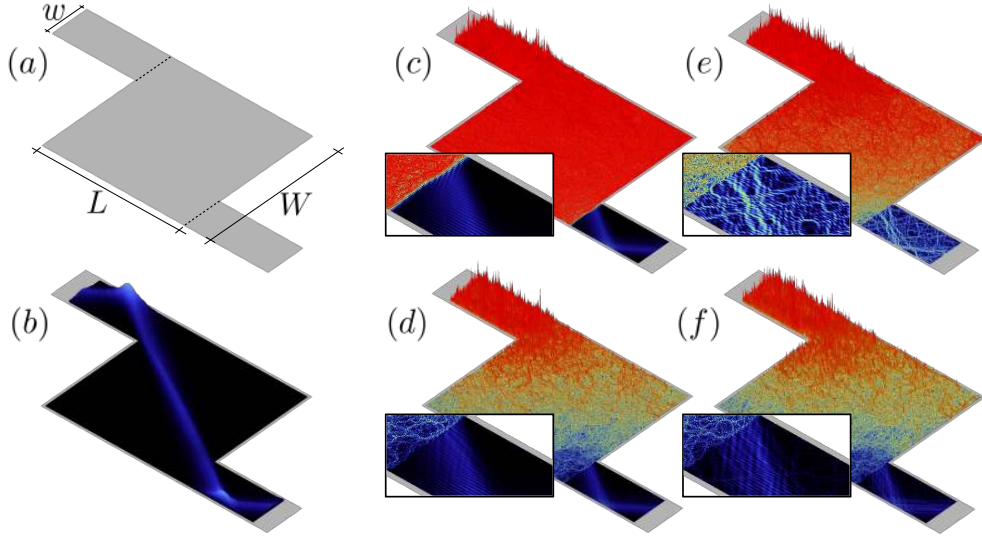


**Figure 3.4:** A resonator of width  $W$  and length  $L = W$  is coupled to two semi-infinite waveguides of width  $w$ . The wave is injected through the left lead. (a) Sketch of the system; the transmission matrix from left to right is evaluated between the dotted lines. (b)-(f) Wave intensity plots on a logarithmic color scale, where red means high intensity. The smaller insets in (c)-(f) display zooms on the output facet. (b) A highly collimated, particlelike intensity pattern generated inside the empty cavity. (c) State produced by a direct inversion of the transmission matrix of the disordered, actual system without noise (see main text). (d) State produced using the effective inversion injected into the same system (see main text). (e) State produced by directly inverting the noisy transmission matrix in Eq. (3.9); the desired output pattern is completely destroyed. (f) Corresponding state exploiting the effective inverse, the collimated output pattern is still clearly visible.

output pattern has completely failed for the case of a non-zero noise level. A direct application of Eq. (3.8) to the experiment is thus not recommendable.

Rescue arrives in form of our generalized inversion scheme introduced in section 2.4. As we will see in the remainder of this section, this procedure is not only suitable for the construction of a meaningful time delay operator (or more generally a DEFT operator, see section 3.5), but moreover, it is also qualified for applications of image transmission. Instead of a direct inversion of  $t_{\text{act}}$ , we rather modify Eq. (3.8) to

$$\vec{u}' = t_{\text{act}(b)}^{-1} t_{\text{ref}} \vec{u}, \quad (3.10)$$

by using the effective inverse  $t_{\text{act}(b)}^{-1}$  computed according to Eq. (2.57). In the absence of noise, we calculated  $\vec{u}'$  following (3.10) by keeping only singular values  $\sigma_n \geq 0.01 \sigma_{\text{max}}$  and the corresponding singular vectors in the projection of  $t_{\text{act}}$ , resulting in 47 of 50 kept singular values. The corresponding intensity pattern is shown in Fig. 3.4(d): The reconstruction of the goal output pattern works comparably well as compared to the perfect reconstruction in (c), however, less energy needs to be injected. An analogous calculation for the noise-afflicted transmission matrix in (3.9) gives the pattern displayed in Fig. 3.4(f). Whereas the output image is completely destroyed for the direct inversion in (e), it is, although distorted, still clearly visible when using the projected inverse. Here, we kept only those singular values with  $\sigma_n \geq 0.03 \sigma_{\text{max}}$ , i.e., the 43 of 50 channels featuring a transmission well above the noise level.

Concludingly, we state the mathematically rather simple yet powerful algorithm given by Eq. (3.8) and its amendment in Eq. (3.10) that can be used to effectively hide one scattering system by mimicking another. The effective inversion by projection onto 'bright' transmission channels involved in (3.10) proves to be an appropriate approach in terms of energy reduction and noise stability. In how far this inverse might also constitute a meaningful refinement or supplement of or to existing and well-established techniques using a so-called *Tikhonov regularization* [11,81], respectively, is subject to future investigation.

### 3.3 A Universal Time as an Invariance Property of Wave Scattering

A fundamental insight in the theory of diffusive random walks is that the mean length of trajectories traversing a finite open system is independent of the details of the diffusion process. This so-called *mean-chord-length theorem* states instead, that the average trajectory length depends only on the system geometry, and is thus unaffected by the value of the (scattering) mean free path [82], where the latter path describes the propagation distance after which a collision with potential scattering objects takes place on average. Here we show that this result is rooted on a much deeper level than that of a random walk, which allows us to extend the reach of this universal invariance property beyond the diffusion approximation. Specifically, we demonstrate that an equivalent invariance relation also holds for the scattering of waves in ballistic, chaotic, as well as in Anderson localized systems. Our work unifies a number of specific observations made in quite diverse fields of science ranging from the movement of ants to nuclear scattering theory. We obtained the results presented in this section in the framework of a collaboration with Romain Pierrat and Rémi Carminati from the ESPCI in Paris, and Sylvain Gigan from the Laboratoire Kastler Brossel in Paris, see our joint publication [61]<sup>1</sup>.

In the biological sciences it has been known for quite some time now, that the movement of certain insects (like ants) on a planar surface can be modeled as a diffusive random walk with a given constant speed  $v$  [83–85]. Using this connection, Blanco et al. [82] proved that the time that these insects spend on average inside a given domain  $\Omega$  of area  $A$  and with an external boundary  $C$  is independent of the parameters entering the random walk such as, e.g., the transport mean free path  $\ell^*$ . This transport length  $\ell^*$  is defined as the length over which the initial propagation direction of an ant (or a photon) is entirely randomized, and it strongly depends on the aforementioned scattering mean free path  $\ell$ . Specifically, the average time  $\langle\tau\rangle$  between the moments when an insect enters the domain and when it first exits it again, is given by the simple relation involving only geometrical parameters

$$\langle\tau\rangle = \frac{\pi A}{v C}. \quad (3.11)$$

One finds that the mean length  $\langle l \rangle$  of the corresponding random walk trajectories inside the domain is also constant,  $\langle l \rangle = \langle\tau\rangle v = \pi A/C$ . Similar relations also hold in three dimensions,  $\langle\tau\rangle = 4V/(\Sigma v)$  and  $\langle l \rangle = 4V/\Sigma$ ,

---

<sup>1</sup>Also the text of this section partially goes back to our paper [61]

where  $V$  and  $\Sigma$  are the volume and the external surface of the given domain, respectively. Extensions of this result exist for trajectories beginning inside the domain [86], or for the calculation of averaged residence times inside sub-domains [87]. As a generalization of the mean-chord-length theorem [32] for straight-line trajectories with an infinite mean free path  $\ell^*$ , this fundamental theorem has numerous applications, e.g., in the context of food foraging [88] and for the reaction rates in chemistry [89].

The surprising element of this result can be well appreciated when applied to the physical sciences and, in particular, to the transport of light or of other types of waves in scattering media. In that context, it is well-known that practically all of the relevant observable quantities depend on  $\ell^*$ : In the diffusive regime, the total transmission of a slab of thickness  $L$  scales with  $\ell^*/L$  through Ohm's law, and the characteristic delay time scales with the so-called Thouless time  $L^2/(v\ell^*)$  [90]. When considering coherent wave effects,  $\ell^*$  also determines the width of the coherent backscattering cone in weak localization [91, 92], and drives the phase-transition from diffusive to Anderson localization [93]. An invariant quantity that does not depend on  $\ell^*$  would thus be highly surprising to the community involved in wave scattering through disordered media. Since, in addition, coherent effects like weak or strong (Anderson) localization clearly fall outside the scope of a diffusive random walk model, one may also expect that an invariance property simply does not exist when wave interference comes into play.

As we will demonstrate here explicitly, this expectation is clearly too pessimistic. Instead, we find that an invariant time and length scale can also be defined for waves, even when they scatter non-diffusively as in the ballistic or in the Anderson localization regime. The keystone in understanding why the average wave time delay constitutes such an invariance property irrespective of the specific transport path  $\ell^*$  of the system under study is its connection to the density of states, which we discussed in section 2.3 of the preceding chapter. As it will turn out, the density of states is the central quantity that stays invariant on a level far beyond the scope of a diffusion approximation.

In the strongly scattering regime, wave interference can lead to a complete halt of wave diffusion in terms of Anderson localization. The question that naturally arises is whether localization will lead to a deviation from the prediction in Eq. (3.11) stemming from the mean-chord-length theorem or not. One could expect such a deviation, e.g., on the grounds that localization prevents scattering states to explore the entire scattering volume  $V$  of the system. Correspondingly, the volume  $V$  and the surface  $\Sigma$  might then have to be rescaled with the localization length  $l_{\text{loc}}$ .

To explore this question in detail, we performed numerical simulations

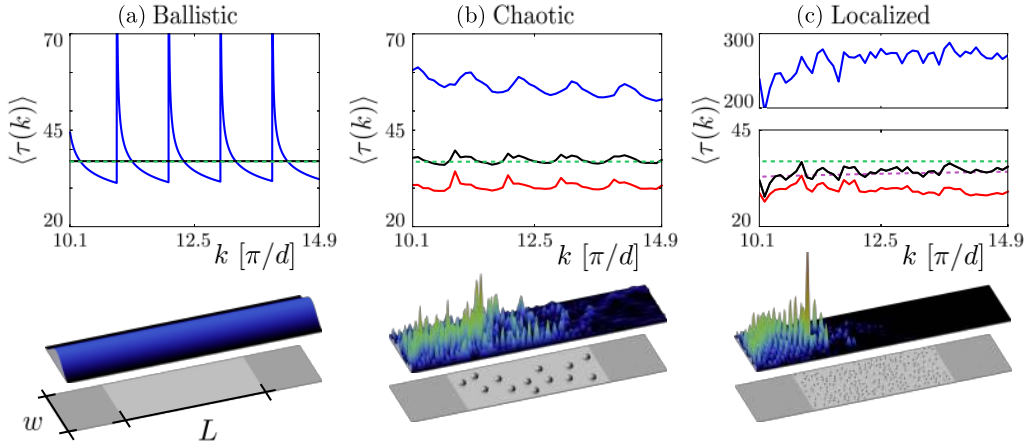


**Figure 3.5:** Total average delay time  $\langle \tau(k) \rangle$  (black line), transmission delay time (blue line), and reflection delay time (red line) for (a) ballistic scattering through a clean waveguide, (b) chaotic scattering through a disordered waveguide with 13 circular obstacles of radius  $r = 0.015 w$ , and (c) Anderson localized transport through a disordered waveguide with 211 obstacles of  $r = 0.060 w$ . All three waveguides have the same width  $d$  and the same effective scattering area  $A = 2.35 w^2$ . For (a), the transmission is perfect, thus the reflection times are strictly zero. The average for the total time delay (black line) is taken here over the entire wavenumber interval shown, and coincides with the estimate of Blanco et al. (green dashed line). For the disordered systems in (b),(c), the averages were taken over (b) 250 and (c) 2500 different random configurations, respectively. For the chaotic scattering case (b), the average delay time agrees well with the random walk prediction (dashed green line), for the case localized transport in (c), we found a systematic deviation. Very good agreement, however, is found with the estimate for the average scattering time according to the corrected Weyl estimate, Eq. (3.17) (purple dashed line). In the lower panels, the intensity of wave functions injected in the lowest-order mode is shown for a specific configuration of scatterers (see grey spheres) embedded in the scattering area (light grey domain in the middle). The flux is incoming from the left and can be transmitted (to the right) or reflected (to the left) through the perfect waveguides attached on both sides (see dark grey areas).

on a two-dimensional, rectangular scattering region of length  $L$  featuring disorder, that is again attached to perfect, semi-infinite waveguides of the same width  $w$  on the left and right (see illustrations in the lower panels of Fig. 3.5). Accordingly, the correct number of scattering channels  $N(\omega)$  is given by the total number of flux-carrying modes in both waveguides.

Unlike in the previous sections, the effective disorder potential is now not correlated and smooth, but rather consists of a discrete number of impenetrable and non-overlapping circular scatterers. The refractive index between individual scatterers is assumed constant,  $n(\vec{x}) = 1$ . In Fig. 3.5 we display our numerical results for different degrees of disorder: In subfigure (a), we show the results obtained for an empty scattering region, corresponding to the ballistic transport regime. In (b), the case with altogether 13 scatterers is shown, for which already a strong reduction of transmission is observed. Finally, in subfigure (c), we increased the degree of disorder even more by placing altogether 211 scatterers, such as to enter the regime of Anderson localization. In order to prove our assertions corresponding to the respective scattering regimes for the systems in (b) and (c), we explicitly investigated the distribution  $P(\zeta)$  in both cases in appendix B.1, where the symbol  $\zeta$  denotes the transmission eigenvalues, i.e., the spectrum of the matrix  $t^\dagger t$ . For (b),  $P(\zeta)$  follows very well the predictions of random matrix theory for the regime of chaotic scattering, whereas for (c), the distribution of transmission eigenvalues agrees very well with the predictions for the case when Anderson localization suppresses all but a single transmission eigenchannel (see also [94, 95]). To make all three cases easily comparable with each other, the different geometries all have the same scattering area  $A$ , which, for ballistic scattering is the entire rectangular region between the leads, whereas for the other two cases the area occupied by the impenetrable scatterers is not part of  $A$ .

Based on the above identification of the different transport regimes that our model system can be in, we investigate now the corresponding results for the average time  $\langle \tau \rangle$  which we get for each of these limits (see panels in Fig. 3.5). In the ballistic limit (see panel (a)), we see that the average time, plotted as a function of the incoming wavenumber  $k$ , shows pronounced periodic enhancements around the random walk prediction by Blanco et al. in Eq. (3.11). The peaks of these fluctuations can be identified with those positions in  $k = k_n = n\pi/w$ , where a new transverse mode opens up in the waveguide. To understand why these mode openings cause an increase in the scattering dwell time, we resort to the fundamental connection between the average dwell time  $\langle \tau \rangle$  and the density of states  $\rho(k)$  given by Eq. (2.38), which reads

$$\rho(k) = \frac{c N(k)}{2\pi} \langle \tau(k) \rangle = \frac{c}{2\pi} \text{Tr}(Q), \quad (3.12)$$

in terms of the wavenumber  $k = \omega/c$ . Since, in the ballistic regime, each individual incoming mode corresponds to a one-dimensional scattering channel with, correspondingly, an associated square root singularity in  $\rho(k)$ ,

$\rho_n(k) = (L/2\pi) k/\sqrt{k^2 - k_n^2}$  for  $k > k_n$ , we can successfully explain the observed oscillations as coming from the successive openings of new waveguide modes. Evaluating the total density of states based on the sum of individual mode contributions,  $\rho(k) = \sum_n^N \rho_n(k)$ , and using the above connection to the average time yields identical results to those shown in Fig. 3.5(a). This demonstration also allows us to show that the time, averaged over an interval of  $k$  that is larger than the distance between successive mode openings, converges exactly to the prediction by Blanco et al.. Quite remarkably, we find in this sense that the estimate from the mean-chord-length theorem and, correspondingly, the random walk prediction also holds, on average, for ballistic wave scattering in a system without any disorder.

Moving next to the disordered system in Fig. 3.5(b), we see that the presence of the disorder strongly reduces the above mode-induced fluctuations, leaving the frequency-average value of the scattering time unchanged. To explain this result, the density of states clearly needs to be estimated differently here than in the ballistic case of uncoupled waveguide modes. Also, since the disorder leads to system and frequency-specific fluctuations in  $\rho(k)$ , we are looking here for an estimate for the ensemble and frequency averaged density. To obtain this quantity, we invoke a result first put forward by Weyl in 1911 [96], who estimated that the average density of states in the asymptotic limit of  $\omega, k \rightarrow \infty$  satisfies the following universal law,  $\rho(\omega) = A\omega/(2\pi c^2)$ , now called the Weyl law [97]. Putting this estimate into the formula relating the average time with the average density of states Eqs. (2.38) and (3.12), we obtain

$$\langle \tau(\omega) \rangle = \frac{2\pi}{N(\omega)} \rho(\omega) = \frac{A\omega}{c^2 N(\omega)}. \quad (3.13)$$

The  $\omega$ -dependent number of incoming channels is given as an integer-valued step-function,  $N(\omega) = 2\omega w/(c\pi)$ . When smoothing over the steps in this function, i.e,  $N(\omega) \approx 2\omega w/(c\pi) - 0.5$ , we arrive at the result

$$\langle \tau(\omega) \rangle = \frac{2\pi}{N(\omega)} \rho(\omega) \approx \frac{\pi A}{c} \frac{A}{2d} = \frac{\pi A}{c C}. \quad (3.14)$$

This relation, which is very accurately satisfied by our numerical results, thus confirms the validity of the diffusive random walk prediction by Blanco et al. also for disordered wave scattering. Considering the expressions for the average reflection and transmission delay times we introduced in section 2.3, we find that these times do strongly depend on  $\ell^*$ . We thus observe that in a system like the considered one, the respective times associated with transmission and reflection need to fully counter-balance each other (see Fig. 3.5).

In the remainder of this section, we will show that this invariance of the average scattering time also persists in the strongly scattering limit, when Anderson localization sets in. Our numerical results shown for this case in Fig. 3.5(c), however, display a small but apparently systematic frequency dependence of the average time  $\langle\tau(\omega)\rangle$ , which increasingly deviates from the value in Eq. (3.14) for decreasing frequencies  $\omega$ . Since the numerical calculations are very challenging and the frequency derivative appearing in the construction of the time delay operator  $Q$  in Eq. (2.1) can reach very large values for highly localized scattering states, we first tested the accuracy of our simulations by evaluating  $\langle\tau(\omega)\rangle$  also through explicit dwell time calculations. Following Eq. (2.61), the expression for the partial dwell times in case of the Helmholtz Eq. (2.2) are given by  $\tau_{d,m} = U_{\Omega,m}/S_{\partial\Omega,m}^{\text{in}}$ , where the index  $m$  refers to the  $m$ -th scattering channel. According to Eq. (2.68), the average delay time is then given by

$$\langle\tau(\omega)\rangle = \frac{1}{N(\omega)} \sum_m^N \tau_{d,m}(\omega). \quad (3.15)$$

The results we obtained in this way (not shown) are practically indistinguishable from those shown in Fig. 3.5(c). To explain this robust deviation from the result in Eq. (3.14), we thus have a more careful look on the Weyl estimate which, in addition to the leading order term which we used above, also features a next-order correction proposed by Weyl [97, 98],

$$\rho(\omega) = \frac{1}{2\pi c} \left( A \frac{\omega}{c} + \frac{C - B}{2} \right). \quad (3.16)$$

This correction involves not only the scattering area  $A$ , but also the internal boundary of the scattering region  $B$  which is notably different from the external boundary  $C$  through which waves can scatter in and out. The internal boundary  $B$  in case of our waveguide system under study is given by  $B = 2L + B_o$ , where  $B_o$  is given by the total circumference of the scatterers. The open (constant-flux) boundary conditions along the external boundary  $C$  were approximated with Neumann boundary conditions, which contribute to the total density of states with the opposite sign as the Dirichlet boundary conditions on the surface of the waveguide and of the scatterers. In systems with a small boundary-to-area ratio this next-order correction of the Weyl law is negligible. Since, however, the number of scatterers which we have placed inside the system (from 0 in the ballistic case, to 13 in the chaotic case, to 211 in the localized case) increases this ratio, the additional boundary term in the Weyl law becomes important

here. To check this explicitly, we re-evaluate the expression for the average dwell time  $\langle\tau(\omega)\rangle$  from above when adding this correction, leading us to

$$\langle\tau(\omega)\rangle = \frac{1}{cN(\omega)} \left( A \frac{\omega}{c} + \frac{C - B}{2} \right). \quad (3.17)$$

A comparison of this analytical formula with the numerical results, see Fig. 3.5(c), yields excellent agreement and indicates that the observed deviation from the prediction by Blanco et al. stems from the comparatively large boundary of the many small scatterers which we placed inside the scattering region. We emphasize at this point that this correction to the Blanco estimate only contains the boundary values  $B$  and  $C$  as additional input, and remains entirely independent of any quantities that characterize the scattering process itself, like  $\ell^*$  or the localization length  $l_{\text{loc}}$ . This insight is of considerable importance, since it means that Eq. (3.17) defines a new invariant quantity that is independent of the scattering regime we are in, and thus accurately matches our numerical results for the average time in the ballistic, chaotic and localized limit. This invariant quantity for waves deviates from the prediction by Blanco et al. [82] only through an additional term originating in the fact that waves feel the boundary of a scattering region already when being close to it on a scale comparable with the wave length.

Summarizing our findings discussed in this section, we have derived a universal invariance property for wave transport through disordered media, namely the averaged path length or averaged time spent by a wave in an open finite medium. Due to the degree of universality of this averaged delay time, our results thus extend the implications of the mean-chord-length theorem<sup>2</sup> far beyond applications of random-walk theory. In the context of wave transport through complex media, most spatial or temporal observables scale with the transport mean free path  $\ell^*$ , so the invariance property we derived here is very counterintuitive. Particularly intriguing in our eyes is the possibility to get access, through Eq. (3.17), to the internal surface  $B_o$  of scatterers embedded in a scattering medium through a time-resolved transport experiment. The specific implications of the invariant average time delay on the design of structures to enhance light harvesting for solar cells will be briefly discussed in the following subsection.

---

<sup>2</sup>Note, however, that for dispersion relations different from the linear relation  $\omega(k) = kc$  in optics, e.g.,  $\omega(k) \propto k^2$  for the Schrödinger equation, the invariant quantity is the path length only.

## The Invariant Average Delay Time and the Yablonovitch Limit

In the theory of solar cells, a fundamental limit for the average intensity enhancement within a cell was already derived in 1982 by Eli Yablonovitch [33] - a result now known as the *Yablonovitch limit*, that is still subject to active research [99–101]. Briefly summarized, this law states, based on density-of-states arguments, that the mean intensity of light stored inside a solar cell, scales with the refractive index as  $n^2$  in a three-dimensional slab, where the latter is assumed to be homogeneous. The major presupposition for the Yablonovitch limit to apply is ergodicity, i.e., that the light waves must be able to explore the whole of the classical (ray, trajectory) phase space. However, no further assumptions on the specific geometrical shape of the light-harvesting device were made. The universal applicability of the Yablonovitch law irrespective of the cell's type of construction already indicates a deep connection to the invariant average delay time introduced in this section. The results of this subsection were achieved in collaboration with Jakob Melchard in the framework of his bachelor thesis that I co-advised [102].

From a mathematical viewpoint, the sought connection between the Yablonovitch limit and the invariant time can already be found in the density of states of the investigated system. For that reason, we will start our derivation from the density of states before we motivate our results more physically. As already mentioned, the intensity enhancement scales quadratically with the index of refraction in three spatial dimensions. In order to compare our numerical results in this section with the Yablonovitch law, however, we will restrict ourselves to two dimensions. We start by computing the density of states for the Helmholtz equation (2.2) for a square region of constant refractive index  $n$  and area  $A$ , which yields [102]

$$\rho(\omega) = \frac{A}{2\pi} \frac{n^2}{c^2} \omega. \quad (3.18)$$

Once again exploiting the Weyl law [96], we can apply Eq. (3.19) to any kind of system featuring the same area  $A$ . Using  $\langle \tau \rangle = 2\pi\rho/N$ , we thus find for the  $n$ -dependent average time the general expression

$$\langle \tau(n) \rangle = \frac{A}{N(\omega)} \frac{n^2}{c^2} \omega. \quad (3.19)$$

Using the link between the Wigner-Smith time delay operator and the dwell time operator in Eq. (2.68), we can write for the ratio of the mean delay

times

$$\frac{\langle \tau(n) \rangle}{\langle \tau(1) \rangle} = \frac{\sum_m \int_{\Omega} dA \psi_m^*(\vec{x}) n^2 \psi_m(\vec{x})}{\sum_m \int_{\Omega} dA \psi_m^*(\vec{x}) \psi_m(\vec{x})} = n^2, \quad (3.20)$$

with  $\psi(\vec{x})$  denoting again the wavefunction for the  $m$ -th mode injected. Since, in contrast to the derivations in section 2.5, we restrict ourselves to two-dimensional geometries, the integration over the stored electromagnetic energy density is now an integration over an area of size  $A$ , rather than an integration over a volume  $V$ . As discussed in the appendix A.2, the intensity for every scattering channel at each point inside the scattering region can be written as

$$I_m(\vec{x}) = v \epsilon_m(\vec{x}) = \frac{c}{n} \left[ \frac{1}{2} \epsilon_0 \psi_m^*(\vec{x}) n^2 \psi_m(\vec{x}) \right], \quad (3.21)$$

where we used  $v = c/n$ . A summation over all open modes and an integration over the entire scattering region  $\Omega$  then gives the total stored intensity,

$$I = \int_{\Omega} dA \sum_m I_m(\vec{x}). \quad (3.22)$$

Since the integration and summation in Eq. (3.22) commute, a comparison to the ratio in Eq. (3.20) gives for the intensity enhancement factor  $\mu$  in two dimensions

$$\mu(n) := \frac{I(n)}{I(1)} = \frac{c/n \sum_m \int_{\Omega} dA \psi_m^*(\vec{x}) n^2 \psi_m(\vec{x})}{c \sum_m \int_{\Omega} dA \psi_m^*(\vec{x}) \psi_m(\vec{x})} = n. \quad (3.23)$$

From this equation it is now easy to write for the fundamental connection between the intensity enhancement factor and the average delay time in Eq. (3.20)

$$\mu(n) = \frac{I(n)}{I(1)} = \frac{v(n) \langle \tau(n) \rangle}{v(1) \langle \tau(1) \rangle}. \quad (3.24)$$

The physical content of Eq. (3.24) is, that intensity enhancement and dwell time prolongation are equivalent. The longer the wave dwells inside the system (or equivalently, the longer its effective propagation path inside the system is), the more intensity is accumulated. The delay time is exactly the duration of time in which the light is able to deliver its energy to the solar cell, accordingly, longer dwell times result in a more efficient way of exploiting solar energy. However, both the average delay time  $\langle \tau \rangle$  and the intensity enhancement factor  $\mu$  are intrinsically limited by the system's area, but independent of its exact shape due to the universal Weyl law for the density of states.

We also substantiated our theoretical findings with numerical simulations for  $\langle\tau\rangle$  and  $\mu$  of the system depicted in Fig. 3.6(b). A square scattering region  $\Omega$  of length  $L$  and area  $A$  is connected to one semi-infinite lead of the same width  $w$ . The boundary opposite to the attached waveguide is roughened in order to introduce mode mixing and, therefore, to satisfy the necessary ergodicity condition. We assumed a homogeneous index of refraction inside  $\Omega$ , which we varied from  $n = 1$  up to  $n = 5$ , whereas the lead features an index of  $n = 1$ . The total wavenumber of the incident waves was chosen to equal  $k = 15.51\pi/w$ , so there are  $N = 15$  modes open. Please note that for our perfectly reflecting geometry, this is also the total number of incident modes, whereas for the respective geometry with a second lead attached thus also allowing for transmission, the total number would be  $N = 30$ . When comparing to the respective transmission geometry, the ratio  $\mu$  in Eq. (3.23) is multiplied by a factor of 2, as a result. At each calculated value of  $n$ , we computed the average time  $\langle\tau\rangle$  and the factor  $\mu$  and averaged both quantities over 20 different random realizations of the surface roughness. The exact expression for the function  $h(y)$  characterizing this roughness can be found in appendix B.1. The results for the mean time and enhancement factor are plotted in Fig. 3.6(b), where we clearly see that the average delay time follows very well the predicted value of  $\langle\tau\rangle = \pi A/(vC)$  in Eq. (3.11), and that  $\langle\mu\rangle$  follows the prediction of  $\langle\mu\rangle = 2n$ .

Summarizing our findings in this subsection, we could successfully derive the link between the fundamental Yablonovitch limit for solar cells and our invariance property, the averaged delay time, which essentially proves that both statements are just two sides of the same medal. In this way, our findings might also indirectly contribute to the design of future generations of solar cells: Naively, one may think that constructing some kind of 'maze' for the sunlight to raise the photon dwell time might be a suitable measure, however, our results show, that the average efficiency cannot be raised by purely geometrical means.

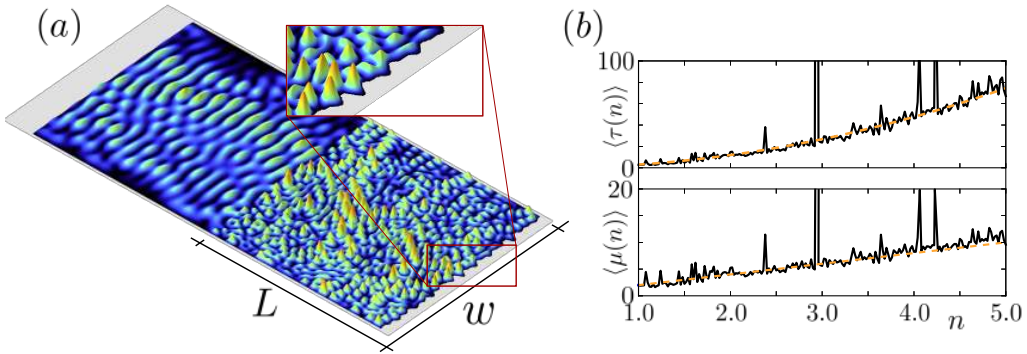


**Figure 3.6:** (a) Sketch of the system and intensity plot for the wave corresponding to injection in the first waveguide mode. The lead is assumed to be clean, the refractive index inside the scattering region was chosen as  $n = 2$  for this plot. The wall opposite to the lead is roughened to ensure ergodicity, the smaller inset shows a zoom on this boundary. (b) Plots for the mean delay time  $\langle \tau \rangle$  and the averaged intensity enhancement factor  $\langle \mu \rangle$  for 201 different values of  $n \in [1, 5]$ , averaged over 20 different realizations of the boundary roughness (black curves). For reasons of simplicity we assumed  $L = w = 1 \rightarrow A = 1$  as well as switching to atomic units, thus setting  $c \equiv 1$  for the speed of light. We clearly see, that  $\langle \tau \rangle$  and  $\langle \mu \rangle$  follow the analytical predictions  $\langle \tau \rangle = \pi n^2$  and  $\langle \mu \rangle = 2n$  (orange dashed lines), respectively.

### 3.4 Orthogonal Super Principal Modes

As mentioned in section 2.4 of the previous chapter, the eigenstates of the general time delay operator  $q$  in Eq. (2.45), i.e. the principal modes (PMs), constitute a very favorable basis of input profiles. Since their output speckle patterns remain spatially stable over a considerable bandwidth if the frequency of the incident light is altered [27, 28], the PMs are much preferable when compared to input configurations that were not tailored in a proper fashion. Such a transmission behavior is specifically desirable for the transmission of pulses with spectral shapes fitting into this stability bandwidth, because then the spatial and temporal profiles of a pulse decouple. Yet these states suffer from the drawback that their output stability bandwidths may greatly vary between different PMs, on the one hand, and that even the bandwidth for the best PM may still not be adequate for an efficient pulse transmission, on the other hand.

In spite of the first experimental demonstrations of the PMs, having succeeded only very recently for the regimes of weak [29] and strong mode mixing [103] in fiber optics, we report here on the demonstration of a novel set of input configurations - both theoretical and experimental - whose corresponding stability frequency bandwidths even exceed those of the PMs. In order to overcome the bottleneck in stability constituted by the PMs, our construction algorithm relies on the experimentally measured polychromatic transmission matrix, rather than the scattering amplitudes at a single wavelength only. We directly apply our findings experimentally to a multi-mode fiber (MMF) in the realistic and challenging regime of strong mode mixing, and further demonstrate that our general concepts can also be used to optimize other transport properties than the spectral output stability. Unlike the PMs, these super principal modes can generally be chosen strictly orthogonal, for that reason we termed this special set of states *orthogonal super principal modes* (OSPMs). One of the very desirable properties of the OSPMs is their reduced crosstalk, that occurs when parts of the signal scatter into other transmission channels than the intended ones.

In collaboration with Wen Xiong, Yaron Bromberg, Brandon Redding, and Hui Cao from Yale University, we implemented our theoretical findings discussed in the following for the specific fiber system sketched in Fig. 3.7(a), where we measured the transmission matrix  $t(\omega)$  for a one-meter-long step-index MMF at different frequencies  $\omega$ . The fiber features a core diameter of  $50\mu\text{m}$ , a numerical aperture of 0.22, and supports about 120 linearly polarized modes at  $\lambda_0 = 1550\text{nm}$  for one polarization. The used digital holographic setup is able to record amplitude as well as phase by applying a Hilbert filter to the farfield of the light leaving the fiber output facet using

the interference with a reference plane wave. We use a single spatial light modulator to spatially control both amplitude and phase of the wavefront coupled into the fiber [104].

In order to understand why a large output stability bandwidth is favorable for telecommunication purposes, we need to consider the two main mechanisms in linear wave transmission that cause a distortion of an initial wave packet sent into the system (see also section 2.4): Firstly, there are deformations due to the so-called *chromatic dispersion*, i.e., wavelength-dependent global amplitudes and global phases. In the special context of fiber communication, however, these effects can often be compensated for [105,106]. A suppression of the second mechanism, the system-inherent *modal dispersion* is more challenging though. The modal dispersion stems from the different delay times of different modes in an MMF, and causes the output speckle pattern to change its spatial shape during the pulse duration.

The principal modes do not suffer from modal dispersion to first order, which follows directly from the construction of the time delay operator  $q$  in Eq. (2.45) (see section 2.4). In case of compensated effects of chromatic dispersion, the time delay eigenstates thus allow a perfect, stable transmission of pulsed signals within the spectral vicinity of the frequency  $\omega_0$  at which the time delay operator is calculated. A suitable measure for the modal dispersion, i.e., the deviation of the output vector  $\vec{v}(\omega) = t(\omega) \vec{u}$  from its respective direction at  $\omega_0$  is the field autocorrelation function

$$C(\omega, \omega_0) := |\hat{v}^\dagger(\omega) \cdot \hat{v}(\omega_0)| \in [0, 1], \quad (3.25)$$

where  $\hat{v}(\omega) = \vec{v}(\omega)/|\vec{v}(\omega)|$  is the normalized output vector. We define the correlation bandwidth of a given input state as the spectral region where the center peak of the correlation function does not drop below 0.90. Fig. 3.7(b) shows the measured correlation function for the PM featuring the largest spectral bandwidth in comparison to the average correlation function of 1000 random input configurations. Please note, that  $C(\omega, \omega_0)$  has a global maximum of 1.0 at the reference frequency by construction for arbitrary inputs, however, the correlation bandwidth of the shown PM clearly exceeds that of random inputs. Figs. 3.8(a) and (b) show the output intensity images for the best PM and one specific random input configuration, respectively.

As a first attempt in order to find input configurations that even outplay the PMs in their advantageous characteristics, we look for a simple, linear operator that would yield such 'super PMs' among its eigenstates. For that purpose, we construct a set of operators very similar to the time delay

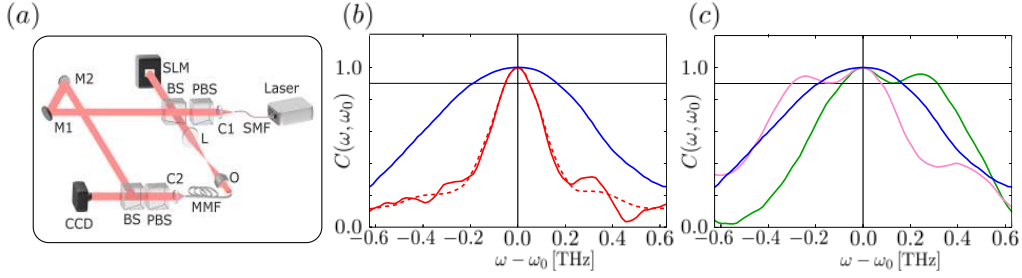


**Figure 3.7:** (a) Schematic of the experimental setup. A laser beam is split into two paths: the signal which is modulated by a spatial light modulator and imaged to the fiber facet of the MMF by a 4-f system composed of a lens and a micro objective, and the reference arm matching the signal arm's pathlength using a pair of mirrors, respectively. The two arms are eventually recombined in front of the CCD camera. (b) Measured autocorrelation function  $C(\omega, \omega_0)$  for the output signals of the most stable PM with a bandwidth of 0.344 THz (blue), one specific random input (red) with a bandwidth of 0.110 THz, and the average correlation for 1000 random inputs (red dashed, 0.110 THz bandwidth). The vertical and the horizontal black lines indicate the reference frequency  $\omega_0$ , and  $C(\omega, \omega_0) = 0.90$ . The pink/green lines in (c) show the broadest correlations for  $\rho(\mp\Delta\omega)$  eigenfunctions with  $\Delta\omega = 0.26$  THz, along with the corresponding curve for the best PM (blue). For  $\Delta\omega > 0.26$  THz, the dips between the two respective peaks in the correlations drop below our threshold of  $C(\omega, \omega_0) = 0.90$ . The respective output intensity patterns for the best PM and the chosen random configuration at  $\omega_0$ , respectively, are displayed in Fig. 3.8(b), (c). The reason why the peaks do not perfectly reach 1.0 at  $\mp\Delta\omega$  is that the operators  $\rho(\mp\Delta\omega)$  are constructed using the projected transmission matrix (see section 2.4).

matrix  $q$ ,

$$\rho(\omega, \omega_0) := -i t^{-1}(\omega_0) \frac{t(\omega) - t(\omega_0)}{\omega - \omega_0}, \quad (3.26)$$

where the symbol  $\rho(\omega, \omega_0)$  used in this section to denote these operators is not to be confused with the density of states. The time delay operator can then be viewed as the limiting operator  $\lim_{\Delta\omega \rightarrow 0} \rho(\omega_0 \pm \Delta\omega, \omega_0) = q(\omega_0)$ . The eigenstates of the new matrices  $\rho(\omega, \omega_0)$  generally feature output vectors that are aligned to each other at two generally distinct frequencies  $\omega_0$  and  $\omega$  (see appendix B.2). This results in corresponding output correlation functions  $C(\omega, \omega_0)$  which do not only peak at  $\omega_0$ , but also at  $\omega \neq \omega_0$  as

shown in Fig. 3.7(c). If we now gradually increase  $|\omega - \omega_0|$ , these correlation peaks move further apart, however, the output state tends to decorrelate in between the peaks resulting in a dip. Thus, the maximum bandwidth achievable in this way is limited by the value of  $|\omega - \omega_0|$  where the dip does not drop below 0.90, our decorrelation limit for the bandwidth. As we find, the maximally stable  $\rho(\omega, \omega_0)$ -eigenstates feature a much broader bandwidth than a random input configuration, yet the center peaks are still narrower than the peak for the best PM (Fig. 3.7(c)).

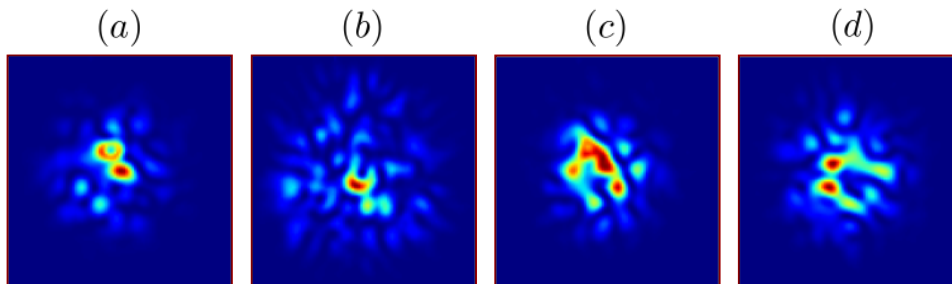


**Figure 3.8:** Measured output intensity speckle patterns recorded at the reference frequency  $\omega = \omega_0 = 1215 \text{ THz} \equiv 1550 \text{ nm} = \lambda_0$  for (a) the best PM, (b) the specific random input discussed in Fig. 3.7(b), (c) the best OSPM generated based on the cost function (3.27), and (d) the best OSPM generated based on the cost function (3.30).

An ideal input state  $\hat{u}$  featuring a perfectly flat correlation function of  $C(\omega, \omega_0) \equiv 1.0$  could be found, if  $\hat{u}$  was a simultaneous eigenstate of *all* operators  $\rho(\omega, \omega_0)$  in the spectral region of interest. Unfortunately, since the commutator  $[\rho(\omega_1, \omega_0), \rho(\omega_2, \omega_0)]$  with  $\omega_1 \neq \omega_2$  is generically non-singular, such a state does not exist in general. Constructing an approximate rather than a perfect mutual eigenvector of many different operators  $\rho(\omega, \omega_0)$  would imply the optimization of some non-linear cost function for the corresponding vector coefficients  $\hat{u}$ . A possibly very time-consuming minimization of a cost function featuring a rather complicated structure, however, might exceed the time scale on which the fiber system is sufficiently stable. If the transmission matrix  $t(\omega)$  is known in a whole  $\omega$ -interval though, one can

also directly optimize a much simpler cost function like

$$\begin{aligned} \mathcal{T}(\hat{u}) &:= \int d\omega (1 - C(\omega, \omega_0)^2) W(\omega) \\ &= \int d\omega \left( 1 - \frac{|\vec{v}^\dagger(\omega) \cdot \vec{v}(\omega_0)|^2}{|\vec{v}(\omega)|^2 |\vec{v}(\omega_0)|^2} \right) W(\omega), \end{aligned} \quad (3.27)$$

which constitutes the core of our algorithm that ultimately leads to OSPMs. For perfectly aligned output vectors  $\vec{v}(\omega)$  and  $\vec{v}(\omega_0)$ , i.e., for a perfectly stable output speckle pattern,  $\mathcal{T}$  vanishes, since  $C(\omega, \omega_0) \equiv 1$  then. Minimizing Eq. (3.27) thus translates into broadening the spectral correlation function  $C(\omega, \omega_0)$ . The (real, scalar) value of  $\mathcal{T}(\hat{u})$  depends on the input configuration  $\hat{u} = t^{-1}(\omega) \vec{v}(\omega)$  that is optimized for. Since we are only interested in maximizing the width of the center peak in the correlation function rather than raising its values at all possible frequencies  $\omega$ , a suitable weighting function  $W(\omega)$  is mandatory. We specifically chose  $W(\omega)$  to be a step-like, but continuous function centered around  $\omega_0$  as displayed in Fig. 3.9(a) for which we achieved the largest OSPM correlation bandwidths. The exact expression for  $W(\omega)$  is given in appendix B.2. An efficient minimization of  $\mathcal{T}$  is possible just using a simple gradient-based scheme (see appendix B.2 for the algorithm and for the expression of the functional gradient  $\delta\mathcal{T}/\delta\hat{u}$ ). At this point we emphasize, that our optimization scheme is a purely numerical optimization based on the experimentally measured transmission matrices in contrast to an experimental feedback loop. A whole cascade of optimizations of Eq. (3.27) can be performed, where after each step, the cost function is minimized in the vector space orthogonal to each of the OSPMs obtained in the preceding steps. In this way, we arrive at a strictly orthogonal set of super PMs that we directly reinjected into our fiber setup - Fig. 3.9(a) shows the correlation functions of the measured output states. We were able to find 14 optimized input configurations that lead to correlations even broader than that of the best PM. Ibidem, we also show the correlation function for an optimized state, where we used the homogeneous weighting function  $\tilde{W}(\omega) \equiv 1.0$ . In that case, the irrelevant tails of the correlation function are increased rather than the width of the center peak.

Much of the orthogonality of the OSPM input profiles is, indeed, sustained in the transmission process through the fiber, therefore reducing crosstalk between different OSPMs. As a quantitative measure for their orthogonality, we introduce the matrix

$$O_{mn} := |\hat{v}_m^\dagger(\omega_0) \cdot \hat{v}_n(\omega_0)|, \quad (3.28)$$

whose elements are the overlaps of the output signals for the  $m$ -th and  $n$ -th OSPMs. For a perfectly orthonormal set we would have  $O_{mn} = \delta_{mn}$ , with  $\delta$  being the Kronecker delta. A plot of the  $O$ -matrix is shown in the smaller inset of Fig. 3.9(a), from which the high degree of preserved orthogonality can directly be seen.

The ratio of the bandwidths of the best PM and the average bandwidth of random inputs turns out to be 3.13 for the fiber system under study. However, the respective ratio of the best OSPM and the best PM describes again a distinct broadening of this bandwidth of a factor of 1.91. We also emphasize that this is the ratio of the best OSPM to the *best* PM, the average value for the bandwidths of the PMs evaluates to 0.229 THz in comparison to the best PM with a bandwidth of 0.344 THz. The output intensity pattern for the best OSPM is shown in Fig. 3.8(c). Please further note that the PMs being eigenstates of the generally non-Hermitian operator  $q$  are not orthonormal. Hence, the OSPMs constitute a significant improvement compared to the PMs, both in bandwidth and orthogonality that was previously unachieved.

In contrast to the time delay operator  $q$ , the functional  $\mathcal{T}$  involves the transmission matrix for a whole spectral interval rather than for a single wavelength. Making use of this additional information is one of our algorithm's key ingredients allowing for super PMs. In order to explain the mechanism causing such large OSPM bandwidths, we return to the previously defined linear,  $\omega$ -dependent  $\rho(\omega, \omega_0)$ -operators in Eq. (3.26). As briefly discussed above, a state with the property of being an eigenstate of all  $\rho$ -operators in the entire spectral region of interest would feature a perfectly flat correlation function. As we will see in what follows, the OSPMs are indeed closer to being such common eigenstates than random inputs or even the PMs are. For that purpose, we define a measure that quantifies how close an input state is to being a simultaneous eigenvector of all  $\rho(\omega, \omega_0)$ -operators,

$$B(\hat{u}) := \frac{1}{\bar{N}_{\text{rand}}} \int d\omega \frac{\langle |\rho(\omega, \omega_0) - \langle \rho(\omega, \omega_0) \rangle|^2 \rangle}{|\langle \rho(\omega, \omega_0) \rangle|^2} W(\omega). \quad (3.29)$$

The numerator of the integrand on the right-hand side of Eq. (3.29) is the variance, the denominator is the absolute square of the expectation value of  $\rho(\omega, \omega_0)$  for a given input state  $\hat{u}$  (see appendix B.2 for the exact mathematical expressions). The constant  $\bar{N}_{\text{rand}}$  normalizes the functional  $B$  such that the average over a large number ( $10^5$ ) of random inputs  $\bar{B}_{\text{rand}} = 1.0$ . If  $\hat{u}$  is a perfect common eigenstate to all  $\rho(\omega, \omega_0)$  where  $W(\omega) \neq 0$ , all variances and, therefore,  $B$  vanishes. The average for the 15 PMs featuring

the largest bandwidths evaluates to  $\bar{B}_{\text{PM}} = 2.9 \times 10^{-4}$  which is almost 4 orders of magnitude smaller than  $\bar{B}_{\text{rand}}$ . Most importantly here, the corresponding average for the 15 measured OSPMs is  $\bar{B}_{\text{OSPM}} = 1.2 \times 10^{-4}$  which is again a factor of 2.4 smaller than that of the PMs. We may thus draw the conclusion, that although the very best PMs are already close to being mutual eigenstates of all relevant operators  $\rho(\omega, \omega_0)$ , the OSPMs are superior in this respect - a fact, which explains, in turn, their even broader bandwidths.

Our algorithm based on cost functions relying on the polychromatic transmission matrix turns out to be very versatile. In cases where a compensation of the effects of chromatic dispersion is not feasible, a different cost function containing both distortion mechanisms of chromatic and modal dispersion at once can be minimized (see appendix B.2 for more details),

$$\mathcal{L}(\hat{u}) := \int dt \left( \frac{|\vec{v}(t)|^2}{N_v} - \frac{|\epsilon(t - t_0)|^2}{N_\epsilon} \right)^2. \quad (3.30)$$

The temporal signals  $\vec{v}(t)$  and  $\epsilon(t)$  are just the Fourier-transformed quantities of the spectral output signal and the (scalar) spectral input envelope as defined in Eq. (2.52), respectively. Again, the symbol  $t$  now denotes time for the remainder of this section and must not be confused with the transmission matrix  $t(\omega)$ . The normalization constants are given by  $N_v = \int dt |\vec{v}(t)|^2$ , and  $N_\epsilon = \int dt |\epsilon(t)|^2$ . An optimization of Eq. (3.30) leads to static input configurations  $\hat{u}$ , that can be used to generate time-dependent output packets that resemble the shape of the chosen input pulse  $\epsilon(t)$  as well as possible. In this way, we minimize both of the aforementioned effects of dispersion. The unknown shift parameter  $t_0$  in Eq. (3.30), which is essentially the time delay of the output pulse, can be viewed as just an additional, real parameter to be optimized for. Fig. 3.9(b) shows the output pulses for the 15 input vectors we minimized Eq. (3.30) for, that resemble the chosen sinc-like input pulse  $\epsilon(t)$  (the sinc pulse is especially suitable for telecommunication purposes [107]) more closely than the pulse resulting from the best PM. Fig. 3.8(d) displays the output speckle pattern of the best OSPM. Since with the cost function in Eq. (3.30), we optimized for both the chromatic and modal dispersion, many of the OSPMs moreover feature a broader correlation bandwidth than the best PM as can be seen from Fig. 3.9(c).

Concludingly we emphasize again, that the optimization scheme we presented in this section is not restricted to  $\mathcal{T}$  and  $\mathcal{L}$  in Eqs. (3.27), (3.30), in fact, literally *any* cost function that can be constructed using the information stored in the polychromatic transmission matrix may serve as a possible candidate for finding whole sets of optimal input states.

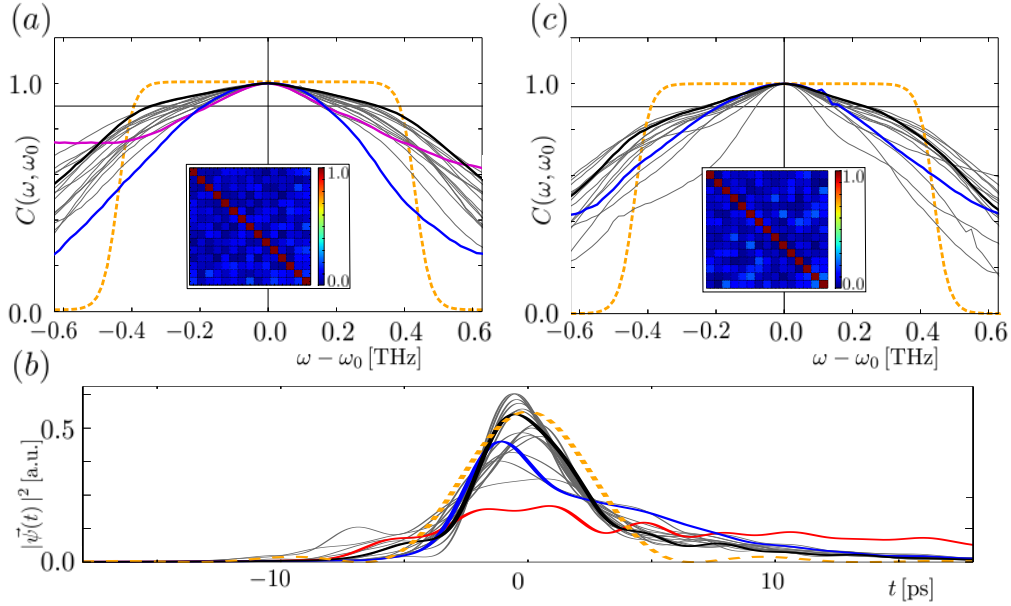


**Figure 3.9:** (a) Measured autocorrelations  $C(\omega, \omega_0)$  for the output signals of the best PM (blue), and 15 measured optimized states (grey). 14 of the 15 OSPMs feature a larger bandwidth than the best PM, the most stable one (black) features a bandwidth of 0.657 THz which is nearly two times larger than that of the best PM. The vertical and horizontal thin black lines indicate  $\omega_0$  and  $C(\omega, \omega_0) = 0.90$ , respectively. The weighting function  $W(\omega)$  used in the cost function optimized in order to get the OSPMs (Eq. (3.27)) is also shown (orange dashed). The magenta line is the correlation function for a state optimized using the homogeneous weighing function  $\bar{W}(\omega) \equiv 1.0$ . The smaller inset shows the overlap matrix elements  $O_{mn}$  (see main text). On average we find for the off-diagonal element the small value of  $\bar{O}_{\text{off}} = 0.077$ . (b) Temporal output pulses  $|\vec{\psi}(t)|^2$  for an input pulse  $|\epsilon(t)|^2$  (orange dashed) for the best PM (blue) and 15 OSPMs (grey) found by minimizing the functional in Eq. (3.30), as well as for a random input (red). The specific shape of the chosen  $\epsilon$  is just the Fourier-transform of the step-like weighting function we used before (see (a)). For 13 of the 15 OSPMs, the overlaps of the input and output signals are larger than for the best PM. The pulse of the best-matching OSPM is shown by the bold black line. (c) Many (8 of 15) of the OSPM input profiles leading to the pulses discussed in (b) do not only preserve the initial pulse shape better than the best PM, but also feature a larger correlation bandwidth (grey, black for best OSPM, blue for best PM). Analogously to (a), the inset shows the output signal overlaps  $O_{mn}$  for the 15 OSPMs, where we find  $\bar{O}_{\text{off}} = 0.080$ . The differences between the measured correlation curve for the best PM in (a) and the corresponding plot in (c) stem from two separate, independent measurements of the fiber transmission matrices.

### 3.5 DEFT: Focus and Omission in Disordered Media

As a specific example for the general DEFT operator class we introduced in section 2.6, we will now discuss the operators

$$D_x = -iS^\dagger \frac{dS}{dx}, \quad \text{and} \quad d_x = -it^{-1} \frac{dt}{dx}, \quad (3.31)$$

where we generally use the symbol  $x$  to denote any spatial direction here. If  $x$  means the spatial position of the entire scattering region along a given axis, the expectation value for an arbitrary input  $\vec{u}$  reads, according to Eq. (2.78),

$$\vec{u}^\dagger D_x \vec{u} = \vec{u}^\dagger k_x \vec{u} - \vec{v}^\dagger k_x \vec{v}, \quad (3.32)$$

where we used the input-output relation  $\vec{v} = S\vec{u}$ , further  $S^\dagger S = \mathbb{1}$ , and for the operator  $k_x$  we thus have  $\hat{k}_x = -i\partial_x$ . Eq. (3.32) thus measures the difference of the wave expectation values for  $k_x$  before and after the scattering process, i.e., exactly that shift in  $k_x$  the wave experiences during propagation. Although the former expectation values are taken for the flux rather than for the wave amplitudes (analogous to the Wigner Smith time delay operator  $Q$ ), for reasons of simplicity, we will call  $\hat{k}_x$  the 'momentum' operator for the direction  $x$ , and  $D_x$  the momentum shift operator, accordingly. One can also view the  $D_x$ -operator as a measure for the momentum transfer the system experiences due to the scattering event, rather than the shift in the  $k_x$ -expectation value for the scattered wave, however, these shifts differ only by a sign.

Before demonstrating a direct application of  $D_x$  in the last subsection of this chapter, we consider the case of a scattering system that mainly consists of distinct, discrete scattering objects, whose positions are characterized by the scalar variables  $\{x_n\}$ . The total increment of the scattering matrix,  $\Delta S$ , and thereby also its total derivative, can then be written in terms of the sums

$$\Delta S \approx \sum_n \frac{dS}{dx_n} \Delta x \quad \rightarrow \quad \frac{dS}{dx} = \sum_n \frac{dS}{dx_n}, \quad (3.33)$$

with the summation index including all parts of the system that affect scattering into the  $x$ -direction. Inserting the expression on the right-hand side of Eq. (3.33) into the definition of the the momentum shift operator, it follows that  $D_x$  can also be expressed in terms of a sum of operators,

$$D_x = \sum_n -iS^\dagger \frac{dS}{dx_n} := \sum_n D_x^{(n)} = k_x - S^\dagger k_x S, \quad (3.34)$$

where we also used Eq. (3.32) for the last equal sign. The meaning of the (Hermitian) partial shift operators  $D_x^{(n)}$  corresponding to the positions of the individual scatterers becomes clear from Eq. (3.34): The sum of all these operators is identical to the operator  $D_x$ , and thus measures the total  $k_x$ -shift as discussed above. Hence, each of the summands  $D_x^{(n)}$  measures the ultimate effect on the *total* shift in  $k_x$ , that can be attributed to the respective scatterer at position  $x_n$ . We emphasize, however, that the individual contribution to the total momentum shift stemming from the presence of the considered  $n$ -th scatterer has to be seen *in the complex interplay* of all other scatterers. Specifically, this also implies, that the expectation value  $\vec{u}^\dagger D_x^{(n)} \vec{u}$  must not be seen as corresponding to the change in  $k_x$  for the simple case where the  $n$ -th scatterer was the only one present in the system, or for the situation if this scatterer was removed from it. The underlying reason is, that generally, the complex multi-path interference pattern would drastically change due to such or similar interventions. Therefore, also the ultimate effect of each obstacle on the scattered wave would be altered decisively.

In most types of currently-existing experiments, it is easier to address only subparts of the scattering matrix, e.g., the transmission matrix. The construction of the generally non-Hermitian operator(s)

$$d_x = \sum_n -it^{-1} \frac{dt}{dx_n} := \sum_n d_x^{(n)}, \quad (3.35)$$

involving the transmission matrix  $t$  is thus often more suitable rather than constructing  $D_x$  in Eq. (3.34). The physical meaning of  $d_x$  is deciphered by Eq. (2.72), which states for our concrete choice of  $a = x$ , that a  $d_x$ -eigenstate will experience a well-defined shift in  $k_x$ , which is given by the derivative of the corresponding scattering phase with respect to  $x$ . In perfect analogy to the time delay operator  $q$  in Eq. (2.45), where the appropriate quantity is the frequency  $\omega$ , the output intensity patterns of  $d_x$ -eigenstates will generally not change their shape to first order, except being dimmed or brightened up, if now the position of the scattering region is varied along the  $x$ -axis. Due to the non-Hermiticity of  $d_x$  and the partial shift operators  $d_x^{(n)}$ , an interpretation of the respective eigen- and expectation values of the  $d_x^{(n)}$ -operators, however, cannot be made as easily as in the Hermitian case, unfortunately. What we do know about the eigenstates of the  $d_x^{(n)}$ -operators, in turn, is that the shapes of their output patterns are now not affected by a variation of the position of only the respective  $n$ -th scatterer, instead of the whole scattering area. This desirable property follows simply from Eq. (3.35), since the operators  $d_x^{(n)}$  'inherit' this remarkable feature due to their special construction analogous to  $d_x$ .

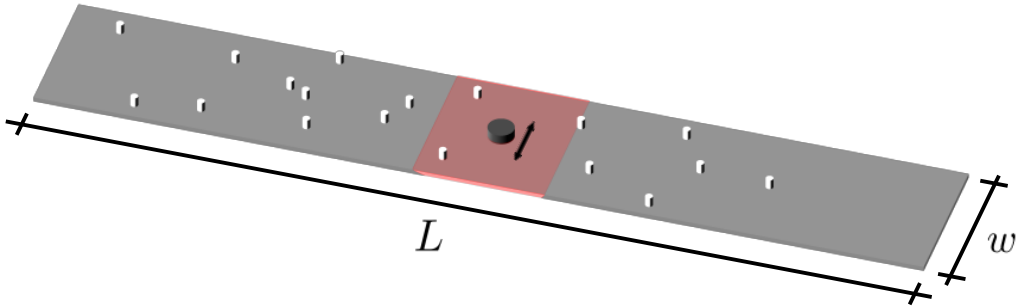


**Figure 3.10:** Sketch of the experimental setup. The scattering region is an aluminum resonator of width  $w = 10$  cm and length  $L = 60$  cm. The wavefront is injected from the left. 18 cylindric scatterers (white,  $n = 1.44$ , radius 2.550 mm) were randomly placed around a metallic scatterer of radius 8.825 mm (dark grey), which is movable in transverse direction. The center region around the metallic cylinder which is displayed in Figs. 3.11 and 3.12 is highlighted in red. The placement in this sketch matches the actual placement of obstacles in the experiment.

The latter observation leads us to the theoretical prediction, that, among states that achieve this independence of the  $n$ -th scatterer's actual position as a result of more subtle wave-interference effects, also  $d_x^{(n)}$ -eigenstates should exist that either strongly *focus* on the chosen object or completely *avoid* it. A strong focus, on the one hand, should lead to a shift in  $k_x$  highly influenced by the presence of the obstacle, which translates into a high  $d_x^{(n)}$ -eigenvalue  $\kappa_x^{(n)}$ . A complete omission, on the other hand, should result in a corresponding  $\kappa_x^{(n)}$  of zero, since the wave is then entirely unaffected by the scatterer.

In order to experimentally verify our predictions, we investigated the microwave setup displayed in Fig. 3.10 in collaboration with Julian Böhm and Ulrich Kuhl from the University of Nice, together with André Brandstötter who supported the experiment by numerical simulations as a part of his diploma thesis that I co-advised [108]. A microwave resonator containing 18 randomly placed scatterers made of teflon featuring a refractive index of  $n = 1.44$  and a radius of 2.550 mm, as well as one metallic scatterer of radius 8.825 mm playing the role of the movable particle, constitute the scattering region along with the resonator's boundary. The width of the resonator of  $w = 10$  cm allows for 10 propagating modes at our injection frequency of 15.5 GHz, where an array of 10 antennas generating the microwave front, allows us to fully control these channels.

After measuring the  $10 \times 10$  transmission matrix and a standard smoothing of the data, we constructed the operator

$$d_x^{(m)} := -it^{-1} \frac{dt}{dx_m}, \quad (3.36)$$

where the symbol  $m$  specifically identifies  $x_m$  as the position of the metallic scatterer. For the projection and inversion of the  $t$ -matrix in (3.36), we kept all 10 singular values in this case, i.e., we performed a direct inversion. The derivative of  $t$  was done by recording the transmission amplitudes for three different positions  $x_m$ , where the scatterer was moved in the direction transverse to the incident flux (see Fig. 3.10) by a distance equal to its radius in each step.

With the operator  $d_x^{(m)}$  at hand, its eigenstates were calculated and reinjected into the system. Figs. 3.11 and 3.12, show the measured intensities for the part of the scattering region centered around the metallic scatterer, for those eigenstates corresponding to the three highest and three lowest real parts in their eigenvalues, respectively. For the sake of visibility, we also measured the intensity profile having the metallic scatterer removed from the system for each of the states, keeping in mind, however, that this procedure affects the focussing states, while the avoiding states are left largely unaffected. From both figures, we clearly see our predictions confirmed: the states corresponding to the highest eigenvalues show a clear focus, the states corresponding to the lowest eigenvalues, in turn, omit the metallic scatterer.

In Eq. (3.36) and the preceding derivations of this section and section 2.6, we have thus introduced a previously unknown operator derived from our general DEFT-class, and were able to put it into a solid theoretical framework. This operator can be used for both focussing on a selected target inside a scattering medium, or omitting the specified target while illuminating other parts of the system under study. Whereas already quite a few concepts of focusing even in the spatio-temporal domain in complex media exist [13,14,34,109], to our best knowledge, the omission of a specified region is a completely new approach. As we will discuss in greater detail in the upcoming subsection, however, our methods might also even improve existing focusing techniques. Regarding the novel possibility to avoid a certain region, we envision possible implementations of our concepts in situations where the protection of a highly sensitive fabric is imperative while simultaneously irradiating its surroundings is requested, e.g., the omission of healthy organs in medical applications. Another example would be secure communication, where an eavesdropper resides at an unfavorable, but well-known location. Using our algorithm, a secret message could be spread

while avoiding the selected region, where the signal is suppressed to noise level.

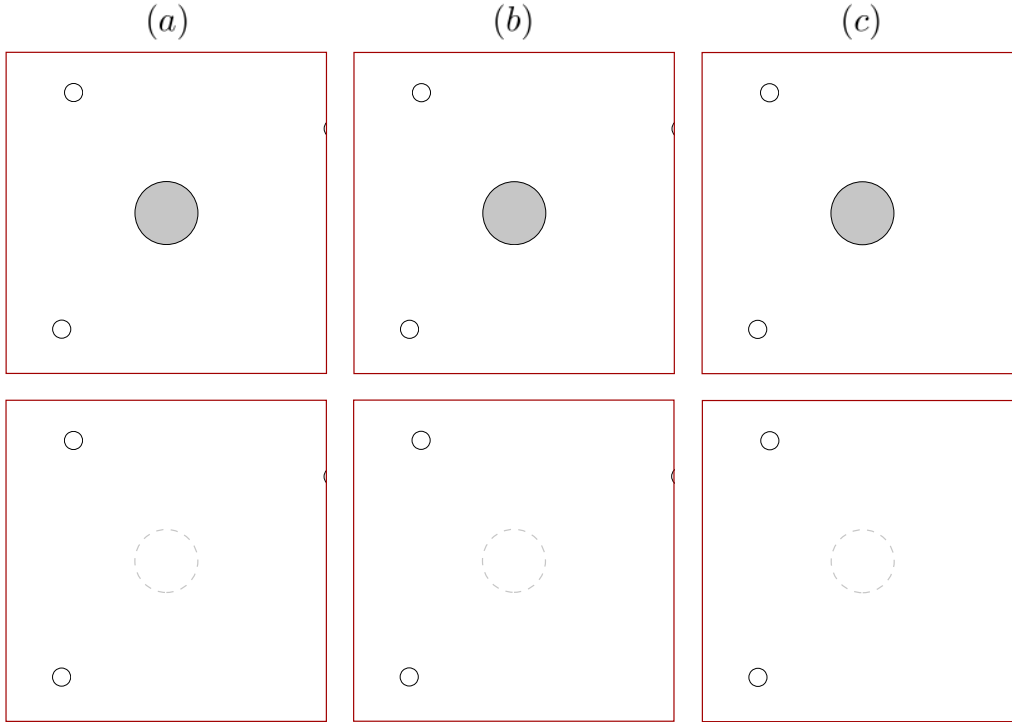


**Figure 3.11:** (a)-(c) Measured intensity plots for the three  $d_x^{(m)}$ -eigenstates with the largest eigenvalues of  $|\kappa_x^{(m)}| = 133.4, 162.8, \text{ and } 193.2$  [a.u.], respectively. The region around the metallic scatterer (grey) shown is the area highlighted in Fig. 3.10. For all three states, a strong focus on the metallic cylinder is clearly visible (upper panel). The lower panel shows the same input configuration injected into the resonator without the metallic scatterer, where the focussing behaviour becomes even more apparent. Note, however, that the intensity patterns are generally changed by removing the center scatterer.

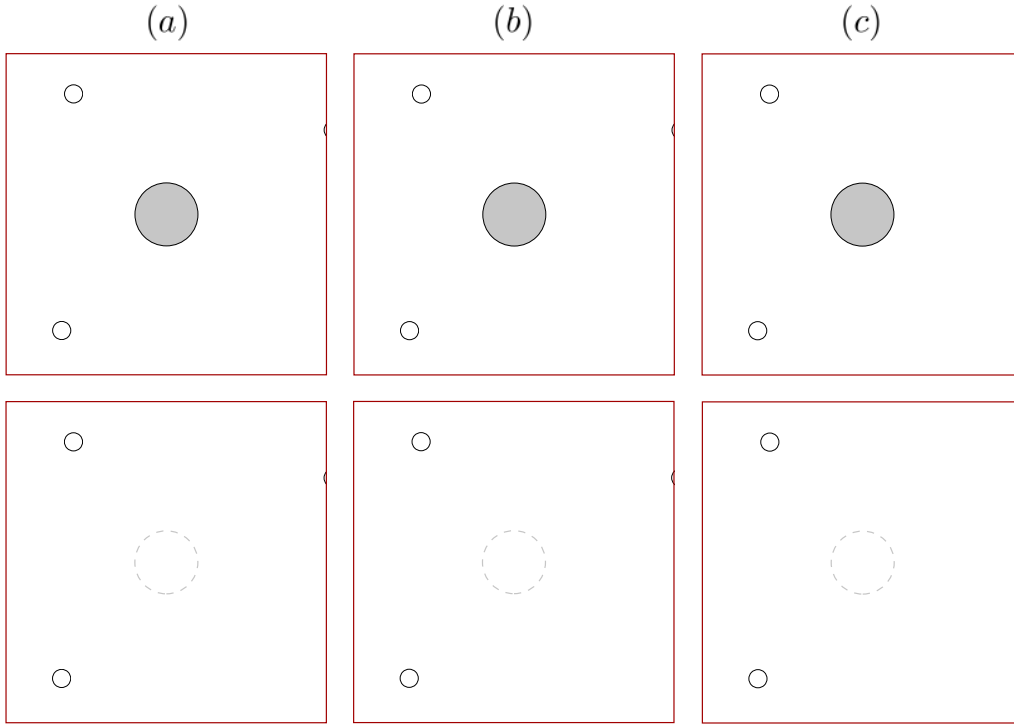


**Figure 3.12:** (a)-(c) Measured intensity plots for the three  $d_x^{(m)}$ -eigenstates with the lowest eigenvalues of  $|\kappa_x^{(m)}| = 3.8, 4.2,$  and  $12.0$  [a.u.], respectively. The region around the metallic scatterer (grey) shown is the area highlighted in Fig. 3.10. For all three states, a strong avoidance of the metallic cylinder and its surroundings is clearly visible (upper panel). The lower panel shows the same input configuration injected into the resonator without the metallic scatterer, for the sake of a better visibility of the omitted region. As we expected, the intensity patterns for these states are almost undisturbed by the removal of the center scatterer.

### Connection to Focussing on a Moving Target

In a recent experiment in the optical domain carried out by Zhou et al. in 2014 [34], the authors presented an algorithm that allows focussing on a target behind a disordered medium by a dynamical measurement of the system's reflection matrix, and directly succeeded in proving their claims experimentally in a quite impressive fashion. In this subsection, we will briefly discuss the connection of this experiment and the exploited algorithm to our DEFT-operator class, more specifically to the shift operator  $d_x^{(m)}$  defined in Eq. (3.36). Moreover we can even outline a refinement to the methods in [34]. Results preliminary to those shown here have been produced by Stephan Hübsch in the framework of his bachelor thesis that I co-advised [110].

The focussing procedure suggested by Zhou et al. basically works in two steps: In a first step, the reflection matrix for a system with the target particle at a location specified by the scalar coordinate  $x_1$ ,  $r(x_1)$ , is recorded. In the second step, the reflection matrix is again measured, now with the particle at a different location  $x_2$ . The main idea of the method is to subtract both reflected signals for a given input state  $\vec{u}$  from each other, which results in an elimination of the 'background' signal stemming from all other scatterers except the target particle. In this way, only that portion of the signal remains, that corresponds to scattering on the target (again in the complex interplay of all other scatterers). After time-reversal by complex conjugation, this signal is launched back into the system. Mathematically, the expression for the input configuration  $\vec{u}'$  which ultimately leads to a focusing on the chosen particle thus reads

$$\vec{u}' = \{[r(x_2) - r(x_1)] \vec{u}\}^* . \quad (3.37)$$

If this technique is repeated each time the position of the particle changes, a dynamical tracking of the target in terms of focussing can be achieved.

For the sake of a better comparability to the microwave experiment discussed above, we performed numerical simulations, where all system dimensions as well as the materials and radii of the scatterers, as well as the input frequency were chosen to match those of the specific setup we studied there (see Fig. 3.10, the simulated random placement of the 18 teflon scatterers is now different though). Instead of solving the full Maxwell equations, we restricted ourselves to the scalar Helmholtz equation in Eq. (2.2). The metallic target was again placed directly inside rather than behind the disordered region. Moreover, we will use the transmission matrix  $t(x_{1,2})$  rather than the reflection matrix.

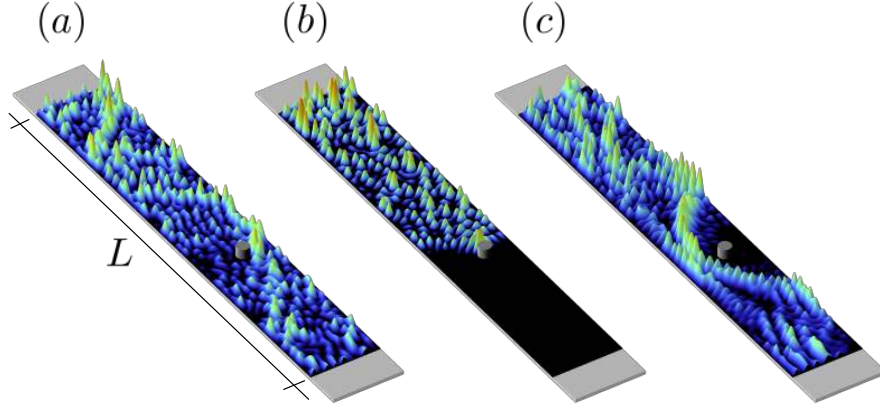


**Figure 3.13:** Intensity plots (a) for the input configuration  $\vec{u}' = \rho(x_2, x_1)\vec{u}$  resulting from a random  $\vec{u}$ , and (b), (c) for the eigenstates of  $\rho(x_2, x_1)$  corresponding to the highest and lowest eigenvalues, respectively. The used discrete displacement of the target in transverse direction,  $\Delta x = x_2 - x_1$ , was equal to its diameter. The setup is chosen very similar to the experimental setup discussed in Fig. 3.10: 18 teflon scatterers (not shown) were randomly placed inside the scattering region of length  $L$ , surrounding the metallic target cylinder which is shown in grey. The positions of the smaller scatterers and the target are different than in Fig. 3.10 though. The wave was injected from the left for all three plots.

Our first step of refining Eq. (3.37) is by substituting the complex conjugation in Eq. (3.37) by an actual backpropagation of the signal in terms of using the inverse  $t^{-1}(x_1)$ ,

$$\vec{u}' = -i t^{-1}(x_1) \frac{t(x_2) - t(x_1)}{x_2 - x_1} \vec{u} := \rho(x_2, x_1) \vec{u}. \quad (3.38)$$

Multiplication with the purely imaginary factor  $-i/(x_2 - x_1)$  just corresponds to a global rescaling of the input configuration  $\vec{u}'$  and, therefore, does not principally affect the algorithm. We can identify the resulting operator acting on  $\vec{u}$  with the  $\rho$ -operators previously introduced in Eq. (3.26) in section 3.4, yet for the position identifier  $x$  now rather than for the input frequency  $\omega$ . In Fig. 3.13(a) we show the intensity plot for the input configuration computed using Eq. 3.38 where we started from a random input configuration  $\vec{u}$ . The discrete stepsize in  $x$  was chosen to equal twice the radius of the target which was again shifted in transverse direction. Although a focusing on the metallic cylinder in our system allowing only for 10 propagating modes can be seen, the effect is not overly pronounced. Further, we

were not able to find a random input configuration that actually leads to an avoidance of the target. The situation drastically changes though, if we do not start with some random input configuration, but specifically inject the eigenstates of  $\rho(x_2, x_1)$  corresponding to the largest and lowest eigenvalues as we did before using the operator in  $d_x^{(m)}$  in Eq. (3.36). Figs. (3.13)(b) and (c) show the resulting intensity plots from which we see a very pronounced focus in (b), as well as a clear omission in (c).

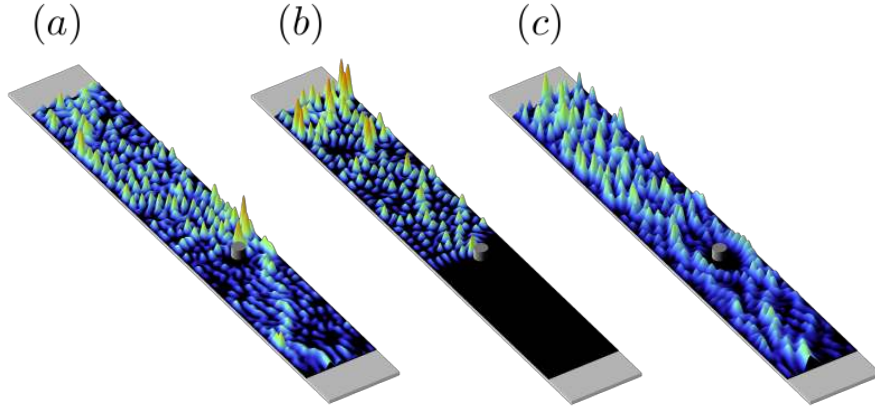


**Figure 3.14:** Intensity plots (a) for the input configuration  $\vec{u}' = d_x^{(m)}\vec{u}$  resulting from a random  $\vec{u}$ , and (b), (c) for the eigenstates of  $d_x^{(m)}$  corresponding to the highest and lowest eigenvalues, respectively. The simulated system is the same as discussed in Fig. 3.13 and in the main text.

The connection to the DEFT-operator  $d_x^{(m)}$  can easily be drawn using the operators  $\rho(x_2, x_1)$ , since, completely analogous to the time delay operator  $q$  in section 3.4,  $d_x^{(m)}$  is obtained in the limit

$$d_x^{(m)} = \lim_{\Delta x \rightarrow 0} -i t^{-1}(x) \frac{t(x + \Delta x) - t(x)}{\Delta x} = \lim_{\Delta x \rightarrow 0} \rho(x + \Delta x, x), \quad (3.39)$$

with  $\Delta x = x_2 - x_1$ . By applying this operator to a random input  $\vec{u}' = d_x^{(m)}\vec{u}$ , we obtained the intensity profile displayed in Fig. 3.14(a). Much similar to the corresponding plot for a discrete step  $\Delta x$  in Fig. 3.13(a), also the continuous variation in  $x$  leads to a more or less apparent focus. Again, we can improve the quality of the focus significantly by injecting the eigenstate of  $d_x^{(m)}$  possessing the largest eigenvalue, as visible in Fig. 3.14(b). The state corresponding to the lowest eigenvalue produces once again a clear avoidance of the target area (Fig. 3.14(c)).

Summarizing, we could demonstrate an intimate connection between the experiment in [34] and our DEFT-operators by modifying the original operational procedure from Eq. (3.37) to Eq. (3.38), and finally proceeding to the operator given in Eq. (3.39). The key mathematical ingredient shared by all of these equations is the difference of the matrices  $t(x_2) - t(x_1)$  (or analogous for the reflection matrix). Injecting appropriate eigenstates of the involved operators rather than starting from a random input vector, proved to be very advantageous in terms of both focussing and avoiding.

## Occupying Regular Islands in Classical Phase Space

The DEFT-operator class is the proper generalization of the time delay operator (2.44), or more generically (2.45), not only by means of the construction scheme and the correlation bandwidths of the eigenstates of its members. In case the investigated system allows for such propagation patterns, also the remarkable ability to find particlelike states can be inherited from the time delay operator(s) by other operators of the DEFT class. A generation of such highly-collimated particlelike propagation patterns might be especially desirable for the purposes of secure and/or low power communication, or of focussing in rather weakly disordered media (see also [30]). However, as we will discuss in this subsection, cases exist, where the time delay operator is not capable of yielding the desired input patterns among its eigenstates, in spite of the proper conditions principally allowing for their existence. More specifically, we will demonstrate that one of those distinct DEFT-members able to resolve this drawback is actually given by the operator defined in Eq. (3.31). The wave intensity and phase space plots shown here, as well as the preceding numerical simulations were produced and performed, respectively, by Matthias Kühmayer, who studied this matter in the course of his diploma thesis that I co-advised [111].

In order to demonstrate our claims with respect to the generation of particlelike states, we studied the following system: A straight glass fiber with a D-shaped cross section [112], as depicted in Fig. 3.15(a). We further assume homogeneous refractive indices of  $n_{\text{fib}} = 1.5$  and  $n_{\text{surr}} = 1.0$  for the fiber and its surrounding, respectively. Due to the cylindrical symmetry in the direction perpendicular to the D-profile,  $z$ , the system can be thought of as a two-dimensional one, where the time replaces the propagation distance  $z$ . The time delay operator  $Q$  does not provide particlelike states in such a system, but rather the appropriate waveguide modes corresponding to the D-shaped cross section - a fact that also stems from this symmetry. Since the lead modes feature well-defined propagation constants in the direction of propagation, they also feature well-defined delay times, due to the complete absence of mode-mixing caused by the system's translational invariance.

The specific D-shape we chose can be envisioned as having been cut from an integrally cylindrical fiber. As it was shown, depending on where the plane defining this cut is placed, the cross section features regular, chaotic, or mixed temporal dynamics of trajectories (or rays) [113]. Here, we will restrict ourselves to the interesting case of mixed phase space dynamics, corresponding to a ratio of the fiber-radius,  $r_{\text{fib}}$ , and the cut parameter,  $r_{\text{cut}}$  (see Fig. 3.15(a) for definitions), of  $f := r_{\text{cut}}/r_{\text{fib}}$ ,  $1 < f < 2$ . A convenient choice for a pair of coordinates in the associated two-dimensional, reduced

phase space are so-called Birkhoff coordinates [36]. They consist of the normalized polar angle  $\bar{\varphi} = \varphi/\varphi_{\max}$ , and the momentum component tangential to the boundary characterized by  $\bar{k}_\varphi = k_\varphi/k$  (see Fig. 3.15(a)), which are recorded every time a trajectory hits the round part of the D-shaped boundary. Launching a great number of trajectories ( $\sim 700$ ) corresponding to a large number of initial conditions reveals the phase space dynamics for our chosen values for the fiber radius  $r_{\text{fib}} = 62.5 \mu\text{m}$  and the cut  $f = 1.05$ , as shown in Fig. 3.15(b): Points in the  $(\bar{k}_\varphi, \bar{\varphi})$ -space hit by a trajectory during its propagation are marked, resulting in broad regions of marked space and islands of unmarked sites that are framed and traversed by circular or elliptic figures. Specific groups of islands that are topologically distinct in the considered phase space cross section, are, as we will see, dynamically connected and mirror-symmetric copies of each other. The more homogeneously marked regions and the islands correspond to chaotic and regular dynamics, respectively. Note however, that a simulation of infinitely long propagation times is numerically infeasible, otherwise the marked chaotic space in between the islands in Fig. 3.15(b) would be perfectly filled. The plots of the areas associated to regular dynamics, in turn, owe their partial blankness to their constituent orbits. Since these latter paths are of measure zero in the space of initial conditions, they are unlikely to be hit by a random initial sampling. The effect of chaos on the dynamics of two trajectories with a specific distance in terms of their positions and momenta, is causing this distance to grow exponentially during propagation, whereas it grows only linearly in the regular case [36].

This dynamical behavior makes the regular islands perfectly suited to 'accomodate' particlelike wave states, in particular in comparison with the chaotic sea. Explicitly investigating the propagation of bundles of trajectories lying on the islands reveals that they remain bundled for large propagation distances, thus collectively hitting the boundary with each bounce. In this way, they transfer momentum to the boundary, such that the average value of the bundle's momentum distribution is always non-zero. In contrast to such collimated bundles, a high number of trajectories featuring arbitrary initial conditions will result in a mean momentum of zero.

The translational invariance of geometries like our considered fiber, excludes the time delay operator from the suitable candidates of operators capable of finding particlelike wave states, because its eigenstates are then equal to the non-collimated fiber modes [44, 111]. The perfect candidate for an operator measuring the mean momentum transfer mentioned above for waves, however, is actually given by the one on the right-hand side of Eq. (3.31),  $d_x$ , constructed from the wave transmission amplitudes for our fiber. As shown in the previous chapter in Eqs. (2.78) and (2.72), the eigen-

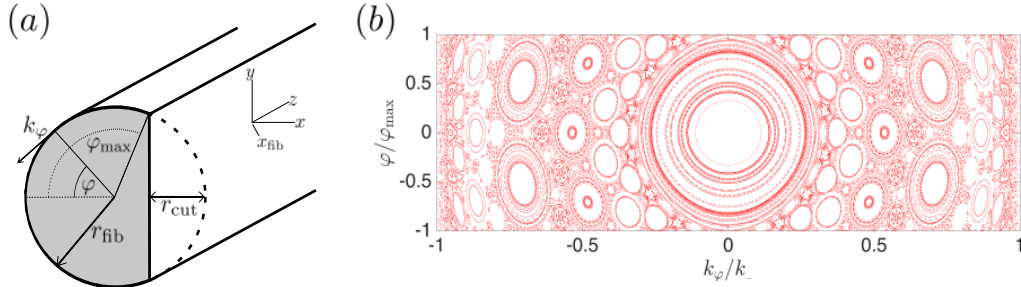


**Figure 3.15:** (a) Sketch of the fiber and its D-shaped cross section (grey). The cross section can be envisioned as a full circle with radius  $r_{\text{fib}}$ , from which a certain fraction has been cut, where the position of the cut is parametrized by  $r_{\text{cut}}$ . The spatial derivative in Eq. (3.40) is taken along the  $x$ -axis, which we chose to be equal to the axis of transverse fiber symmetry. The actual position of the fiber on this axis is denoted by  $x_{\text{fib}}$ . In order to produce the results shown in (b) and Figs. 3.16–3.17, we chose the specific values of  $r_{\text{fib}} = 62.5 \mu\text{m}$  and  $f = 1.05$ . (b) Phase space cross section for the (normalized) Birkhoff coordinates  $(\varphi/\varphi_{\text{max}}, k_{\varphi}/k)$ . The partially filled elliptical islands correspond to trajectories featuring regular dynamics, the regions in between constitute the so-called “chaotic sea”.

values of this operator constitute a measure for the momentum change of an initial wavefront in a specific direction during scattering. In contrast to the situations earlier in this section, we will now vary the location of the *whole* scattering system (the fiber), where we chose this variation with respect to  $x_{\text{fib}}$  to happen along the axis of transverse symmetry of the fiber cross section (see Fig. 3.15(a)). Note that moving the fiber in this way causes a mixing of the original waveguide modes corresponding to the initial position of the fiber cross-section. The appropriate shift operator for this procedure reads

$$d_{x_{\text{fib}}} = -it^{-1} \frac{dt}{dx_{\text{fib}}}. \quad (3.40)$$

The scheme we propose to find particlelike states works in two steps: Firstly, the transmission amplitudes for the fiber and their derivative with respect to a variation of  $x_{\text{fib}}$  are recorded in order to construct and diagonalize the operator  $d_{x_{\text{fib}}}$  in Eq. (3.40). Then, selected eigenstates are injected into the fiber - see [111] for details of both steps. In Figs. 3.16 and 3.17, we show the propagation of two such states, indeed, confirming the success in our approach to generate particlelike states. The wavefronts with an assumed wavelength of  $\lambda = 2\pi/k = 553 \text{ nm}$  stay collimated beams during the entire

propagation, where the reason of two symmetric beams in each of the plots originates in the transverse symmetry of the system with respect to the chosen  $x$ -axis.

So-called Husimi distributions conveniently translate the propagation of waves to the phase space of trajectories [113, 114]. The lower panels of Figs. 3.16 and 3.17 show the respective distributions overlaying the classical phase space structure for the considered states (see [111] for details). One of them occupies bundles of trajectories from the center regular island, whereas the other one corresponds to a group of smaller but dynamically connected outer islands.

We could thus successfully demonstrate that the time delay operator is not the only member of the DEFT-class that can be utilized to create particlelike wave propagation patterns by presenting the specific counterexample of the momentum shift operator  $d_{x_{\text{fib}}}$ . Further, with the specific system we studied for that purpose, we have also shown, that other DEFT-operators might be able to find such favorable states, even in situations where the time delay operator is not. The underlying working principle of the  $d_{x_{\text{fib}}}$ -operator roots on information about the underlying trajectory dynamics of the studied system. As we have found, in case of mixed classical dynamics, the particlelike states are mostly situated on regular islands, which causes the corresponding wavefront to retain their initial collimation even over long propagation distances. We emphasize though, that an exact knowledge of the trajectory phase space is not required for the construction of the wave operator  $d_{x_{\text{fib}}}$ .

Eventually, we would also like to point out, that the output patterns for eigenstates of  $d_{x_{\text{fib}}}$  are generally independent of fiber movements in the specified direction to first order, irrespective of being particlelike or not. Accordingly, the generation of such states might find an application in situations where, despite possible vibrations and/or uncertainties in the exact location of the scattering device, a strong focus is desired.

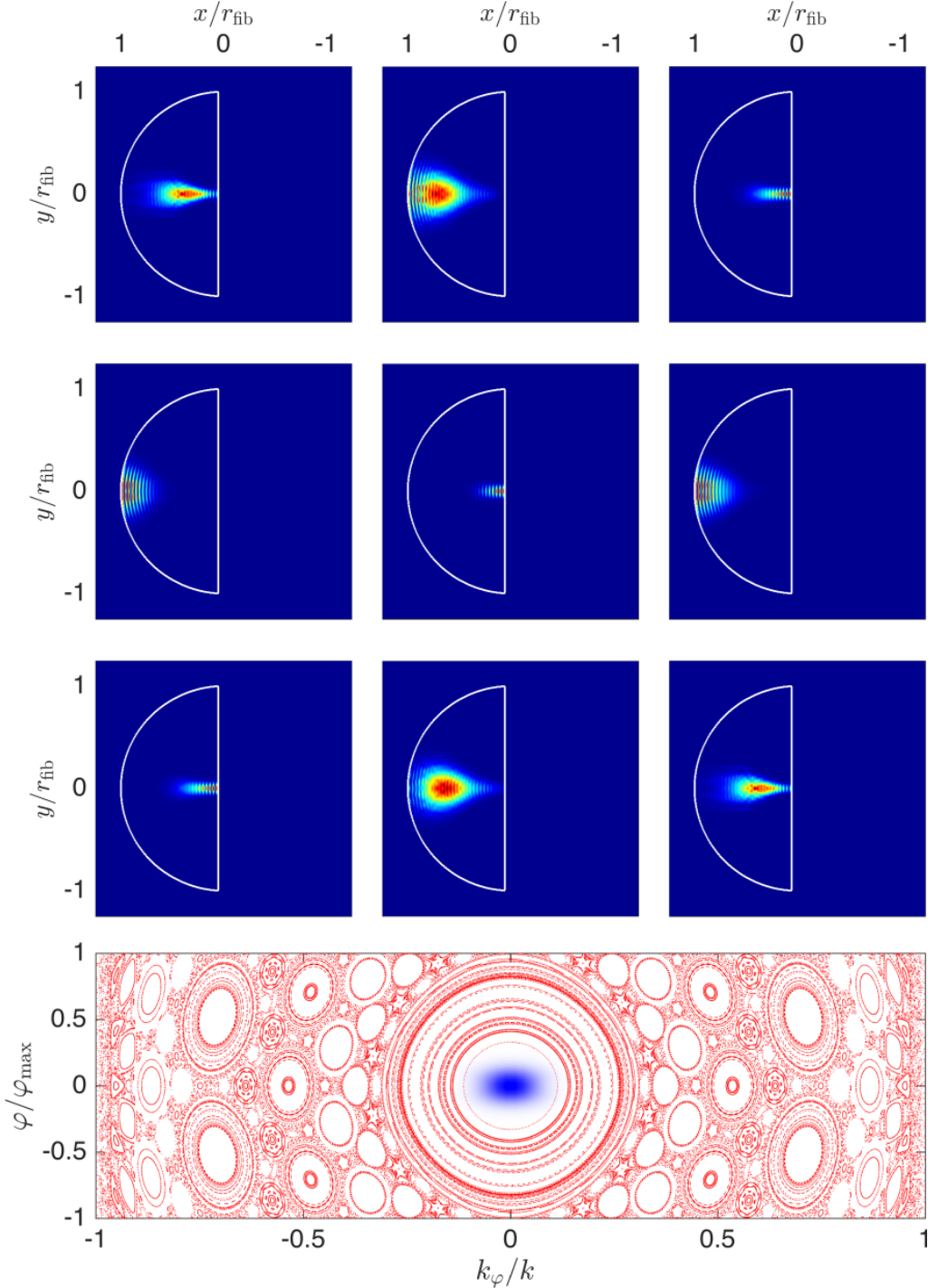


**Figure 3.16:** Intensity plots for an initial wavefront constructed from an eigenstate of the operator  $d_{x_{\text{fib}}}$  in Eq. (3.40) for different propagation distances  $z = [0, 1, 2, \dots, 8] L/8$ , with  $L$  being the length of the fiber (to be read linewise; reddish colors denote high intensity). As can be seen, the intensity pattern stays highly collimated even after several bounces off the fiber boundary. Lower panel: The corresponding Husimi distribution (blue) reveals the state's position on the center regular island in the trajectory phase space.

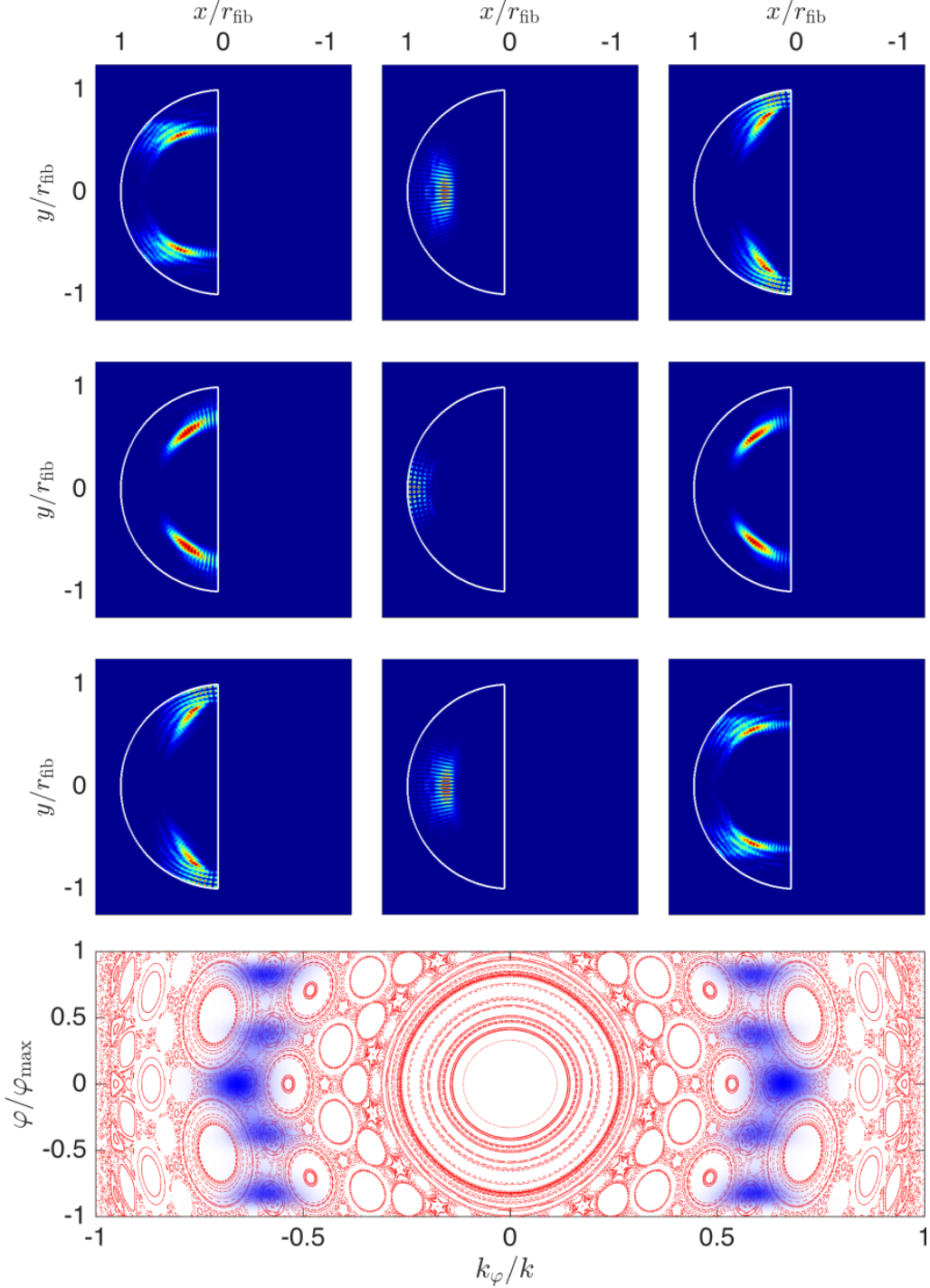


**Figure 3.17:** Intensity plots for an initial wavefront constructed from an eigenstate of the operator  $d_{x_{\text{fib}}}$  in Eq. (3.40) for different propagation distances  $z = [0, 1, 2, \dots, 8] L/8$ , with  $L$  being the length of the fiber (to be read linewise; reddish colors denote high intensity). As can be seen, the intensity patterns stay highly collimated even after several bounces off the fiber boundary. Lower panel: The corresponding Husimi distributions (blue) reveal the state's position on dynamically connected regular islands in the trajectory phase space.

CHAPTER 4 

**Summary and Outlook**

After reviewing the Wigner-Smith time delay operator and deriving several adaptations for the Helmholtz equation, we specifically demonstrated an extension of the mean-chord-length theorem. In order to do so, we exploit the intimate relation between the average delay time, that can be calculated from the trace of this matrix, and the density of states in a given scattering region. Our findings clearly indicate, that this theorem basically also holds for wave transport, even for the regime of Anderson localization that exists for waves only. Quite counterintuitively, we demonstrate that the mean delay time is independent of the actual geometric shape of the investigated system, but rather depends only on its size and the length of its boundary. This result, as we could further show, is linked to the Yablonovitch limit, a fundamental result for the intensity enhancement within solar cells. We could prove that the mean-chord-length theorem and the Yablonovitch limit are essentially two sides of the same medal. Accordingly, our derivations exclude pure geometrical variations from the list of possibilities that might lead to an increase in the effectiveness of future generations of light harvesting devices.

Leaving the immediate environment of the specific expression for a time delay operator proposed by Smith, we presented a generalization of this concept. We could not only physically reason the design principle of this new operator, the meaning of its eigenvalues and properties of its eigenstates, we could also derive versatile construction algorithms, allowing for a broad range of applications of our concepts. These novel construction principles found a direct implementation in two numerical studies we presented. On the one hand, we successfully demonstrated the possibility to address individual branches of the complex propagation pattern evolving in the framework of branched flow. The algorithm we suggested there works in two steps of firstly defining the spatial output region one is interested in, and measuring the corresponding elements of the scattering matrix, and secondly, separating different intensity branches ending in the specified region. This separation works by means of the different wave time delays associated to the branches. Since branched flow systems are not yet available for optical waves, we hope that our work might contribute in pushing the regarding developments. On the other hand, we exploited concepts of wavefront shaping in order to effectively camouflage a strongly disordered region by mimicking the scattering dynamics of a perfectly homogeneous one. In principal, the simple numerical procedure we suggest is capable of hiding any system by feigning the presence of any other setup.

In the context of fiber communication, we could substantially broaden the current bottleneck in frequency stability as set by the principal modes, i.e. eigenstates of the time delay operator, by a purely numerical opti-

mization scheme (in contrast to an experimental feedback loop). The corresponding cost function contains the information of the scattering amplitudes in a whole frequency domain, rather than at a single frequency only. Wide stability bandwidths are especially beneficial for data transfer, since in case of a perfect auto-correlation of the output signal in a whole spectral range, the spatial and temporal traces of a sent pulse decouple. By experimentally demonstrating the practicability of our findings in an optical fiber setup, our results might help increasing the data transfer capacity of optical multi-mode fibers in the future. Furthermore, our gradient-based optimization scheme is actually not restricted to cost functions optimizing pulse transmission, literally any purpose might be pursued if a corresponding cost function can be found.

The unique functional principle of the time delay operator(s) inspired us to generalize these ideas to a whole class of previously unknown operators, which we termed dependence shift or DEFT-operators. The eigenstates of these operators share their output stability with the principal modes, if a certain quantity the scattering matrix parametrically depends on is varied. For the latter time delay eigenstates, this parameter is the frequency of the initial wavefront. For the particular example of the parameter being equal to the spatial position of an individual scatterer inside a scattering medium, we experimentally demonstrated the possibilities of both focussing on the scatterer, and avoiding its surroundings, in a microwave setup. The latter omission is, to the best of our knowledge, an entirely novel approach, and we envision possible medical applications or a usage in secure communication. Exploiting a very similar ansatz, we showed moreover, that shifting the entire scattering region can lead to the formation of particlelike states in systems, where the time delay operator is incapable of producing them. Apart from a possible utilization of the particlelike states in secure or low-energy communication, we envision a further, more general application of the eigenstates of the DEFT-operator we used in this context: Due to their stability with respect to variations of the entire scattering system along a specific direction, we envision an implementation of these states in systems, where possible vibrations cannot be sufficiently compensated for, but a stable output pattern is desired nevertheless.



APPENDIX **A**

**Notion of Time Delay and  
Analytical Results**

## A.1 Average Delay Times and the DOS

### Connection of the Scattering Phases and the Resonance Poles

#### Cayley transform of $S$

Here, we will present the necessary steps of Cayley-transforming the scattering matrix. We start by rewriting

$$S = -\mathbb{1} + 2iV^\dagger G V = -\mathbb{1} + 2iV^\dagger \frac{1}{\Delta + n^2 k^2 + iVV^\dagger} V. \quad (\text{A.1})$$

For reasons of simplicity, we omitted explicitly specifying the Hermitian part of the purely outgoing boundary conditions in the denominator on the right-hand side, but rather only the anti-Hermitian part that can be expressed using the coupling matrix  $V$  (see also [44]). Denoting the Green's function of the Hermitian part as  $G_0 := [\Delta + n^2 k^2]^{-1}$ , we can further rewrite

$$S = -\mathbb{1} + 2iV^\dagger \frac{1}{\Delta + n^2 k^2 + iVV^\dagger} V \quad (\text{A.2})$$

$$= -\mathbb{1} + 2iV^\dagger [G_0^{-1} + iVV^\dagger]^{-1} V \quad (\text{A.3})$$

$$= -\mathbb{1} + 2iV^\dagger [(\mathbb{1} + iVV^\dagger G_0) G_0^{-1}]^{-1} V \quad (\text{A.4})$$

$$= -\mathbb{1} + 2iV^\dagger G_0 \frac{1}{\mathbb{1} + iVV^\dagger G_0} V \quad (\text{A.5})$$

$$= -\mathbb{1} + 2iV^\dagger G_0 \sum_n (-i)^n (VV^\dagger G_0)^n V. \quad (\text{A.6})$$

Reordering according to  $(VV^\dagger G_0)V = V(V^\dagger G_0 V)$  we further get

$$S = -\mathbb{1} + 2iV^\dagger G_0 V \sum_n (-i)^n (V^\dagger G_0 V)^n \quad (\text{A.7})$$

$$= -\mathbb{1} + 2iV^\dagger G_0 V \frac{1}{\mathbb{1} + iV^\dagger G_0 V} \quad (\text{A.8})$$

$$= \frac{-\mathbb{1} - iV^\dagger G_0 V + 2iV^\dagger G_0 V}{\mathbb{1} + iV^\dagger G_0 V} \quad (\text{A.9})$$

$$= \frac{-\mathbb{1} + iV^\dagger G_0 V}{\mathbb{1} + iV^\dagger G_0 V} = -\frac{\mathbb{1} - iV^\dagger G_0 V}{\mathbb{1} + iV^\dagger G_0 V}, \quad (\text{A.10})$$

which is the Caley transform of  $S$  as used in Eq. (2.31).

**Spectral Representation of  $\text{Det}[S]$** 

Starting from

$$\text{Det}[S] = \text{Det} \left[ -\frac{\mathbb{1} - iV^\dagger G_0 V}{\mathbb{1} + iV^\dagger G_0 V} \right] = |-1| \frac{\text{Det}[\mathbb{1} - iV^\dagger G_0 V]}{\text{Det}[\mathbb{1} + iV^\dagger G_0 V]}, \quad (\text{A.11})$$

we move on by proving the identity  $\text{Det}[\mathbb{1} + V^\dagger AV] = \text{Det}[\mathbb{1} + AV^\dagger V]$  [36]. Consider the product of the matrices,

$$C = \begin{pmatrix} \mathbb{1} & 0 \\ -V^\dagger A & \mathbb{1} \end{pmatrix} \begin{pmatrix} A^{-1} & V \\ V^\dagger & \mathbb{1} \end{pmatrix} \begin{pmatrix} \mathbb{1} & -AV \\ 0 & \mathbb{1} \end{pmatrix} = \begin{pmatrix} A^{-1} & 0 \\ 0 & \mathbb{1} - V^\dagger AV \end{pmatrix}, \quad (\text{A.12})$$

and please note the generally different dimensions of the block matrices. We first calculate the determinant of the left-hand side of Eq. (A.12) using  $\text{Det}(AB) = \text{Det}(A)\text{Det}(B)$  which evaluates to

$$\text{Det}[C] = \text{Det}[A^{-1} - VV^\dagger] = \text{Det}[A^{-1}] \text{Det}[\mathbb{1} - AVV^\dagger]. \quad (\text{A.13})$$

For the right-hand side we find

$$\text{Det}[C] = \text{Det}[A^{-1}] \text{Det}[\mathbb{1} - V^\dagger AV]. \quad (\text{A.14})$$

Comparing Eqs. (A.13) and (A.14), we arrive at the desired result

$$\text{Det}[\mathbb{1} - VAV^\dagger] = \text{Det}[\mathbb{1} - AVV^\dagger]. \quad (\text{A.15})$$

Using Eq. (A.15) and inserting for  $A = \pm G_0$ , we find for the determinant of the scattering matrix

$$\text{Det}[S] = \frac{\text{Det}[\mathbb{1} - iV^\dagger G_0 V]}{\text{Det}[\mathbb{1} + iV^\dagger G_0 V]} = \frac{\text{Det}[\mathbb{1} - G_0 iVV^\dagger]}{\text{Det}[\mathbb{1} + iG_0 VV^\dagger]}. \quad (\text{A.16})$$

We further rearrange

$$\text{Det}[S] = \frac{\text{Det}[G_0^{-1} - iVV^\dagger]}{\text{Det}[G_0^{-1} + iVV^\dagger]} = \frac{\text{Det}[G]}{\text{Det}[G^\dagger]} = \frac{\text{Det}[\tilde{G}]}{\text{Det}[\tilde{G}^\dagger]}, \quad (\text{A.17})$$

where we used  $G = [G_0^{-1} + iVV^\dagger]^{-1}$ ,  $G_0^\dagger = G_0$ , and  $\tilde{G} = G n^2$ . Keeping in mind that the ratio of products is equal to the product of the ratios, and that the determinant of a matrix can be expressed as the product of its eigenvalues, we can write in terms of the complex eigenvalues  $\lambda_n$  and using the spectral representation of the Green's function  $\tilde{G}$  (2.26)

$$\text{Det}[S] = \prod_n \frac{k^2 - \lambda_n^*}{k^2 - \lambda_n} = \prod_n \frac{\omega^2 - \omega_n^2 - i\gamma_n/2}{\omega^2 - \omega_n^2 + i\gamma_n/2}. \quad (\text{A.18})$$

This is the expression given by Eq. (2.33).

## Connection of the Average Time and the DOS

### Average Time Delay and the Scattering Phases

We start from the spectral representation of the scattering matrix in terms of its (unimodular) eigenvalues and eigenvectors,

$$S = \sum_n \vec{\alpha}_n e^{i\theta_n} \vec{\alpha}_n^\dagger. \quad (\text{A.19})$$

Since we assumed  $S$  to be unitary in this section, it features an orthonormal eigenbasis which can easily be seen from

$$\begin{aligned} S\alpha &= \alpha\Theta &\rightarrow \alpha^\dagger S^\dagger &= \Theta^* \alpha^\dagger \\ & &\rightarrow \alpha^{-1} S^\dagger &= \Theta^* \alpha^{-1}, \end{aligned} \quad (\text{A.20})$$

where the matrix  $\alpha$  contains column-wise the eigenvectors  $\vec{\alpha}$  and  $\Theta$  is a diagonal matrix containing the eigenvalues  $\exp(i\theta_n)$ . We conjugated the eigenvalue equation for the upper, and inverted it for the lower expression on the right-hand side of Eq. (A.20), using  $S^\dagger = S^{-1}$  and  $\exp(i\theta_n)^* = \exp(-i\theta_n)$ . We thus found  $\alpha^\dagger = \alpha^{-1}$ . Accordingly, we can write

$$\frac{dS}{d\omega} = \sum_n e^{i\theta_n} \left( i\dot{\theta}_n \vec{\alpha}_n \vec{\alpha}_n^\dagger + \dot{\vec{\alpha}}_n \vec{\alpha}_n^\dagger + \vec{\alpha}_n \dot{\vec{\alpha}}_n^\dagger \right), \quad (\text{A.21})$$

where we abbreviated the derivative  $da/d\omega = \dot{a}$ . Inserting Eqs. (A.19) and (A.21) into  $Q = -iS^\dagger dS/d\omega$ , we get for the time delay operator with  $\vec{\alpha}_n^\dagger \vec{\alpha}_m = \delta_{mn}$ ,

$$Q = \sum_n \left( \dot{\theta}_n \vec{\alpha}_n \vec{\alpha}_n^\dagger - i\vec{\alpha}_n \dot{\vec{\alpha}}_n^\dagger - i \sum_m e^{i(\theta_m - \theta_n)} \vec{\alpha}_n^\dagger \dot{\vec{\alpha}}_m \vec{\alpha}_n \vec{\alpha}_m^\dagger \right). \quad (\text{A.22})$$

Its trace evaluates followingly to

$$\text{Tr}(Q) = \sum_l \vec{\alpha}_l^\dagger Q \vec{\alpha}_l = \sum_l \frac{d\theta_l}{d\omega}. \quad (\text{A.23})$$

For the last equal sign we used

$$\vec{\alpha}_l^\dagger \vec{\alpha}_l \equiv 1 \quad (\text{A.24})$$

$$\rightarrow \frac{d}{d\omega} (\vec{\alpha}_l^\dagger \vec{\alpha}_l) = \frac{d\vec{\alpha}_l^\dagger}{d\omega} \vec{\alpha}_l + \vec{\alpha}_l^\dagger \frac{d\vec{\alpha}_l}{d\omega} = 0 \quad (\text{A.25})$$

$$\rightarrow i \frac{d\vec{\alpha}_l^\dagger}{d\omega} \vec{\alpha}_l = -i \vec{\alpha}_l^\dagger \frac{d\vec{\alpha}_l}{d\omega}. \quad (\text{A.26})$$

Bearing in mind that the determinant of the  $S$ -matrix is just the product of its eigenvalues,

$$\text{Det}(S) = \prod_n e^{i\theta_n} = e^{i\sum_n \theta_n}, \quad (\text{A.27})$$

we arrive at our desired result in Eq. (2.35) by comparing Eqs. (A.23) and (A.27),

$$\text{Tr}(Q) = -i \frac{d}{d\omega} \ln(\text{Det}[S]). \quad (\text{A.28})$$

### Average Time Delay and the Resonance Poles

From Eq. (2.36) in the main text, we calculate

$$\begin{aligned} \frac{d}{d\omega} \ln(\text{Det}[S]) &= \frac{d}{d\omega} \sum_n \ln\left(\frac{\omega^2 - \omega_n^2 - i\gamma_n/2}{\omega^2 - \omega_n^2 + i\gamma_n/2}\right) \\ &= 2\omega \sum_n \frac{\omega^2 - \omega_n^2 + i\gamma_n/2}{\omega^2 - \omega_n^2 - i\gamma_n/2} \left( -\frac{\omega^2 - \omega_n^2 - i\gamma_n/2}{(\omega^2 - \omega_n^2 + i\gamma_n/2)^2} + \frac{1}{\omega^2 - \omega_n^2 + i\gamma_n/2} \right) \\ &= 2\omega \sum_n \left( \frac{1}{\omega^2 - \omega_n^2 - i\gamma_n/2} - \frac{1}{\omega^2 - \omega_n^2 + i\gamma_n/2} \right) \\ &= 4i\omega \sum_n \frac{\gamma_n/2}{(\omega^2 - \omega_n^2)^2 + \gamma_n^2/4} \end{aligned} \quad (\text{A.29})$$

Multiplication with  $-i/N$  yields Eq. (2.37).

## A.2 The Dwell Time

### Energy Density and Power Flux for the Helmholtz Equation

In this subsection we will physically reason the expressions for the densities of the energy and the power flux we used for the Helmholtz equation in the main text. For didactic reasons, we will give an intuitive sketch rather than a rigorous derivation. For that purpose, we start from the Maxwell

equations,

$$\vec{\nabla} \cdot \vec{D} = \rho_f \quad (\text{A.30})$$

$$\vec{\nabla} \times \vec{E} = -\frac{\partial \vec{B}}{\partial t} \quad (\text{A.31})$$

$$\vec{\nabla} \times \vec{H} = \vec{j}_f + \frac{\partial \vec{D}}{\partial t}, \quad (\text{A.32})$$

where we used the definitions of the fields  $\vec{D} = \epsilon_0 \epsilon_r \vec{E}$ , and  $\vec{H} = \mu_0 \mu_r \vec{B}$ , respectively. We now assume the very simple case of a perfectly homogeneous, isotropic, source-free, and non-magnetic, dielectric medium, thus  $\epsilon_r(\vec{x}) \equiv \epsilon_r$ ,  $\rho_f \equiv 0$ ,  $\vec{j}_f \equiv 0$ , and  $\mu_r \equiv 1$ . Accordingly, we can write for the diffractive index  $n = \sqrt{\epsilon_r}$ , and the Maxwell equations simplify to

$$\vec{\nabla} \cdot \vec{E} = 0 \quad (\text{A.33})$$

$$\vec{\nabla} \times \vec{E} = -\mu_0 \frac{\partial \vec{H}}{\partial t} \quad (\text{A.34})$$

$$\vec{\nabla} \times \vec{H} = \epsilon_0 n^2 \frac{\partial \vec{D}}{\partial t}. \quad (\text{A.35})$$

Inserting Eq. (A.35) into Eq. (A.34) and using Eq. (A.33) yields

$$\Delta \vec{E}(\vec{x}, t) = \frac{n^2}{c^2} \frac{\partial \vec{E}(\vec{x}, t)}{\partial t}, \quad (\text{A.36})$$

where we also used  $c = \sqrt{\epsilon_0 \mu_0}$  for the vacuum speed of light. We now further assume a linearly polarized wave and make the time-harmonic ansatz  $\vec{E}(\vec{x}, t) = E_z(\vec{x}) \hat{e}_z \exp(-i\omega t)$  with  $\hat{e}_z = (0, 0, 1)^T$ , and arrive at the Helmholtz equation

$$\left( \Delta + n^2 \frac{\omega^2}{c^2} \right) E_z(\vec{x}) = 0, \quad (\text{A.37})$$

which is perfectly equivalent to the Helmholtz equation in (2.2) in the main text for the case of a uniform index of refraction  $n$ . Identifying the electromagnetic field component  $E_z(\vec{x})$  with the field  $\psi(\vec{x})$ , and using the linear dispersion  $k = \omega/c$ , we get exactly the expression in Eq. (2.2). Eq. (A.37) is solved by a plane wave ansatz

$$E_z(\vec{x}) = A e^{iknx}, \quad (\text{A.38})$$

where we assumed the direction of propagation to be equal to the  $x$ -direction. From Eq. (A.38) and calculating from Eq. (A.34), we thus find for the fields

$$\vec{E}(\vec{x}, t) = A e^{i(knx - \omega t)} \hat{e}_z, \quad (\text{A.39})$$

and

$$\vec{H}(\vec{x}, t) = -\frac{kn}{\mu_0\omega} A e^{i(knx-\omega t)} \hat{e}_y. \quad (\text{A.40})$$

Using these expressions, we can finally calculate the time-averaged electromagnetic energy density  $\epsilon$  and the Poynting vector, i.e., the power current density  $\vec{s}$ ,

$$\epsilon = \frac{1}{2} \left( \vec{E} \cdot \vec{D}^* + \vec{H} \cdot \vec{B}^* \right) = \frac{1}{2} \epsilon_0 n^2 |E_z|^2, \quad (\text{A.41})$$

and,

$$\vec{s} = \frac{1}{2} \vec{E} \times \vec{H}^* = \frac{1}{2} \epsilon_0 n^2 |E_z|^2 \frac{c}{n} \hat{e}_x. \quad (\text{A.42})$$

Please note that this expression for the power flux density features the familiar form of a flux density,  $\vec{s} = \epsilon v$ , with  $\epsilon$  being the energy density and  $v = c/n$  the energy velocity. Using the correspondence to the scalar Helmholtz equation,  $E_z(\vec{x}) = \psi(\vec{x})$ , we can also express (A.41), (A.42) in terms of  $\psi(\vec{x})$  like,

$$\epsilon(\vec{x}) = \frac{1}{2} \epsilon_0 \psi^*(\vec{x}) n^2(\vec{x}) \psi(\vec{x}), \quad (\text{A.43})$$

$$\begin{aligned} \vec{s}(\vec{x}) &= \frac{1}{2} \epsilon_0 c \psi^*(\vec{x}) n(\vec{x}) \psi(\vec{x}) \hat{e}_x \\ &= \frac{1}{2} \epsilon_0 \frac{ic}{2k} \left( \psi(\vec{x}) \vec{\nabla} \psi^*(\vec{x}) + \text{c.c.} \right), \end{aligned} \quad (\text{A.44})$$

as is easily verified utilizing the ansatz in Eq. (A.38). The trivial (non-) dependence of the refractive index on the position  $\vec{x}$  written above is only a formal one. However, we will now use Eqs. (A.43), (A.44) we derived based on our simplifying assumptions as an approximation for the general, local expressions for the energy and power flux densities, and the electric field, respectively (see also [115] and refs. therein). An integration over the whole volume of the scattering region  $\Omega$  then yields for the total stored energy

$$U_\Omega = \int_\Omega dV \epsilon(\vec{x}) = \frac{1}{2} \epsilon_0 \int_\Omega dV \psi^*(\vec{x}) n^2(\vec{x}) \psi(\vec{x}), \quad (\text{A.45})$$

which is the expression (2.62) we used in the main text. As the last step in this subsection, we now also perform an integration of the power flux density over the whole boundary of the scattering area,

$$S_{\partial\Omega}^{(\text{in})} = \int_{\partial\Omega} d\vec{A} \cdot \vec{s}(\vec{\xi}) = \frac{1}{2} \epsilon_0 \frac{ic}{2k} \int_{\partial\Omega} d\vec{A} \cdot \left( \psi(\vec{\xi}) \vec{\nabla} \psi^*(\vec{\xi}) + \text{c.c.} \right), \quad (\text{A.46})$$

which in turn is equal to Eq. (2.63) in the main text.

### Connection of $Q_d$ and $Q$

Before we treat the relation of the time delay operators  $Q_d$  and  $Q$ , we derive an identity we will need to do so. We start from the expression for the scattering matrix

$$S = -\mathbb{1} + 2iV^\dagger GV, \quad (\text{A.47})$$

and write using the unitarity  $S^\dagger S = \mathbb{1}$ ,

$$\begin{aligned} S^\dagger S &= (-\mathbb{1} - 2iV^\dagger G^\dagger V)(-\mathbb{1} + 2iV^\dagger GV) \\ &= \mathbb{1} + 2iV^\dagger G^\dagger V - 2iV^\dagger GV + 4V^\dagger G^\dagger VV^\dagger GV \\ &= \mathbb{1}. \end{aligned} \quad (\text{A.48})$$

For the last equal sign to hold generally, the relation

$$4G^\dagger VV^\dagger G = 2i(G - G^\dagger) \quad (\text{A.49})$$

must be valid. Inserting the expression (A.47) in the defining equation for the Wigner-Smith operator,  $Q = -iS^\dagger dS/d\omega$ , and neglecting the frequency dependence of  $V$ , we find

$$\begin{aligned} Q &\approx -i(-\mathbb{1} - 2iV^\dagger G^\dagger V)(2iV^\dagger \dot{G}V) \\ &= -i(-2iV^\dagger \dot{G}V + 4V^\dagger G^\dagger VV^\dagger \dot{G}V), \end{aligned} \quad (\text{A.50})$$

where we abbreviated the derivative  $dA/d\omega$  with  $\dot{A}$ . Using  $G = (\Delta + n^2 k^2 + iVV^\dagger)^{-1}$ , and the dispersion relation  $\omega = kc$ , we find for the derivative of the Green's function (see also [116])

$$\dot{G} = -\frac{2k}{c} G n^2 G. \quad (\text{A.51})$$

Hence, we can further write

$$Q \approx \frac{2k}{c} (2V^\dagger G n^2 G V + 4iV^\dagger G^\dagger VV^\dagger G n^2 G V). \quad (\text{A.52})$$

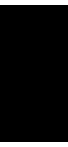
Using the identity (A.49) for the last term on the right-hand side we finally obtain

$$\begin{aligned} Q &\approx \frac{2k}{c} (2V^\dagger G n^2 G V - 2V^\dagger G n^2 G V + 2V^\dagger G^\dagger n^2 G V) \\ &= \frac{4k}{c} V^\dagger G^\dagger n^2 G V \\ &= Q_d, \end{aligned} \quad (\text{A.53})$$

where we used  $Q_d = 4k V^\dagger G^\dagger n^2 G V/c$ .

APPENDIX

B



**Numerical & Experimental  
Results and Applications**

## B.1 A Universal Time as an Invariance Property of Wave Scattering

### Statistical Signature for the Chaotic and the Localized Regime

In the main text, we discuss systems featuring ballistic, chaotic and localized wave scattering, respectively. The corresponding scattering regime is determined by the number and size of impenetrable obstacles we placed inside the scattering region, and can be characterized through the regime-specific transmission statistics. For the ballistic system, transmission is perfect in our case, since without any scatterers, we are dealing with a perfectly transmitting waveguide. In order to verify that the scattering in the systems containing a finite number of obstacles is chaotic and localized, respectively, we check whether the transmission statistics follow the respective predictions. For that purpose, we calculated the eigenvalues  $\zeta_i$  of the matrix  $t^\dagger t$ , where  $t$  is the transmission matrix. For chaotic dynamics, the  $\zeta_i$  follow the bimodal distribution [117–119]

$$P(\zeta) = \frac{1}{\pi\sqrt{\zeta(1-\zeta)}}. \quad (\text{B.1})$$

In a sample with Anderson localization, only one single transport channel dominates the transmission [95], such that the total transmission,  $T = \sum_{i=1}^{N/2} \zeta_i \approx \zeta_{\max} \equiv T$ , follows the prediction for a one-dimensional wire-geometry with disorder [94, 95],

$$P(T) = Z \frac{\sqrt{\text{arccosh}(T^{-1/2})}}{T^{3/2}(1-T)^{1/4}} \exp\left(-\frac{l'_{\text{loc}}}{2L} \text{arccosh}^2(T^{-1/2})\right), \quad (\text{B.2})$$

with  $Z$  being a normalization constant. The effective localization length  $l'_{\text{loc}} = -2L/\langle \ln T \rangle$  (the brackets here mean an average over different random realizations of the positions of the hard-wall scatterers) can be determined from the numerical data. Figure B.1(a),(b) shows the comparison of the numerically calculated histograms of  $\zeta$  and  $T$ , respectively, and their analytical predictions (B.1) and (B.2). We find that in both cases, the numerical data fits very well the analytical formulae, which confirms our assumptions about the scattering dynamics being chaotic or localized for the two different situations considered.

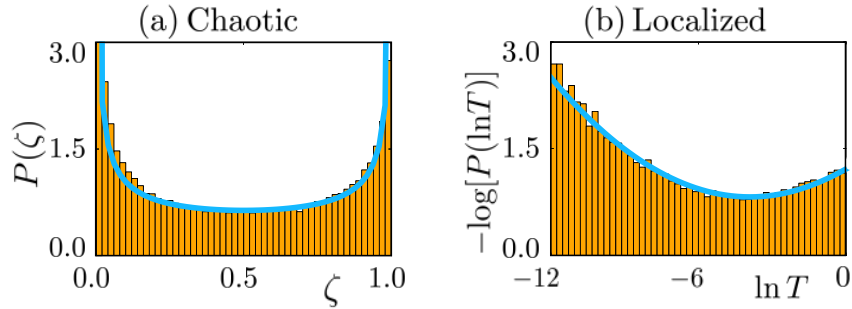


**Figure B.1:** Transmission statistics for different transport regimes. (a) Distribution of the  $t^\dagger t$  eigenvalues  $\zeta$  for chaotic scattering (orange bars), compared with the prediction, Eq. (B.1) (light blue line). (b) Distribution of the total transmission  $T$  for localized scattering compared with the prediction based on Eq. (B.2). To produce the histograms,  $k$  was scanned between  $k = 12.1\pi/d$  and  $k = 12.9\pi/d$  and 1000 scatterer configurations were considered for each of the cases (a),(b) (in (a) only values  $0.01 < \tau < 0.99$  were considered for the histogram).

## The Invariant Average Delay Time and the Yablonoitch Limit

The surface roughness used for the calculations leading to the results plotted in Fig. 3.6 in the main text, is described by the function [102],

$$h(y) = \sum_{m=-M_r}^{M_r} \alpha_m \sin\left(\frac{m\pi}{w}y\right) + h_0, \quad y \in [0, w] \quad (\text{B.3})$$

where the integer number  $M_r$  defines the number of spatial frequencies contributing to the rippled surface,  $2M_r + 1$ . The real numbers  $\alpha_m$  are randomly drawn from a uniform distribution,  $\alpha_m \in [0, w]$ , and the constant  $h_0$  ensures a positive value of  $h(y)$ . For the specific calculations in Fig. 3.6, we set  $w = 1$  for the width of the system, and  $M_r = 46$  as well as  $h_0 = 0.05$ .

## B.2 Orthogonal Super Principal Modes

### Eigenstates of the Recurrence Operator

The eigenvalue equation for an eigenstate of  $\rho(\omega, \omega_0)$  reads

$$\rho(\omega, \omega_0) \hat{u} = -i t^{-1}(\omega_0) \frac{t(\omega) - t(\omega_0)}{\omega - \omega_0} \hat{u} = \varsigma \hat{u}, \quad (\text{B.4})$$

with the complex eigenvalue  $\varsigma$ . Much analogous to the derivations in section 2.4, we can rearrange Eq. (B.4) like

$$\begin{aligned} \frac{t(\omega) - t(\omega_0)}{\omega - \omega_0} \hat{u} &= i \varsigma t(\omega_0) \hat{u} \\ \frac{\vec{v}(\omega) - \vec{v}(\omega_0)}{\omega - \omega_0} &= i \varsigma \vec{v}(\omega_0) \\ \Delta \vec{v}(\omega) &= i \varsigma \Delta \omega \vec{v}(\omega_0) \\ \Delta \vec{v}(\omega) &= z \vec{v}(\omega_0). \end{aligned} \quad (\text{B.5})$$

Eq. (B.5) states that for an eigenstate of  $\rho(\omega, \omega_0)$ , the deviation of the output vector at  $\omega \neq \omega_0$ ,  $\Delta \vec{v}(\omega) = \vec{v}(\omega) - \vec{v}(\omega_0)$ , and, therefore also  $\vec{v}(\omega)$ , is aligned to its value at  $\omega_0$ , with a proportionality constant  $z = i \varsigma \Delta \omega$ .

### Weighting Function & Wavepacket Envelope

In order to produce a weighting function  $W(\omega) = |\epsilon(\omega)|^2$  for the cost function in Eq. (3.27), or a spectral envelope for an input pulse used in the cost function in Eq. (3.30) in the main text,  $\epsilon(\omega)$ , that is continuous on the one hand, but similar to a rectangular function on the other hand, we utilize step-like Fermi functions of the following form,

$$f^\pm(\omega, \omega_0, b, s) = \frac{1}{1 + e^{-(\omega - \omega_0 \pm b/2)/s}}. \quad (\text{B.6})$$

The actual envelope is then given by

$$\epsilon(\omega) = \frac{1}{N_\epsilon} (f^+(\omega, \omega_0, b, s) + f^-(\omega, \omega_0, b, s)), \quad (\text{B.7})$$

where the parameter  $\omega_0$  denotes the center frequency,  $b$  is the FWHM of the envelope, and  $s$  determines the steepness of the slopes. For  $s = 0$ , Eq. (B.6) turns into discontinuous step functions. The normalization constant is given by  $N_\epsilon = \int d\omega |\epsilon(\omega)|^2$ . For the experimental results displayed in the main text, we used the specific values of  $b = 0.875$  THz and  $s = 0.022$  THz.

## The Gradient-Based Optimization Scheme

The gradient with respect to  $\hat{u}^\dagger$  using  $\vec{v}(\omega) = t(\omega) \hat{u}$  for the cost function

$$\begin{aligned} \mathcal{T}(\hat{u}) &= \int d\omega \left( 1 - \frac{|\vec{v}^\dagger(\omega) \cdot \vec{v}(\omega_0)|^2}{|\vec{v}(\omega)|^2 |\vec{v}(\omega_0)|^2} \right) W(\omega) \\ &= \int d\omega \left( 1 - \frac{|\hat{u}^\dagger t^\dagger(\omega) t(\omega_0) \hat{u}|^2}{|t(\omega) \hat{u}|^2 |t(\omega_0) \hat{u}|^2} \right) W(\omega), \end{aligned} \quad (\text{B.8})$$

reads

$$\begin{aligned} \frac{\delta \mathcal{T}}{\delta \hat{u}^\dagger} &= \int d\omega \left[ (t^\dagger(\omega) t(\omega_0) \hat{u} + t^\dagger(\omega_0) t(\omega) \hat{u}) \frac{-\hat{u}^\dagger t^\dagger(\omega_0) t(\omega) \hat{u}}{|t(\omega) \hat{u}|^2 |t(\omega_0) \hat{u}|^2} \right. \\ &+ (t^\dagger(\omega) t(\omega) \hat{u}) \frac{|\hat{u}^\dagger t^\dagger(\omega) t(\omega_0) \hat{u}|^2}{|t(\omega) \hat{u}|^4 |t(\omega_0) \hat{u}|^2} \\ &\left. + (t^\dagger(\omega_0) t(\omega_0) \hat{u}) \frac{|\hat{u}^\dagger t^\dagger(\omega) t(\omega_0) \hat{u}|^2}{|t(\omega) \hat{u}|^2 |t(\omega_0) \hat{u}|^4} \right] W(\omega). \end{aligned} \quad (\text{B.9})$$

Please note that  $|t(\omega) \hat{u}|^2 = \hat{u}^\dagger t^\dagger(\omega) t(\omega) \hat{u}$  and that a derivative of  $\mathcal{T}$  with respect to  $\hat{u}$  does not lead to equations linearly independent from the set of equations (B.9), since  $\mathcal{T}(\hat{u})$  is a purely real quantity.

The  $n + 1$ -th optimization step for the vector  $\hat{u}$  that is optimized for is just calculated from the  $n$ -th step according to

$$\hat{u}_{n+1} = \frac{1}{N_{n+1}} \left( \hat{u}_n - \frac{\delta \mathcal{T}}{\delta \hat{u}^\dagger} \Big|_{\hat{u}_n} \Delta s \right), \quad (\text{B.10})$$

with a suitably chosen stepsize  $\Delta s$  and the normalization constant  $N_{n+1}$  assuring  $|\hat{u}_{n+1}| = 1$ . As starting guesses for each OSPM optimization served the respective projections of the best PM onto the subspaces orthogonal to each of the previously calculated OSPMs. In the first iteration step, we started directly from the best PM.

The second cost function discussed in the main text is given by the expression,

$$\begin{aligned} \mathcal{L}(\hat{u}) &= \int dt \left( \frac{|\vec{v}(t)|^2}{N_v} - \frac{|\epsilon(t - t_0)|^2}{N_\epsilon} \right)^2 \\ &= \int dt \left( \frac{\hat{u}^\dagger I(t) \hat{u}}{\int dt' \hat{u}^\dagger I(t') \hat{u}} - \frac{|\epsilon(t - t_0)|^2}{N_\epsilon} \right)^2, \end{aligned} \quad (\text{B.11})$$

where we introduced the abbreviation

$$I(t) = \int d\omega' \int d\omega \epsilon^*(\omega') t^\dagger(\omega') t(\omega) \epsilon(\omega) e^{-i(\omega-\omega')t} / (2\pi)^2. \quad (\text{B.12})$$

The normalization constant for the input signal reads like  $N_\epsilon = \int dt |\epsilon(t)|^2$ . The gradient  $\delta\mathcal{L}/\delta\hat{u}^\dagger$  evaluates to

$$\begin{aligned} \frac{\delta\mathcal{L}}{\delta\hat{u}^\dagger} &= \int dt \left[ 2 \left( \frac{\hat{u}^\dagger I(t) \hat{u}}{\int dt' \hat{u}^\dagger I(t') \hat{u}} - \frac{|\epsilon(t-t_0)|^2}{N_\epsilon} \right) \right. \\ &\quad \times \left. \left( \frac{I(t) \hat{u}}{\int dt' \hat{u}^\dagger I(t') \hat{u}} - \left( \int dt' I(t') \hat{u} \right) \frac{\hat{u}^\dagger I(t) \hat{u}}{[\int dt' \hat{u}^\dagger I(t') \hat{u}]^2} \right) \right]. \end{aligned} \quad (\text{B.13})$$

Since we also optimize for the unknown temporal shift  $t_0$  in Eq. (B.11), we also have to compute

$$\begin{aligned} \frac{\partial\mathcal{L}}{\partial t_0} &= \int dt \left[ 2 \left( \frac{|\vec{v}(t)|^2}{N_v} - \frac{|\epsilon(t-t_0)|^2}{N_\epsilon} \right) \left( -\frac{i}{N_\epsilon (2\pi)^2} \right) \right. \\ &\quad \times \left. \int d\omega' \int d\omega (\omega - \omega') \epsilon^*(\omega') \epsilon(\omega) e^{-i(\omega-\omega')(t-t_0)} \right]. \end{aligned} \quad (\text{B.14})$$

The  $n+1$ -th step for the temporal shift  $t_0$  is calculated much analogous to Eq. (B.10), where

$$t_{0,n+1} = t_{0,n} + \text{sign} \left[ \frac{\partial\mathcal{L}}{\partial t_0} \Big|_{t_{0,n}} \right] \Delta s'. \quad (\text{B.15})$$

For the construction of both cost functions (B.8) and (B.11), we implicitly used the projected version of the transmission matrix  $t(\omega)$  given by Eq. (2.58), thus avoiding an optimization of the irrelevant dark background of the output signals.

## Expectation Value and Variance of the $\rho(\omega, \omega_0)$ -Operators

For our purposes, we define the expectation value of  $\rho(\omega, \omega_0)$  for a state  $\hat{u}$  analogously to that of a Hermitian operator like

$$\langle \rho(\omega, \omega_0) \rangle = \hat{u}^\dagger \rho(\omega, \omega_0) \hat{u}. \quad (\text{B.16})$$

In contrast to a Hermitian operator, this expectation value is a complex number in general. The variance for the non-Hermitian operators  $\rho(\omega, \omega_0)$ , however, can be computed,

$$\begin{aligned} \langle |\rho(\omega, \omega_0) - \langle \rho(\omega, \omega_0) \rangle|^2 \rangle &= \hat{u}^\dagger \rho(\omega, \omega_0)^\dagger \rho(\omega, \omega_0) \hat{u} \\ &- |\hat{u}^\dagger \rho(\omega, \omega_0) \hat{u}|^2, \end{aligned} \quad (\text{B.17})$$

and gives a purely real number. Note that for an eigenstate of  $\rho(\omega, \omega_0)$ , the expectation value is equal to the corresponding (complex) eigenvalue, and thus, the variance vanishes.



# Bibliography

- [1] O. Dietz, U. Kuhl, H. J. Stöckmann, N. M. Makarov, and F. M. Izrailev. Microwave realization of quasi-one-dimensional systems with correlated disorder. *Phys. Rev. B - Condens. Matter Mater. Phys.*, 83(13):134203, apr 2011.
- [2] F. E. Toole. *Sound Reproduction*. Focal Press, Elsevier, Oxford, 2008.
- [3] A. Prasadka, S. Feat, P. Petitjeans, V. Pagneux, A. Maurel, and M. Fink. Time reversal of water waves. *Phys. Rev. Lett.*, 109:064501, 2012.
- [4] A. Chabchoub and M. Fink. Time-reversal generation of rogue waves. *Phys. Rev. Lett.*, 112:124101, 2014.
- [5] B. Gerardin, J. Laurent, A. Derode, C. Prada, and A. Aubry. Full transmission and reflection of waves propagating through a maze of disorder. *Phys. Rev. Lett.*, 113(17):173901, oct 2014.
- [6] Allard P. Mosk, Ad Lagendijk, Geoffroy Lerosey, and Mathias Fink. Controlling waves in space and time for imaging and focusing in complex media. *Nat. Photonics*, 6(5):283–292, may 2012.
- [7] I. M. Vellekoop and A. P. Mosk. Focusing coherent light through opaque strongly scattering media. *Opt. Lett.*, 32(16):2309–2311, 2007.
- [8] I. M. Vellekoop and A. P. Mosk. Universal optimal transmission of light through disordered materials. *Phys. Rev. Lett.*, 101(12):120601, sep 2008.
- [9] S. M. Popoff, G. Lerosey, R. Carminati, M. Fink, A. C. Boccara, and S. Gigan. Measuring the transmission matrix in optics: An approach to the study and control of light propagation in disordered media. *Phys. Rev. Lett.*, 104(10):100601, mar 2010.

- [10] E. van Putten and A. Mosk. The information age in optics: Measuring the transmission matrix. *Physics (College. Park. Md.)*, 3:22–24, 2010.
- [11] S. Popoff, G. Lerosey, M. Fink, A. C. Boccarda, and S. Gigan. Image transmission through an opaque material. *Nat. Commun.*, 1:81, 2009.
- [12] T. Chaigne, O. Katz, A. C. Boccarda, M. Fink, E. Bossy, and S. Gigan. Controlling light in scattering media non-invasively using the photoacoustic transmission matrix. *Nat. Photonics*, 8(1):58–64, 2013.
- [13] J. Aulbach, B. Gjonaj, P. M. Johnson, A. P. Mosk, and A. Lagendijk. Control of light transmission through opaque scattering media in space and time. *Phys. Rev. Lett.*, 106(10):103901, mar 2011.
- [14] O. Katz, Y. Bromberg, E. Small, and Y. Silberberg. Focusing and Compression of Ultrashort Pulses through Scattering Media. *Nat. Photonics*, 5(6):372–377, may 2010.
- [15] D. J McCabe, A. Tajalli, D. R. Austin, P. Bondareff, I. A. Walmsley, S. Gigan, and B. Chatel. Spatio-temporal focusing of an ultrafast pulse through a multiply scattering medium. *Nat. Commun.*, 2(May):447, jan 2011.
- [16] L. Eisenbud. PhD Thesis, Princeton. 2012.
- [17] D. Bohm. *Quantum Theory*. Prentice-Hall, New York, 1951.
- [18] E. Wigner. Lower Limit for the Energy Derivative of the Scattering. *Phys. Rev.*, 98:5–7, 1955.
- [19] F. T. Smith. Lifetime matrix in collision theory. *Phys. Rev.*, 118(1):349–356, 1960.
- [20] E. H. Hauge and J. A. Støvneng. Tunneling times: A critical review. *Rev. Mod. Phys.*, 61(4):917–936, 1989.
- [21] B. A. van Tiggelen, A. Tip, and A. Lagendijk. Dwell times for light and electrons. *J. Phys. A Math. Gen.*, 26:1731–1748, 1993.
- [22] Y. V. Fyodorov and H.-J. Sommers. Statistics of resonance poles, phase shifts and time delays in quantum chaotic scattering: Random matrix approach for systems with broken time-reversal invariance. *J. Math. Phys.*, 38(4):1918–1981, 1997.

- [23] P. Brouwer, K. Frahm, and C. Beenakker. Quantum Mechanical Time-Delay Matrix in Chaotic Scattering. *Phys. Rev. Lett.*, 78(25):4737–4740, jun 1997.
- [24] D. V. Savin and H.-J. Sommers. Delay times and reflection in chaotic cavities with absorption. *Phys. Rev. E*, 68(3 Pt 2):036211, sep 2003.
- [25] V. L. Lyuboshitz. On collision duration in the presence of strong overlapping resonance levels. *Phys. Lett. B*, 72(1):41–44, 1977.
- [26] S. Souma and A. Suzuki. Local density of states and scattering matrix in quasi-one-dimensional systems. *Phys. Rev. B*, 65(11):115307–7, feb 2002.
- [27] S. Fan and J. M. Kahn. Principal modes in multimode waveguides. *Opt. Lett.*, 30(2):135–137, jan 2005.
- [28] A. A. Juarez, S. Warm, C. A. Bunge, P. M. Krummrich, and K. Petermann. Perspectives of principal mode transmission in a multi-mode fiber. *Eur. Conf. Opt. Commun. ECOC*, 1-2(13):13810, jun 2010.
- [29] J. Carpenter, B. J. Eggleton, and J. Schröder. First demonstration of principal modes in a multimode fibre. *Eur. Conf. Opt. Commun. ECOC*, 9(11):751–757, 2014.
- [30] S. Rotter, P. Ambichl, and F. Libisch. Generating particlelike scattering states in wave transport. *Phys. Rev. Lett.*, 106(12):120602, mar 2011.
- [31] M. A. Topinka, B. J. LeRoy, R. M. Westervelt, S. E. Shaw, R. Fleischmann, E J Heller, K D Maranowski, and A. C. Gossard. Coherent branched flow in a two-dimensional electron gas. *Nature*, 410(6825):183–186, mar 2001.
- [32] M. C. Case and P. F. Zweifel. *Linear Transport Theory*. Addison-Wesley, Reading, Massachusetts, 1967.
- [33] E. Yablonovitch. Statistical ray optics. *J. Opt. Soc. Am.*, 72(7):899–907, 1982.
- [34] E. H. Zhou, H. Ruan, C. Yang, and B. Judkewitz. Focusing on moving targets through scattering samples. *Optica*, 1(4):227–232, 2014.
- [35] S. Datta. *Electronic Transport in Mesoscopic Systems*. Cambridge University Press, Cambridge, 5 edition, 2003.

- [36] L. Reichl. *The Transition to Chaos*. Springer, New York, 2nd edition, 2004.
- [37] H. R. Stuart. Dispersive multiplexing in a multimode optical fiber. *Science*, 289:281–283, 2000.
- [38] R. Sprik, A. Tourin, J. de Rosny, and M. Fink. Eigenvalue distributions of correlated multichannel transfer matrices in strongly scattering systems. *Phys. Rev. B - Condens. Matter Mater. Phys.*, 78(1):012202, 2008.
- [39] S. Rotter, J.-Z. Tang, L. Wirtz, J. Trost, and J. Burgdörfer. Modular recursive Green’s function method for ballistic quantum transport. *Phys. Rev. B*, 62(3):1950–1960, 2000.
- [40] F. Libisch, S. Rotter, and J. Burgdörfer. Coherent transport through graphene nanoribbons in the presence of edge disorder. *New J. Phys.*, 14:123006, 2012.
- [41] H.-J. Stöckmann. *Quantum Chaos*. Cambridge University Press, Cambridge, 1999.
- [42] O. J. F. Martin, C. Girard, and A. Dereux. Generalized field propagator for electromagnetic scattering and light confinement. *Phys. Rev. Lett.*, 74(4):526–529, 1995.
- [43] E. H. Hauge, J. P. Falck, and T. A. Fjeldly. Transmission and reflection times for scattering of wave packets off tunneling barriers. *Phys. Rev. B*, 36(8):4203–4214, 1987.
- [44] P. Ambichl. *Delay Times and Beam-Like Scattering States in Coherent Wave Transmission Through Resonators*. PhD thesis, TU Vienna, 2012.
- [45] J. Schwinger. On gauge invariance and vacuum polarization. *Phys. Rev.*, 82(5):664–679, 1951.
- [46] M. G. Krein. On the theory of wave operators and scattering operators. *Dokl. Akad. Nauk SSSR*, 144:475–478, 1962.
- [47] R. Dashen, S. K. Ma, and H. J. Bernstein. S-matrix formulation of statistical mechanics. *Phys. Rev.*, 187(1):345–370, 1969.
- [48] M. S. Birman and D. R. Yafaev. The spectral shift function. The papers of M. G. Krein and their further development. *Algebr. i Anal.*, 4(5):1–44, 1992.

- [49] A. Yamilov and H. Cao. Manifestation of photonic band structure in small clusters of spherical particles. *Phys. Rev. B*, 68(8):4, aug 2002.
- [50] M. Davy, Z. Shi, J. Wang, X. Cheng, and A. Z. Genack. Transmission eigenchannels and the densities of states of random media. *Phys. Rev. Lett.*, 114(3):033901, 2015.
- [51] G. Breit and E. Wigner. Capture of slow neutrons. *Phys. Rev.*, 49(7):519–531, 1936.
- [52] O. Rosas-Ortiz, N. Fernandez-Garcia, and S. Cruz y Cruz. A Primer on Resonances in Quantum Mechanics. *arXiv*, 1077:28, 2009.
- [53] N. Nakanishi. A Theory of Clothed Unstable Particles. *Prog. Theor. Phys.*, 19(6):822–834, 1958.
- [54] J. Feinberg and A. Zee. Non-hermitian random matrix theory: Method of hermitian reduction. *Nucl. Phys. B*, 504(3):579–608, 1997.
- [55] R. de Madrid. Replacing the Breit-Wigner Amplitude by. *Prog. Theor. Phys. Suppl.*, (184):516–522, 2010.
- [56] E. N. Economou. *Greens Functions in Quantum Physics*. Springer Berlin Heidelberg, Heidelberg, 3rd edition, 2006.
- [57] A. Moroz. Density-of-states calculations and multiple-scattering theory for photons. *Phys. Rev. B*, 51(4):2068–2081, 1995.
- [58] A. Moroz. Minima and maxima of the local density of states for one-dimensional periodic systems. *Europhys. Lett.*, 46(4):419–424, 1999.
- [59] H. E. Türeci, A. D. Stone, and B. Collier. Self-consistent multimode lasing theory for complex or random lasing media. *Phys. Rev. A - At. Mol. Opt. Phys.*, 74(4):043822, oct 2006.
- [60] U. Günther. Theoretical aspects of PT - symmetric S-matrix techniques. *Unpubl. notes*, 2012.
- [61] R. Pierrat, P. Ambichl, S. Gigan, A. Haber, R. Carminati, and S. Rotter. Invariance property of wave scattering through disordered media. *Proc. Natl. Acad. Sci. U. S. A.*, 111(50):17765–17770, 2014.
- [62] M. Büttiker. Larmor precession and the traversal time for tunneling. *Phys. Rev. B*, 27(10):6178–6188, 1983.

- [63] H. Winful. Group delay, stored energy, and the tunneling of evanescent electromagnetic waves. *Phys. Rev. E*, 68(1):016615, jul 2003.
- [64] H. Winful. Delay Time and the Hartman Effect in Quantum Tunneling. *Phys. Rev. Lett.*, 91(26):1–4, 2003.
- [65] I. Ilić, P. P. Beličev, V. Milanović, and J. Radovanović. Modeling of dwell time and group delay in dispersive and absorptive media. *Phys. Scr.*, T135:014040, jul 2009.
- [66] V. V. Sokolov and V. G. Zelevinsky. A Simple Mode on a Highly Excited Background: Collective Strength and Damping in the Continuum. *Phys.Rev.C*, 56(1):23, jul 1997.
- [67] S. Rotter, B. Weingartner, N. Rohringer, and J. Burgdörfer. Ballistic quantum transport at high energies and high magnetic fields. *Phys. Rev. B*, 68(16):165302, 2003.
- [68] G. Iannaccone. General relation between density of states and dwell times in mesoscopic systems. *Phys. Rev. B*, 51(7):4727–4729, 1995.
- [69] R. Höhmann, U. Kuhl, H. J. Stöckmann, L. Kaplan, and E. J. Heller. Freak waves in the linear regime: A microwave study. *Phys. Rev. Lett.*, 104(9):1–4, 2010.
- [70] E. J. Heller, L. Kaplan, and A. Dahlen. Refraction of a Gaussian seaway. *J. Geophys. Res. Ocean.*, 113(9):1–14, 2008.
- [71] H. Degueldre, J. J. Metzger, T. Geisel, and R. Fleischmann. Random focusing of tsunami waves. *Nat. Phys.*, (November):6–11, 2015.
- [72] M. P. Jura, M. A. Topinka, L. Urban, A. Yazdani, H. Shtrikman, L. N. Pfeiffer, K. W. West, and D. Goldhaber-Gordon. Unexpected features of branched flow through high-mobility two-dimensional electron gases. *Nat. Phys.*, 3(12):841–845, nov 2007.
- [73] L. Kaplan. Statistics of branched flow in a weak correlated random potential. *Phys. Rev. Lett.*, 89(18):184103, oct 2002.
- [74] J. J. Metzger, R. Fleischmann, and T. Geisel. Universal statistics of branched flows. *Phys. Rev. Lett.*, 105(2):020601, jul 2010.
- [75] J. J. Metzger, R. Fleischmann, and T. Geisel. Statistics of extreme waves in random media. *Phys. Rev. Lett.*, 112(20):1–5, 2014.

- [76] R. Bruck, B. Mills, B. Troia, D. J. Thomson, F. Y. Gardes, Y. Hu, G. Z. Mashanovich, V. M. N. Passaro, G. T. Reed, and O. L. Muskens. Device-level characterization of the flow of light in integrated photonic circuits using ultrafast photomodulation spectroscopy. *Nat. Photonics*, 9(1):54–60, 2014.
- [77] D. R. Smith, D. R. Smith, W. J. Padilla, W. J. Padilla, D. C. Vier, D. C. Vier, S. C. Nemat-Nasser, S. C. Nemat-Nasser, S. Schultz, and S. Schultz. Composite Medium with Simultaneously Negative Permeability and Permittivity. *Phys. Rev. Lett.*, 84(18):4184–4187, may 2000.
- [78] J. Pendry. Photonics: metamaterials in the sunshine. *Nat. Mater.*, 5(8):599–600, 2006.
- [79] D. Schurig, J. J. Mock, B. J. Justice, S. A. Cummer, J. B. Pendry, A. F. Starr, and R. Smith, D. Metamaterial electromagnetic cloak at microwave frequencies. *Science*, 314(5801):977–980, 2006.
- [80] S. Steinhauer. Controlling Wave Transport Through Disordered Media, Bachelor Thesis, TU Vienna. 2012.
- [81] A. N. Tikhonov. Solution of incorrectly formulated problems and the regularization method. *Sov. Math. Dokl*, 4(4):1035–1038, 1963.
- [82] S. Blanco and R. Fournier. An invariance property of diffusive random walks. *Eur. Phys. Lett.*, 61:168–173, 2003.
- [83] P. Turchin. Translating foraging movements in heterogeneous environments into the spatial distribution of foragers. *Ecology*, 72(4):1253–1266, 1991.
- [84] T. O. Crist and J. A. Macmahon. Individual foraging components of harvester ants - movement patterns and seed patch fidelity. *Insectes.Soc.*, 38(4):379–396, 1991.
- [85] E. E. Holmes. Are diffusion models too simple? A comparison with telegraph models of invasion. *Am. Nat.*, 142(5):779–795, 1993.
- [86] A. Mazzolo. Properties of uniform random walks in bounded convex bodies. *J. Phys. A. Math. Gen.*, 37(28):7095–7111, 2004.
- [87] Olivier Bénichou, M. Coppey, Michel Moreau, P. H. Suet, and Raphael Voituriez. Averaged residence times of stochastic motions in bounded domains. *Europhys. Lett.*, 70(1):42–48, 2005.

- [88] A. Campo, S. Garnier, O. Dédriche, M. Zekkri, and Marco Dorigo. Self-organized discrimination of resources. *PLoS One*, 6(5):e19888, jan 2011.
- [89] O. Bénichou, C. Loverdo, M. Moreau, and R. Voituriez. Optimizing intermittent reaction paths. *Phys. Chem. Chem. Phys.*, 10(47):7059–7072, 2008.
- [90] E. Akkermans. *Mesoscopic Physics of Electrons and Photons*. Cambridge University Press, Cambridge, 2007.
- [91] M. P. Albada and A. Lagendijk. Observation of weak localization of light in a random medium. *Phys. Rev. Lett.*, 55(24):2692–2695, 1985.
- [92] E. Akkermans, P. E. Wolf, and R. Maynard. Coherent backscattering of light by disordered media: Analysis of the peak line shape. *Phys. Rev. Lett.*, 56(14):1471–1474, 1986.
- [93] A. Lagendijk, B. van Tiggelen, and D. S. Wiersma. Fifty years of Anderson localization. *Phys. Today*, 62(8):24–29, 2009.
- [94] V. A. Gopar and R. A. Molina. Controlling conductance statistics of quantum wires by driving ac fields. *Phys. Rev. B*, 81(19):195415, may 2010.
- [95] A. Peña, A. Girschik, F. Libisch, S. Rotter, and A. A. Chabanov. The single-channel regime of transport through random media. *Nat. Commun.*, 5:3488, jan 2014.
- [96] H. Weyl. Über die asymptotische Verteilung der Eigenwerte. *Göttinger Nachrichten*, 1911(2):110–117, 1911.
- [97] W. Arendt, R. Nittka, W. Peter, and F. Steiner. *Weyl’s Law: Spectral Properties of the Laplacian in Mathematics and Physics*. Weinheim, 2009.
- [98] H. Weyl. Über die Randwertaufgabe der Strahlungstheorie und asymptotische Spektralgesetze. *J. für die Reine und Angew. Math.*, 1913(143):177–202, 1913.
- [99] Z. Yu, A. Raman, and S. Fan. Fundamental limit of nanophotonic light trapping in solar cells. *Proc. Natl. Acad. Sci. U. S. A.*, 107(41):17491–17496, 2010.

- [100] T. Markvart. Beyond the Yablonovitch limit: Trapping light by frequency shift. *Appl. Phys. Lett.*, 98(7):071107, 2011.
- [101] O. D. Miller, E. Yablonovitch, and S. R. Kurtz. Strong internal and external luminescence as solar cells approach the Shockley-Queisser limit. *IEEE J. Photovoltaics*, 2(3):303–311, 2012.
- [102] J. Melchard. Dwell Time and Intensity Enhancement: On the Connection Between Universal Time and the Yablonovitch Limit, Bachelor Thesis, TU Vienna. 2015.
- [103] W. Xiong, P. Ambichl, Y. Bromberg, B. Redding, S. Rotter, and H. Cao. Spatiotemporal Control of Light through a Multimode Fiber Using Principal Modes, Submitt. to PRL. 2015.
- [104] V. Bagnoud and J. D. Zuegel. Independent phase and amplitude control of a laser beam by use of a single-phase-only spatial light modulator. *Opt. Lett.*, 29(3):295–297, 2004.
- [105] H. Itoh, T. Urakami, S. I. Aoshima, and Y. Tsuchiya. Femtosecond pulse delivery through long multimode fiber using adaptive pulse synthesis. *Japanese J. Appl. Physics, Part 1 Regul. Pap. Short Notes Rev. Pap.*, 45(7):5761–5763, 2006.
- [106] A. M. Weiner. Ultrafast optical pulse shaping: A tutorial review. *Opt. Commun.*, 284(15):3669–3692, 2011.
- [107] R.-J. Essiambre, G. Kramer, P. J. Winzer, G. J. Foschini, and B. Goebel. Capacity Limits of Optical Fiber Networks. *J. Light. Technol.*, 28(4):662–701, 2010.
- [108] A. Brandstötter. Wave control in complex media - from material design to wave front shaping, Diploma Thesis, TU Vienna. 2016.
- [109] R. Horstmeyer, H. Ruan, and C. Yang. Guidestar-assisted wavefront-shaping methods for focusing light into biological tissue. *Nat Phot.*, 9(9):563–571, 2015.
- [110] S. Hübsch. Focusing on Moving Targets Behind Scattering Media, Bachelor Thesis, TU Vienna. 2015.
- [111] M. Kühmayer. Particlelike States in D-Shaped Fibers, Diploma Thesis, TU Vienna. 2016.

- [112] V. Doya, O. Legrand, F. Mortessagne, and C. Miniatura. Light scattering in an optical fiber. *Phys. Rev. Lett.*, 88:014102, 2002.
- [113] S. Ree and L. E. Reichl. Classical and quantum chaos in a circular billiard with a straight cut. *Phys. Rev. E*, 60(2):1607–1615, 1999.
- [114] K. Husimi. Some Formal Properties of the Density Matrix. *Proc. Physico-Mathematical Soc. Japan. 3rd Ser.*, 22(4):264–314, 1940.
- [115] S. Rotter and S. Gigan. Light fields in complex media: mesoscopic scattering meets wave control, Subm. to *Rev. Mod. Phys.* 2016.
- [116] R. Mathias. A Chain Rule for Matrix Functions and Applications. *SIAM J. Matrix Anal. Appl.*, 17(3):610–620, jul 1996.
- [117] H. U. Baranger and P. A. Mello. Mesoscopic Transport through Chaotic Cavities: A Random S-Matrix Theory Approach. *Phys. Rev. Lett.*, 73(1):142–145, 1994.
- [118] R. A. Jalabert, J.-L. Pichard, and C. W. J. Beenakker. Universal Quantum Signatures of Chaos in Ballistic Transport. *Europhys. Lett.*, 27(4):255, 1994.
- [119] C. W. J. Beenakker. Random-matrix theory of quantum transport. *Rev. Mod. Phys.*, 69(3):731–808, jul 1997.

# Acknowledgements

No scientist is an island. This thesis and the corresponding research would not have been possible without the help of many people whom I would like to thank.

I am deeply grateful for the support and understanding of my bachelor, diploma, and doctoral advisor Stefan Rotter throughout many years. Without his tireless efforts to push science further, many of the projects presented in this thesis would not have seen the light of day. I must also thank Stefan not only for promoting my scientific advances, but also for indirectly enabling many valuable experiences and career opportunities resulting from my scientific research and work.

A great willingness to assist me with computer or physics troubles of any kind, many useful, and especially even more useless discussions, is what I have to thank my colleagues from the Institute for Theoretical Physics for. Especially (but not only) all the guys from the third floor, of course, have grown dear to my heart over the years.

Further, I am grateful for the contributions and support of all external collaboration partners who co-authored our mutual publications. Especially I thank (in alphabetical order) Julian Böhm, Yaron Bromberg, Hui Cao, Rémi Carminati, Sylvain Gigan, Ulrich Kuhl, Konstantinos Makris, Romain Pierrat, and Wen Xiong from Nice, Paris, Yale, and Crete, respectively.

Besides for their great scientific endeavors, I would like to thank my students (in order of their matriculation numbers) Stephan Steinhauer, Matthias Kühmayer, Andre Brandstötter, Michael Stückler, Katharina Newrkla, Faruk Salighbegovic, Jakob Melchard, Naz Shokrani, and Stephan Hübsch not only for obeying my commands as if they were the word of God, but also for sharing my weird sense of humor. Especially I am grateful for my diploma students Matthias Kühmayer and Andre Brandstötter, who created such an amusing and warm, yet productive atmosphere in our shared office.

I cannot even put my gratitude into words towards the architects of the Freihaus for 'designing' this building I spent so many days in during the last ten years.

I am very grateful for the constant moral and financial support of my mother and grandmother throughout the many years of my studies at the Vienna University of Technology.

Finally, I must thank Sonja Mielczarek, she knows what for.



# List of Publications

- B. Gérardin, J. Laurent, P. A., C. Prada, S. Rotter, and A. Aubry,  
*Particle-like wave packets in complex scattering systems*,  
arXiv:1602.05812, submitted to Physical Review X (2016).
- W. Xiong, P. A., Y. Bromberg, B. Redding, S. Rotter, and H. Cao,  
*Spatio-temporal control of light transmission through  
a multimode fiber with strong mode coupling*,  
arXiv:1601.04646, submitted to Physical Review Letters (2016).
- R. Pierrat, P. A\*, S. Gigan, A. Haber, R. Carminati, and S. Rotter,  
*Invariance property of wave scattering through disordered media*,  
Proceedings of the National Academy of Sciences of the United States  
of America **111**, 17765 (2014). \* shared first authorship
- P. A., K. G. Makris, L. Ge, Y. Chong, A. D. Stone, and S. Rotter,  
*Breaking of  $PT$ -symmetry in bounded  
and unbounded scattering systems*,  
Physical Review X **3**, 41030 (2013).
- S. Rotter, P. A., and F. Libisch,  
*Generating particle-like scattering states in wave transport*,  
Physical Review Letters **106**, 120602 (2011).

## Manuscripts in preparation:

- P. A., A. Brandstötter, J. Böhm, M. Kühmayer, U. Kuhl, and S. Rotter,  
*Focus and Omission in Disordered Media* (2016).
- P. A., W. Xiong, Y. Bromberg, B. Redding, H. Cao, and S. Rotter,  
*Orthogonal Super Principal Modes as Carriers  
for Optimal Pulse Transmission* (2016).
- A. Girschik, A. Brandstötter, P. A., and S. Rotter,  
*Control of Branched Flow in Optics* (2016).

# Curriculum Vitae

Philipp Ambichl  
Dipl.-Ing.

## personal information

born on May 2nd 1987 in St. Pölten, Lower Austria  
present employment adress:

Institute for Theoretical Physics E136  
Vienna University of Technology (TU Vienna)  
Wiedner Hauptstraße 8-10  
1040 Vienna  
**T** +43 1 58801 136 49  
philipp.ambichl@tuwien.ac.at

## education and academic employment

since July 2012	employed as <b>Project Assistant</b> at the Institute for Theoretical Physics of the Vienna University of Technology
since July 2012	<b>PhD studies</b> in theoretical physics at the Vienna University of Technology
October 2010 - June 2011	employed as <b>Tutor</b> for quantum theory and data processing at the Vienna University of Technology
March 2010 - June 2012	<b>Master studies</b> in physics at the Vienna University of Technology
October 2006 - March 2010	<b>Bachelor studies</b> in physics at the Vienna University of Technology

### **talks, activities, and distinctions in science communication and popular science**

- April 2015      **Invited talk** at the **Gala Evening** on the occasion of the 200th anniversary of the Vienna University of Technology
- December 2014    Article in the print version of the Austrian newspaper **Die Presse** "Irrwege, nicht nur im Advent" from December 13th 2014, article discussing our publication in PNAS **111**, 17765 (2014)
- October 2011    **Concluding talk** (invited) at the annual meeting of **Sparkling Science**, program to promote young talents in science organized by the Austrian Ministry of Science
- June 2011        **4th Place** at **FameLab International 2011**, international competition in science communication held by the British Council in the framework of "The TIMES Cheltenham Science Festival"
- May 2011        **1st Place** at **FameLab Austria 2011**, national competition in science communication held by the British Council
- April 2011       David Appell, "How to Shout Without Anyone Hearing", Phys. Rev. Focus 27, 13 (2011) - **Physical Review Focus** article discussing our publication in PRL **106**, 120602 (2011)
- April 2011       Articles in the print versions of the Austrian newspapers **Standard** "Maßschneiderei für Wellen", and **Wiener Zeitung** "Die schnurgerade Welle", both from April 5th 2011, articles discussing our publication in PRL **106**, 120602 (2011)

### **private interests and distinctions**

- Sifu of WingTsun    honorary title (fatherly teacher) for high-ranking Kung Fu teachers
- management club    invited member of the management club (mc)
- reading                classics, popular science, far-eastern philosophies
- Zamioculcas         breeding and cultivating to extraordinary sizes

Vienna, March 23rd 2016